Multifocal Multiphoton Microscopy for Neurobiological Imaging

By

Jae Won Cha

B.S., Mechanical and Aerospace Engineering
Seoul National University (2003)

S.M., Mechanical Engineering
Massachusetts Institute of Technology (2007)

Submitted to the Department of Mechanical Engineering
in Partial Fulfillment of the Requirements for the Degree of

Doctor of Philosophy

at the
MASSACHUSETTS INSTITUTE OF TECHNOLOGY

February 2014

Signature of Author: _____
Department of Mechanical Engineering
Jan 15, 2014

Certified by: _____
Peter T. C. So
Professor of Mechanical Engineering and Biological Engineering
Thesis Supervisor

Accepted by: _____
David E. Hardt
Chairman of the Departmental Committee for Graduate Students

Multifocal Multiphoton Microscopy for Neurobiological Imaging

By

Jae Won Cha

Submitted to the Department of Mechanical Engineering
on Jan 15, 2014 in Partial Fulfillment of the
Requirements for the Degree of Doctor of Philosophy in
Mechanical Engineering

Abstract

Observing neuronal structures and monitoring changes in synaptic connectivity with respect to time have a significant impact on understanding the basis of structural brain abnormalities and the development of therapeutics for their correction. Today, multiphoton excitation fluorescence microscopy is the method of choice for in vivo neuronal imaging with its inherent 3D resolution, minimal photo-damage, and excellent penetration depth. The study of neuronal interactions on dendritic arbor remodeling often requires large volume imaging demanding fast imaging speed. One of the methods to improve imaging speed is multifocal multiphoton microscopy (MMM) that parallelizes imaging process with multiple excitation foci. Early MMM had very limited imaging depth due to signal-to-noise ratio (SNR) degradation resulting from the scattering of emission photons in highly turbid biological specimens. The development of descanned MMM with multianode photomultiplier tube has partly alleviated this problem, but it still suffers from greater signal loss and the presence of image artifacts compared with conventional single focus multiphoton microscopes. In this thesis, adaptive optics compensation, image post processing for emission photon reassignment, and a novel non-descanned MMM have been investigated for SNR improvement. In addition, spectral resolved MMM has been developed for simultaneous fast imaging and spectral detection.

Thesis Supervisor: Peter T. C. So
Title: Professor of Mechanical Engineering and Biological Engineering

Acknowledgement

It was pretty long time to study at MIT and finish my Ph.D. work. During my nine-year Boston life, I am deeply indebted to many people for academic research as well as personal life.

First of all, I would like to thank my thesis advisor, Prof. Peter So for his generosity, guidance, encouragement, tolerance, and trust. He has given me limitless opportunities even from when I was a complete novice as a master candidate. In addition, whenever I faced challenging situations, he was always supportive and provided essential advice. Not only his academic advice, but also his thoughtful consideration was indispensable for my successful MIT life. I also would like to thank Prof. Elly Nedivi for her support, advice, generosity, patience, and trust. She was another greatest support for my study and life at MIT. I also would like to express my gratitude to Prof. Roger Kamm for his key advice, guidance and generous support for successful research.

I also thank all the former and current So Lab members, especially Kihean Kim, Daekeun Kim, Hyuksang Kwon, Euihean Chung, Maxine Jonas, Judith Su, Heejin Choi, Dimitris Tzeranis, Yang-Hyo Kim, Christof Buehler, Hayden Huang, Timothy Ragan, Karsten Bahlmann, Christopher Rowlands, Elijah Yew, Vijay Raj Singh, Yun-Ho Jang, Barry Masters, and Sossy Megerdichian for their academic advice, numerous help, and warm-hearted support.

I also would like to thank all the people who have been with me in my Boston life, Korean Graduate Student Association members in Mechanical Engineering, SNU OB Choir members in Boston, many MIT friends, and especially Jooeun Ahn and his family for priceless friendship.

I cannot imagine how I can express my appreciation to my parents and parents-in-law. I am deeply grateful to Sung-Chan Cha, Soon-Ja Koo, Je-Kyung Ryu, and Ja-Kyung Choi.

Especially I thank my wife, Min Young Yoo for her constant support and endless love, and our children, Yuna, Jihyo, and Seehun with all my heart.

I would like to acknowledge my funding sources and sponsors, NIH RO1 EY017656, Singapore-MIT Alliance 2, Singapore MIT Alliance for Research and Technology, and Imagine Optic.

Table of Contents

List of Figures

Abbreviations

1D	one-dimensional
2D	two-dimensional
3D	three-dimensional
AO	adaptive optics
AOI	angle of incidence
CPC	custom parabolic light collector
DALYs	disability adjusted life years
DOE	diffractive optical element
FOV	field-of-view
FWHM	full-width at half-maximum
MAPMT	multianode photomultiplier tube
ML	maximum likelihood
MMM	multifocal multiphoton microscopy
NA	numerical aperture
PMT	photomultiplier tube
PSF	point spread function
SGR	signal-to-ghost image ratio
SNR	signal-to-noise ratio
SPAD	single-photon avalanche diode
TCSPC	Time-Correlated Single Photon Counting
WHO	world health organization

Chapter 1

Introduction

1.1 Multiphoton microscopy for neurobiological imaging

The economic costs of mental illness have been ranked one of the top five costly conditions in the entire health care costs. The Agency for Healthcare Research and Quality cited a cost of $57.5B in 2006 for mental health care in the U.S., which was equivalent to the cost of cancer care [1]. In addition, the World Health Organization (WHO) has reported that mental illnesses are the leading causes of disability adjusted life years (DALYs, the number of years lost due to ill-health, disability or early death) worldwide, accounting for 37% of healthy years lost from non-communicable diseases [2]. Considering not only the cost of health care, but also the intangible loss such as unemployment, expenses for social supports, and a range of indirect costs due to a chronic disability, understanding of cognitive disorders, needless to say, is important.

Numerous studies have revealed that many mental disorders exhibit some form of structural change in the brain at the global as well as the cellular level [3-7]. It is suspected that neuronal and synaptic deficits result in altered connectivity and thus give rise to pathophysiological circuit dysfunction. Therefore, observing neuronal structures in relation to mental disorders and monitoring subtle changes in connectivity with respect to time have a significant impact on understanding the basis of structural brain abnormalities and the development of therapeutics for their correction.

Multiphoton excitation fluorescence microscopy is the method of choice for in vivo neuronal imaging in animal models. The theory of the two-photon excitation was first introduced by Maria Göppert-Mayer in 1931 [8]. In the two-photon excitation process, a fluorophore (fluorescent chemical compound that can re-emit light upon light excitation) is brought to an electronically excited state by the simultaneous

absorption of two photons. Each photon has approximately half of the energy that is needed for the transition between the ground state and the excited state [Fig 1.1]. Similarly one-photon excitation process requires only single photon to excite a fluorophore. The one-photon excitation process typically requires photons in the ultraviolet, blue, or green spectral range, which can easily damage biological specimens. However, the two-photon excitation process typically uses red or infrared spectral range, which has less energy than those for the one-photon excitation process. Therefore, two-photon excitation microscopy is often more suitable for non-invasive biological imaging with less photon-damaging [9-11].

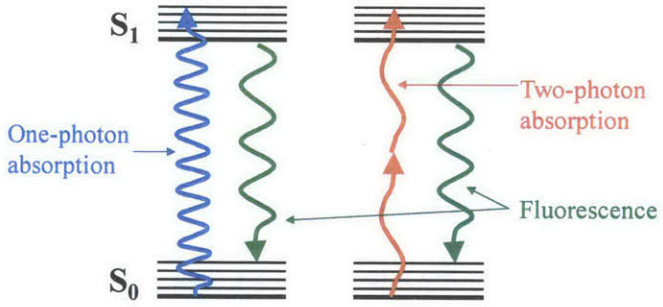

Fig 1.1. Jablonski diagram for one-photon and two-photon excitation.

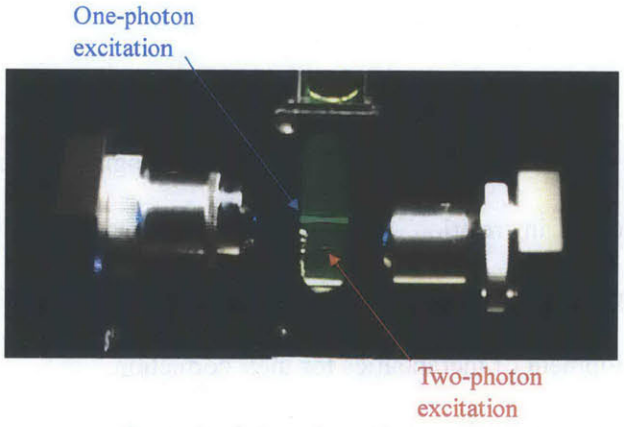

Fig 1.2. Comparison of one- and two-photon excitation profiles [10].

Two-photon microscopy has inherent 3D resolution due to the quadratic dependence of the excitation process on the incident light distribution. Two-photon excitation can be localized to a femtoliter region

about the focal point of a high numerical aperture objective [Fig 1.2]. In addition two-photon excitation microscopy has the capability of deep tissue imaging. Typically tissue specimens are turbid and easily scatter light, but scattering is inversely proportional to the wavelength to the fourth power in the Rayleigh approximation; therefore, the longer wavelength excitation light of the two-photon excitation can better penetrate the thick tissues compared to the one-photon excitation wavelengths.

In 1990, Denk, Webb, and co-workers first demonstrated the two-photon excitation fluorescence microscopy [9]. As a light source, typically a femto-second pulsed laser is used. The high peak power of a mode-locked laser pulse increases the efficiency of the two-photon excitation with minimal photo-induced thermal damage. The raster scanning is accomplished by deflecting the excitation beam using galvanometer-driven x-y mirrors. The excitation beam is expanded by a scan lens and a tube lens to ensure overfilling of the back aperture of an objective lens. The expanded laser beam is reflected by a dichroic mirror towards the back aperture of the objective lens, and focused on the sample. The emission light is collected by the same objective lens and passes through the dichroic mirror. A highly sensitive photon detector, such as a photomultiplier tube, is used to detect the emission signal. Fig 1.3 shows the schematic of two-photon excitation fluorescence microscopy.

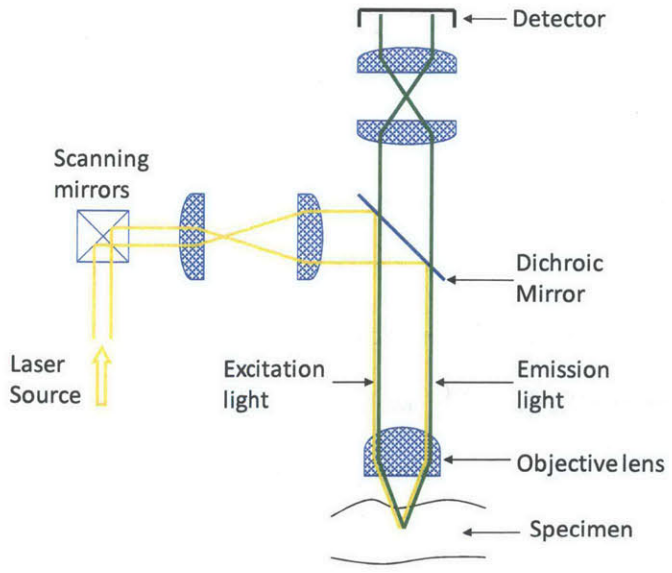

Fig 1.3. The schematic of two-photon excitation fluorescence microscopy.

1.2 Imaging speed improvement in multiphoton microscopy

Multiphoton microscopy has been applied in structural plasticity studies of mature mouse brains including the remodeling of the whole dendritic arbor of neurons [12-15]. Dendritic remodeling is a complex process that depends on many factors including interactions between pre-synaptic and post-synaptic neuronal partners. Since many neurons have extensive arbor structures, the study of neuronal interactions on dendritic arbor remodeling often requires imaging over a volume of several cubic millimeters. For this large volume imaging, fast imaging speed becomes critical for minimizing animal stress due to prolonged anesthesia, overcoming motion artifacts, and improving imaging throughput. Several methods have been developed to improve imaging speed beyond conventional point scanning approach based on galvanometric mirror scanners. One approach is based on the use higher speed scanners such as polygonal mirrors [16], resonant mirror scanners [17], or acousto-optical deflectors [18-21]. These high speed scanners can typically achieve frame rate up to about 1 kHz in tissues with a comparable imaging depth as conventional multiphoton microscopy. However, the higher speed scanning requires a correspondingly decreased pixel dwell time resulting in lower signal-to-noise ratio (SNR). This tradeoff can be partially compensated by increasing the excitation laser power but laser power is ultimately limited by specimen photodamage and excitation saturation [11, 22]. Another approach is two-photon wide-field imaging based on temporal focusing [23, 24]. In this case, two-photon excitation is localized to a plane, instead of a point, by controlling the spectrally dispersing the light pulse away from the focal plane. However, wide-field two-photon imaging is often limited by the lower axial resolution and the smaller field-of-view (FOV) due to the need for much higher peak power laser pulses. Another popular approach to improve imaging speed is multifocal multiphoton microscopy (MMM) [25, 26]. With a lenslet array or a diffractive optical element (DOE) [27, 28], multiple foci are generated and scanned simultaneously. Within the limit of available laser power, about a hundred foci can be effectively generated with a standard Ti-Sapphire oscillator resulting in approximately two orders of magnitude improvement in imaging speed proportionally. For MMM system, simultaneous acquisition of data from many foci often

require the use of an area detector, such as a CCD or a CMOS sensor [25, 26]. The spatial registration is achieved by telecentric mapping of the image plane into the image sensor plane. In the presence of a turbid specimen, the emission photons can be scattered resulting in image blurring. More important, as scattered emission photons are scattered away from the correct location, they contribute to an increased background and degrading image SNR. To overcome the scattering issue, MMM with a descanned detection configuration using a multianode photomultiplier tube (MAPMT) has been developed [29, 30]. As in most confocal microscopes, the descanned geometry guides the emission photons from each focus backward along the same optical path shared with the excitation beams [31-34]. Since the motion of the scanning mirror is much slower than the speed of light, the emission light rays after the scanning mirror becomes stationary independent of scanner motion and can be separated from the excitation beams with a dichroic mirror. The unscattered ballistic emission photons generated by each focus are focused at the cathode which is corresponding to the center of each anode of the MAPMT. The scattered emission photons will not be focused at the center but many can still be collected by the corresponding anode. Very intuitively, the larger area projected by each anode at the specimen plane will results in greater collection efficiency of these scattered emission photons. At the limit of infinitely large anode, the collection efficiency of scattered emission photons will be comparable to that of a single focus scanning multiphoton system. Since the infinitely large anode cannot be completely realized, if the sample is highly scattering and imaging depth is large, the scattered emission photons will reach neighbor anodes resulting in ghost images in the neighbor sub-images. In addition, the emission signal loss can be severe in the long optical path associated with the descanned detection geometry due to the small size of optics and many optical surfaces [29]. To achieve not only fast imaging speed, but also comparable SNR, adaptive optics (AO) compensation (chapter 2), image post processing for emission photon reassignment (chapter 3), and non-descanned MMM (chapter 4) have been investigated in this thesis. In addition, spectral resolved MMM is further introduced for simultaneous fast imaging and spectral detection (chapter 5).

1.3 Signal-to-noise ratio improvement in MMM

1.3.1 Adaptive optics compensation

The imaging depth of two-photon excitation fluorescence microscopy is partly limited by the inhomogeneity of the refractive index in biological specimen. This inhomogeneity results in a distortion of the wavefront of the excitation light. This wavefront distortion results in image resolution degradation and lower signal level. Using an adaptive optics system consisting of a Shack-Hartmann wavefront sensor and a deformable mirror, the wavefront distortion can be measured and corrected. With adaptive optics compensation, it is demonstrated that the resolution and signal level can be better preserved at greater imaging depth in a variety of ex vivo tissue specimens including mouse tongue muscle, heart muscle and brain in chapter 2. However, for these highly scattering tissues, it is found that signal degradation due to scattering to be a more dominant factor than aberration.

1.3.2 Emission photon reassignment

MMM achieves fast imaging by simultaneously scanning multiple foci across different regions of a specimen. The sub-images generated by the foci are combined as a montage to form the final image. In order to resolve the signals from the different foci, imaging detectors, such as CCD cameras, are used. The use of imaging detectors results in degradation of image SNR due to the scattering of emitted photons into neighbor pixels limiting image depth. It has been shown that SNR can be partly recovered using MAPMT [29]. In this design, however, emission photons scattered to neighbor anodes are encoded by the foci scan location resulting in ghost images, duplicates of an image acquired by one focus added onto the images of neighbor foci. The crosstalk between different anodes can be quantified by a scattering matrix that can be measured a priori. With the known scattering matrix, the photons of these ghost images can be reassigned to restore the final picture. However, a priori measurement of this scattering matrix is

cumbersome as scattering crosstalk depends on specimen type, location, and depth. The need to measure the scattering matrix a priori partly negates the advantage of the high speed imaging of MMM. In chapter 3, a novel methodology is investigated for the photon reassignment process based on the maximum likelihood estimation for the quantification of the crosstalk between the anodes of MAPMT without a priori measurement. The method provides the reassignment of the photons generated by the ghost images to the original spatial location thus increases the SNR of the final reconstructed image.

1.3.3 Non-descanned MMM

MMM improves imaging speed over point scanning approach by parallelizing the excitation process. Early versions of MMM rely on imaging detectors, such as CCD or CMOS, to simultaneously record emission signals from multiple foci. Image registration is achieved by telecentric mapping of the specimen plane to the image plane of the detector. For many turbid biological specimens, the scattering of emission photons results in blurred images and degrading SNR. It has been demonstrated that a MAPMT placed in a descanned configuration can effectively collect scattered emission photons from each focus into their corresponding anodes significantly improving image SNR for highly scattering specimens [29]. This approach is especially effectively with high numerical aperture, low magnification objectives that allows foci to be widely separated in the specimen plane. However, this descanned MMM approach has several drawbacks. The longer detection path of the descanned configuration caused significant emission photon loss up to 70 % [29]. Further, it is a challenge to design intermediate optics in the descanned geometry that minimizes optical aberration of the foci located in the edge of the large FOV for high NA, low magnification objectives resulting in resolution loss at image edges. Overcoming these drawbacks, a novel non-descanned MMM based on MAPMT is introduced in chapter 4. In this non-descanned configuration, the excitation foci can be widely separated covering the full FOV of these objectives with minimal aberrations, and signal collection efficiency can be improved up to fourfold.

1.4 Spectral resolved MMM

Multiphoton excitation fluorescence microscopy is the preferred method for in vivo deep tissue imaging. There are many biological applications that demand high imaging speed. One of the successful methods to improve the imaging speed in highly turbid specimen is multifocal multiphoton microscopy (MMM) based on multi-anode photomultiplier tubes (MAPMT). It improves imaging speed by using multiple foci for parallelized excitation without sacrificing signal to noise ratio (SNR) due to the scattering of emission photons. In this work, we demonstrate that the MAPMT based MMM approach can be extended by implementing of spectroscopic imaging capability. Instead of generating multiple excitation foci in 2D grid pattern, a linear array of foci is generated. This leaves one axis of the MAPMT available for spectral dispersion and detection. The spectral-resolved MMM can detect several emission signals simultaneously with high imaging speed optimized for high-throughput, high-contents applications (chapter 5).

References

1. Soni, A., *The five most costly conditions, 1996 and 2006: Estimates for the US civilian noninstitutionalized population. Statistical Brief# 248. July 2009.* 2009, Rockville, MD: Agency for Healthcare Research and Quality.
2. Alwan, A., *Global status report on noncommunicable diseases 2010.* 2011: World Health Organization.
3. Fiala, J.C., J. Spacek, and K.M. Harris, *Dendritic spine pathology: cause or consequence of neurological disorders?* Brain Research Reviews, 2002. **39**(1): p. 29-54.
4. Grutzendler, J. and W.-B. Gan, *Two-photon imaging of synaptic plasticity and pathology in the living mouse brain.* NeuroRx, 2006. **3**(4): p. 489-496.
5. Penzes, P., et al., *Dendritic spine pathology in neuropsychiatric disorders.* Nature neuroscience, 2011. **14**(3): p. 285-293.
6. Kays, J.L., R.A. Hurley, and K.H. Taber, *The dynamic brain: neuroplasticity and mental health.* The Journal of neuropsychiatry and clinical neurosciences, 2012. **24**(2): p. 118-124.
7. Murmu, R.P., et al., *Dendritic Spine Instability Leads to Progressive Neocortical Spine Loss in a Mouse Model of Huntington's Disease.* The Journal of Neuroscience, 2013. **33**(32): p. 12997-13009.
8. Göppert-Mayer, M., *Über elementarakte mit zwei quantensprüngen.* Annalen der Physik, 1931. **401**(3): p. 273-294.
9. Denk, W., J.H. Strickler, and W.W. Webb, *2-PHOTON LASER SCANNING FLUORESCENCE MICROSCOPY.* Science, 1990. **248**(4951): p. 73-76.
10. So, P.T.C., et al., *Two-photon excitation fluorescence microscopy.* Annual Review of Biomedical Engineering, 2000. **2**: p. 399-429.
11. Zipfel, W.R., R.M. Williams, and W.W. Webb, *Nonlinear magic: multiphoton microscopy in the biosciences.* Nature biotechnology, 2003. **21**(11): p. 1369-1377.
12. Lee, W.C.A., et al., *Dynamic remodeling of dendritic arbors in GABAergic interneurons of adult visual cortex.* Plos Biology, 2006. **4**(2): p. 271-280.
13. Lee, W.C.A., et al., *A dynamic zone defines interneuron remodeling in the adult neocortex.* Proceedings of the National Academy of Sciences, 2008. **105**(50): p. 19968-19973.
14. Chen, J.L., et al., *Structural basis for the role of inhibition in facilitating adult brain plasticity.* Nature neuroscience, 2011. **14**(5): p. 587-594.
15. Chen, J.L., et al., *Clustered dynamics of inhibitory synapses and dendritic spines in the adult neocortex.* Neuron, 2012. **74**(2): p. 361-373.
16. Kim, K.H., C. Buehler, and P.T.C. So, *High-speed, two-photon scanning microscope.* Applied optics, 1999. **38**(28): p. 6004-6009.
17. Fan, G., et al., *Video-rate scanning two-photon excitation fluorescence microscopy and ratio imaging with cameleons.* Biophysical journal, 1999. **76**(5): p. 2412-2420.
18. Iyer, V., B.E. Losavio, and P. Saggau, *Compensation of spatial and temporal dispersion for acousto-optic multiphoton laser-scanning microscopy.* Journal of Biomedical Optics, 2003. **8**: p. 460.
19. Reddy, G.D. and P. Saggau, *Fast three-dimensional laser scanning scheme using acousto-optic deflectors.* Journal of Biomedical Optics, 2005. **10**: p. 064038.
20. Zeng, S., et al., *Simultaneous compensation for spatial and temporal dispersion of acousto-optical deflectors for two-dimensional scanning with a single prism.* Optics Letters, 2006. **31**(8): p. 1091-1093.
21. Katona, G., et al., *Fast two-photon in vivo imaging with three-dimensional random-access scanning in large tissue volumes.* Nature methods, 2012. **9**(2): p. 201-208.
22. Cianci, G.C., J. Wu, and K.M. Berland, *Saturation modified point spread functions in two-photon microscopy.* Microscopy research and technique, 2004. **64**(2): p. 135-141.
23. Oron, D., E. Tal, and Y. Silberberg, *Scanningless depth-resolved microscopy.* Optics Express, 2005. **13**(5): p. 1468-1476.
24. Zhu, G., et al. *Simultaneous spatial and temporal focusing of femtosecond pulses.* 2005: Optical Society of America.
25. Bewersdorf, J., R. Pick, and S.W. Hell, *Multifocal multiphoton microscopy.* Optics Letters, 1998. **23**(9): p. 655-657.
26. Buist, A.H., et al., *Real time two-photon absorption microscopy using multi point excitation.* Journal of Microscopy-Oxford, 1998. **192**: p. 217-226.

27. Sacconi, L., et al., *Multiphoton multifocal microscopy exploiting a diffractive optical element.* Optics Letters, 2003. **28**(20): p. 1918-1920.
28. Watson, B.O., V. Nikolenko, and R. Yuste, *Two-photon imaging with diffractive optical elements.* Frontiers in neural circuits, 2009. **3**.
29. Kim, K.H., et al., *Multifocal multiphoton microscopy based on multianode photomultiplier tubes.* Optics Express, 2007. **15**(18): p. 11658-11678.
30. Martini, J., V. Andresen, and D. Anselmetti, *Scattering suppression and confocal detection in multifocal multiphoton microscopy.* Journal of biomedical optics, 2007. **12**(3): p. 034010-034010-6.
31. Minsky, M., *Microscopy apparatus.* 1961, US Patent 3013467.
32. Sheppard, C. and A. Choudhury, *Image formation in the scanning microscope.* Journal of Modern Optics, 1977. **24**(10): p. 1051-1073.
33. Brakenhoff, G., P. Blom, and P. Barends, *Confocal scanning light microscopy with high aperture immersion lenses.* Journal of microscopy, 1979. **117**(2): p. 219-232.
34. Carlsson, K. and N. Åslund, *Confocal imaging for 3-D digital microscopy.* Applied optics, 1987. **26**(16): p. 3232-3238.

Chapter 2

A Shack-Hartmann Wavefront Sensor Based Adaptive Optics System for Multiphoton Microscopy[1]

2.1. Introduction

Two-photon excitation fluorescence microscopy has millimeter scale penetration depth in biological specimens [1, 2]. However, the refractive index inhomogeneity in these samples often distorts the wavefront of the excitation light resulting in broader focal point spread function and lower two-photon excitation efficiency. With an adaptive optics system, this wavefront distortion can be compensated and image resolution and signal level can be preserved at greater imaging depth.

The adaptive optics approach was first developed in fields such as astronomy [3] and ophthalmology [4]. In microscopy, significant progress has been made in confocal systems [5, 6], and also adaptive optics has been applied to nonlinear microscopies such as two-photon excitation microscopy [7, 8], harmonic generation microscopy [9, 10], and CARS microscopy [11]. The different implementations of adaptive optics to nonlinear microscopy can be roughly classified into two approaches: feedback via two-photon excited fluorescence light or feedback via reflected excitation light. Most fluorescence light feedback systems are based on maximizing signal strength, for example, by varying the shape of the deformable mirror via genetic algorithms [12, 13], or image-based algorithms [14]. In addition, the choice of performance parameters for feedback control using genetic algorithm (e.g., brightness, contrast, and resolution) have been investigated [15]. As an alternative approach, a differential aberration imaging technique has been demonstrated by rejecting out-of-focus fluorescence background signals by using a defocused image [16]. For feedback control using reflected excitation light, most implementations utilize

[1] This chapter was modified from Ref. 36 with the permission of the publisher.

the coherent nature of the reflected light and incorporate a wavefront sensor component. A major challenge in applying wavefront sensing in nonlinear microscopes with inherent 3D resolution is to select the reflected light signal preferentially from the focal plane of interest but not throughout the optical path of the excitation light. In one approach, Rueckel and co-workers used coherence-gated wavefront sensing method [17, 18]. This approach utilizes the low temporal coherence properties of femtosecond laser pulses. The reflected light signal from the focal plane is selected interferometically via a modified Michelson interferometer and the wavefront distortion is quantified using a shear interferometer.

In this work, we demonstrate an alternative method for adaptive correction in two-photon microscopy via reflected light feedback utilizing confocal principle for depth selection. This approach simplifies the optics in the wavefront detection light path and reduces the potential of inducing additional aberrations. Further, we utilize a Shack-Hartmann wavefront sensor that allows the wavefront distortion to be monitored by acquiring a single image improving the bandwidth of the adaptive optics feedback loop.

2.2. Methods and Experimental Setup

This two-photon microscope with adaptive optics compensation was constructed by modifying an existing system as previously described [2]. The major additional components consist of a large dynamic range deformable mirror, a Shack-Hartmann wavefront sensor, and a confocal light path for reflected light detection.

2.2.1. A large dynamic range deformable mirror

The deformable mirror (Mirao52d, Imagine Optic, Orsay, France) includes a silver-coated reflective membrane coupled 52 miniature voice-coil type actuators. The diameter of its pupil is 15.0 mm and it has 200 Hz bandwidth. The maximum wavefront amplitude that can be generated is ±50 μm with ±1 V

voltage range. An important feature of this deformable mirror is its large dynamic range. It can generate mimic Zernike modes up to 4th order and partially up to 6th order.

2.2.2. The detection of the wavefront distortion with a Shack-Hartmann wavefront sensor

The Shack-Hartmann wavefront sensor (HASO32, Imagine Optic, Orsay, France) consists of a lenslet array and a CCD sensor. It has 32×32 lenslets within 3.6×3.6 mm2 rectangular aperture. Its bandwidth is 20 Hz. With an incident plane wave, an array of foci produces a rectilinear grid defined by the lenslet dimension. However, if the incoming wavefront is distorted, the foci are displaced from the grid location. By measuring the distance of the displacement using a CCD camera, the slope of local wavefront can be calculated and the whole wavefront can be constructed. The advantage of the Shack-Hartmann sensor is its ability to rapidly quantify wavefront aberration with a single image.

2.2.3. The application confocal detection to select reflected light signal from the focal plane

Only the aberration information of light from the focal region of the objective is relevant for optimizing two-photon excitation. However, the reflected light signal is not only produced at the focal plane, but also from out-of-focal regions. The signal from out-of-focal regions needs to be eliminated, and we accomplished it by setting up a confocal detection light path. The confocal pinhole passes the signal originating from the focal region of the objective while blocking the out-of-focus light at the confocal pinhole. The depth selectivity, axial resolution, should be optimized by selecting a small pinhole [19, 20]. However, this requirement must be traded-off against the fact that the pinhole also acts as a spatial filter. A very small pinhole will filter out all higher spatial frequency information of the distorted wavefront needed for adaptive correction. These two conflicting requirements must be balanced in our system. The optimization of the pinhole size will be discussed in the next section.

2.2.4. Overall Instrument Configuration

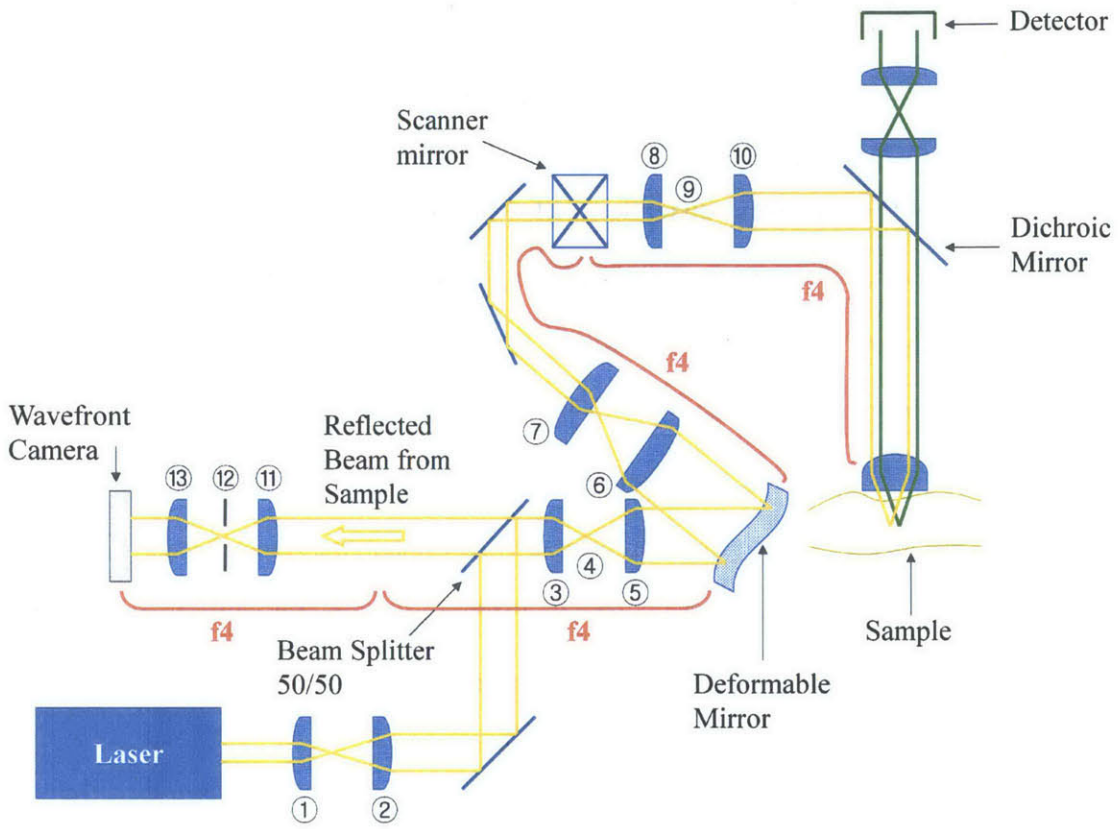

Fig 2.1. System configuration. The components used are Ti-Sapphire (Ti-Sa) laser (Tsunami, Spectra-Physics, Mountain View, CA), plano-convex lens L1 (focal length 50 mm, KPX082AR.16, Newport, Irvine, CA), L2 (f 200 mm, KPX106AR.16, Newport), L3 (f 100 mm, KPX094AR.16, Newport), L5 (f 200 mm, KPX106AR.16, Newport), L6 (f 400 mm, KPX115AR.16, Newport), L7 (f 50 mm, KPX082AR.16, Newport), L8 (f 20 mm, 444232, Zeiss, Thornwood, NY), L10 (f 125 mm, KPX097AR.16, Newport), L11 (f 200 mm, KPX106AR.16, Newport), L13 (f 100 mm, KPX094AR.16, Newport), silver coated mirrors (10D20ER.2, Newport), beam splitter (10BC17MB.2, Newport), deformable mirror (Mirao52d, Imagine Optic, Orsay, France), scanning mirrors (6350, Cambridge Technology, Lexington, MA), short-pass dichroic mirror (650dcxxr, Chroma Technology, Rockingham, VT), objective lens (Fluar, 1.3 NA, Zeiss), photomultiplier detector (R7400P, Hamamatsu, Bridgewater, NJ), pinhole (P150S, Thorlabs, Newton, NJ), and wavefront camera (HASO32, Imagine Optic).

Fig 2.1 describes the general experimental setup. The laser source was a Ti-Sapphire (Ti-Sa) laser (Tsunami, Spectra-Physics, Mountain View, CA) pumped by a frequency doubled Nd:YVO4 laser (Millennia V, Spectra-Physics, Mountain View, CA). The excitation light was reflected by the deformable

mirror (Mirao52d, Imagine Optic, Orsay, France), positioned at a conjugate plane of the back aperture of the microscope objective, towards the excitation optical path of a typical two-photon laser scanning microscopy [2]. The emission fluorescence signal passing a short-pass dichroic mirror and a short pass barrier filter (650dcxxr and E700SP, Chroma Technology, Rockingham, VT) was incident upon a photomultiplier detector (R7400P, Hamamatsu, Bridgewater, NJ) and the associated single photon counting circuitry. The scattered light signal was reflected by the dichroic scanner, descanned by passing through the scanning mirrors, and directed toward the wavefront camera (HASO32, Imagine Optic, Orsay, France). The wavefront camera was also positioned at a conjugate plane of the microscope objective back aperture. Before the wavefront camera, a confocal pinhole (P150S, Thorlabs, Newton, NJ) was positioned at a plane conjugated to the microscope focal plane selecting depth-resolved reflected light signal.

As described above, a small pinhole is necessary for good axial resolution. However, the pinhole also should be sufficiently large to pass the spatial frequency information contained in the distorted wavefront. We set the minimum pinhole size based on the highest spatial frequency that the deformable mirror can generate because higher order distortion cannot be corrected in any case. The distances between the two actuators on the deformable mirror is 2.5 mm corresponding to a minimum spatial period of 5 mm. Fourier transform of this spatial period gives a maximum spatial frequency that needs to pass through the wavefront detection light path. We determined that a confocal aperture with diameter no less than 125 μm placed at plane 12 of Fig 2.1 would transmit all the relevant aberration information. However, we chose to use a 150 μm diameter pinhole to provide some additional margin of error. It is necessary to examine what axial resolution is afforded by this 150 μm diameter pinhole. Accounting for the magnification of the intermediate lenses, the 150 μm pinhole at plane 12 corresponds to an effective aperture of 37.5 μm radius at plane 9 of Figure 1. At plane 9, the axial resolution is related to the aperture size by equation (1) [21]:

$$d_z(3dB)_{plane} = \frac{a\sqrt{2}}{M \sin\theta_0} \tag{1}$$

where a is the radius of the aperture (37.5 μm), sinθ0 is NA/n = 1.3/1.518 = 0.856 for an oil immersion objective lens (Fluar, 1.3 NA, Zeiss, Thornwood, NY), NA is the numerical aperture of the objective lens, n is the index of refraction of medium, and M is the magnification. Since the focal length of lens 10 is 125 mm, the effective magnification M is 30.3. This results in an axial resolution of about 2.0 μm. This is resolution more than sufficient because the back aperture of the objective is underfilled corresponding to an effective axial resolution of 4.8 μm, to be discussed later in section 3.2.

By measuring the wavefront distortion, the wavefront camera provided feedback signal to the deformable mirror. The deformable mirror generated a pre-distortion to the plane wave that countered the distortion induced by the sample. The pre-distortion from the deformable mirror and the distortion from the sample were cancelled out to produce a more ideal point spread function at the focal point. It should be noticed that the light that was detected by the wavefront camera passed the deformable mirror twice while the actual incoming excitation light to a sample passed the deformable mirror once. Under the assumption the specimen is highly scattering, this is the appropriate optical configuration since the detected light also got aberrated twice by the sample in reflected light mode. Therefore, with close loop control, the adaptive optics compensation worked with the pre-distorted excitation light before the sample producing a flat wavefront at the wavefront camera after the feedback system reaches steady state.

Fig 2.2 and Fig 2.3 show representative wavefronts and aberration coefficients before and after adaptive optics compensation. The wavefront sensor provides the deformable mirror with the feedback signal satisfying 4 fold of Nyquist–Shannon sampling criterion. Therefore, the adaptive optics system can correct the wavefront up to the maximum capability of the deformable mirror, which is under 10 nm RMS error according to its specification.

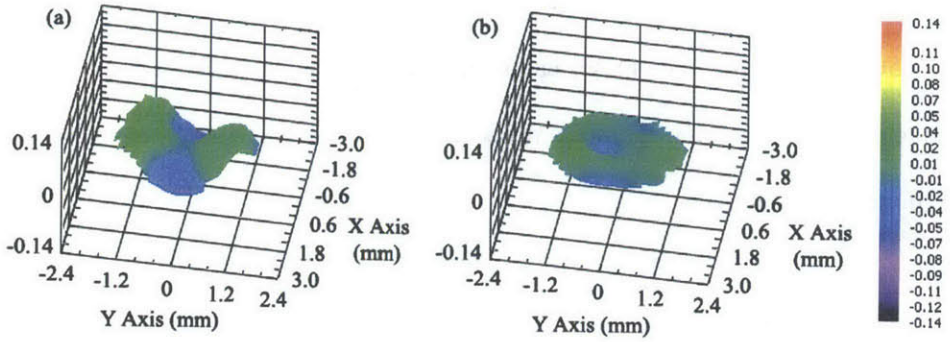

Fig 2.2. Wavefront change after the AO compensation. The sample is a mouse heart (described in 3.4) and imaged at 20 μm depth. (a) Distorted wavefront without the compensation. (b) Wavefront after the AO compensation.

(a)	Astigmatism at 0°	-0.0411	(b)	Astigmatism at 0°	-0.0120
	Astigmatism at 45°	0.0198		Astigmatism at 45°	0.0005
	Coma at 0°	0.0051		Coma at 0°	-0.0047
	Coma at 90°	-0.0087		Coma at 90°	-0.0012
	3th order spherical aberration	-0.0048		3th order spherical aberration	-0.0072

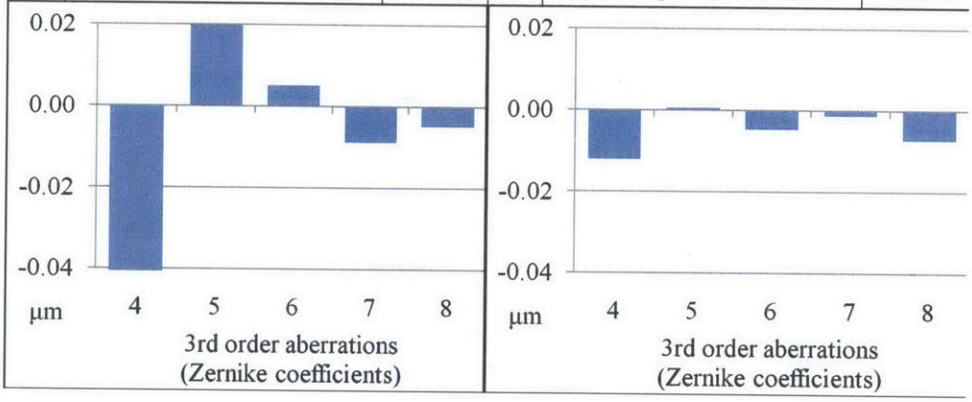

Fig 2.3. 3rd order aberration coefficients change after the AO compensation. (a) Uncompensated coefficients corresponding to Fig 2.2(a). X-axis represents Zernike coefficients; 4 is Z2,2, 5 is Z2,-2, 6 is Z3,1, 7 is Z3,-1, and 8 is Z4,0. The error of the wavefront measurement is less than 2 nm. (b) Compensated coefficients.

It should be also noted that our method holds only when the sample is highly scattering, which is often, but not always, the case in biological samples. For a more reflective sample, the measured wavefront is dependent on whether the aberrations generated by the sample are odd (asymmetric) or even (symmetric), which was extensively discussed in the references [22, 23, 24]. For a reflective sample with the odd aberrations, this system configuration gives incorrect wavefront measurement.

In our system configuration, there are the losses of excitation laser power and reflected light signal due to the use of the 50/50 beam splitter. The losses can be avoided by using a polarizing beam splitter followed by a quarter-wave plate [8]. This configuration reflects 100% of the excitation laser power instead of 50% in the absence of multiple scattering.

2.3. Experiment and Result

To thoroughly quantify the performance of our adaptive optics system, we have devised a series of experiments using artificial and biological specimens. Two artificial specimens with large aberration were prepared and used to evaluate our adaptive optics system in terms of minimizing signal loss and optimizing image resolution loss. Further, the performance of this adaptive optics system was evaluated in three typical biological tissue specimens: mouse tongue muscle, heart muscle, and brain slice.

2.3.1. Signal loss due to aberrations as a function of imaging depth

This experiment was designed to measure the signal loss due to aberration as a function of imaging depth and the compensatory performance of the adaptive optics system. A 20x air objective lens (Fluar, 0.75 NA, Zeiss, Thornwood, NY) was intentionally used to image into aqueous fluorescein samples with varying thickness, 50, 100, and 150 μm [Fig 2.4]. A mirror (10D20ER.2, Newport, Irvine, CA) was placed at the bottom of the specimen to enhance reflected light signal. A femtosecond pulsed laser (Tsunami, Spectra-Physics, Mountain View, CA) was used to provide 780 nm excitation light. The two-photon excitation focal volume was placed just above the mirror surface within 1~2 μm. The refractive index mismatch between the air objective and the aqueous specimen resulted in the generation of significant aberration, especially spherical aberration [25, 26]. As the focus went deeper, the signal loss became higher. The signal loss was measured with a normal two-photon excitation fluorescence microscope with and without the adaptive optics compensation and the two signal losses were compared.

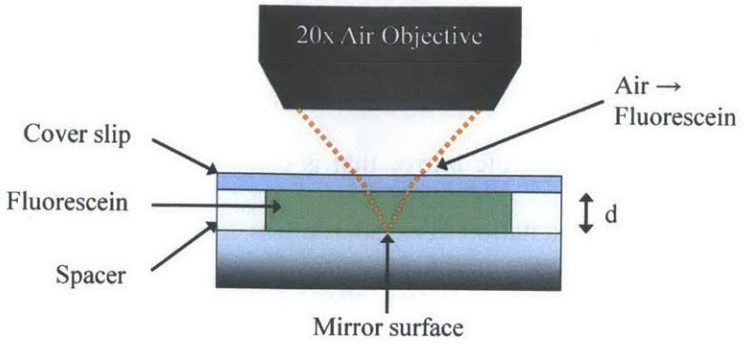

Fig 2.4. Signal loss experiment sample

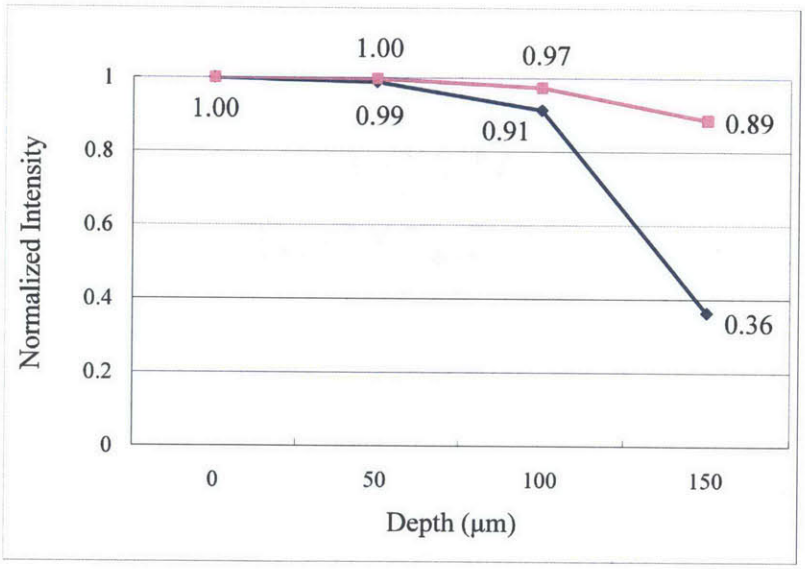

Fig 2.5. Signal loss improvement. The ranges of error bars are smaller than their symbols.

Fig 2.5 shows the result of the fluorescein emission signal loss experiment. The uncompensated signal is the blue line and the compensated signal is the pink line. The uncompensated signal decreased with increasing focus depth. However, with adaptive optics compensation, the emission signal remained almost constant. The signal improvement was 1% at 50 μm, 7% at 100 μm, and 147% at 150 μm. At 150 μm, the maximum Zernike coefficient of the uncompensated aberration among the 3rd order aberrations

was 0.39 μm, but it became 0.10 μm with the adaptive optics compensation. The Zernike coefficient for spherical aberration (Z4,0) was reduced from 0.036 μm to 0.004 μm. The maximum aberration was astigmatism instead of the spherical aberration and it may be caused either by slight misalignment of the lenses or by slight bending of the dichroic mirror that is common in some microscope dichroic mirror holders [27, 28]. In addition, the excitation laser source was linearly polarized in front of the sample instead of circular polarization and it is known that scattering depends on polarization direction. Therefore, linearly polarized excitation light may generate erroneous astigmatism [18].

2.3.2. Point spread function degradation due to aberrations as a function of imaging depth

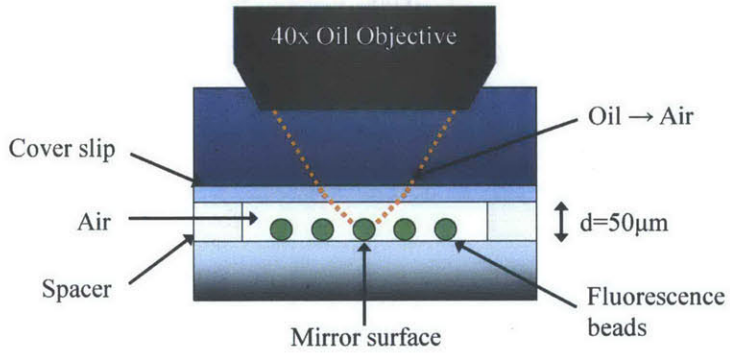

Fig 2.6. PSF degradation experiment sample

In this experiment, we tried to quantify point spread function degradation due to aberrations as a function of imaging depth and the compensatory performance of the adaptive optics system. A 40x oil immersion objective lens (Fluar, 1.3 NA, Zeiss, Thornwood, NY) was used to image 0.1 μm diameter fluorescence beads (F8803, Invitrogen, Eugene, OR) deposited on a mirror though an air gap of 50 μm [Fig 2.6]. The mirror was used to enhance reflected light signal. The excitation wavelength was 780 nm. Spherical aberration was again generated due to index mismatch between the oil objective and the air specimen.

The point spread function was measured with a normal two-photon excitation fluorescence microscope with and without the adaptive optics system.

Fig 2.7 shows the effect of aberration on PSF laterally and axially. The blue bar shows the uncompensated resolution and the pink bar shows the compensated resolution. Clearly, when the air gap thickness is zero, no compensation is necessary. At 50 μm air gap, lateral resolution was improved by 12% and axial resolution was improved by 38%. Lateral resolution is proportional to 1/NA and axial resolution is proportional to 1/NA2, so it is a reasonable result that axial resolution was affected more than lateral resolution with the adaptive optics compensation. The Zernike coefficient of the uncompensated maximum aberration had been 0.44 μm, but it became 0.09 μm with compensation. The Zernike coefficient for spherical aberration (Z4,0) became from 0.14 μm to 0.02 μm. Here the reason that the spherical aberration was not the maximum value among the 3rd order aberrations may be again due to reasons cited in the previous section.

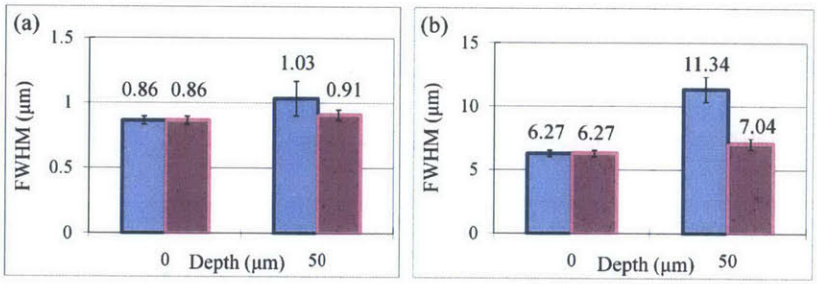

Fig 2.7. Resolution (full-width at half-maximum: FWHM) change after AO compensation. (a) Lateral resolution change. (b) Axial Resolution change.

Further, we should note that the lateral and axial resolutions were larger than the values of diffraction limited resolutions. It was because the objective lens was underfilled by the excitation light. As we mentioned with the system configuration, the deformable mirror gives same compensation to the input beam and the outgoing beam from the sample. The two beams should be located exactly at the same area on the deformable mirror, so their beam sizes should be same and the objective was just filled with the

excitation light. However, because of the Gaussian characteristic of the laser beam, the objective lens was practically underfilled and the lateral and axial resolutions became larger. According to the experimental result, the effective NA of the objective was about 0.55 in our experimental setup although its theoretical NA is 1.3, which is valid only when immersion oil is present under the objective lens until a cover slip, and a sample is then just below the cover slip in a refractive index of 1.5. This current limitation may be removed by utilizing a top-hat wavefront shaper or modifying the adaptive optics feedback algorithm to ignore information from the peripheral region of the wavefront sensor.

2.3.3. Mouse tongue muscle imaging using AO compensated two-photon microscopy

The mouse tongue musculature was visualized based on both endogenous fluorescence and second harmonic generation. The whole tongue excised from a female C57BL/6 mouse (10 weeks old) was fixed in phosphate buffered saline (PBS, pH 7.4) containing 2.5% glutaraldehyde for about a day. The fixed tongue tissue was then immersed in PBS for 3 hours, rinsed with the same buffer excessively and finally embedded in paraffin without a cover slip. The wavelength of the excitation light was set to 780 nm. The objective lens was a 40x oil immersion objective lens (Fluar, 1.3 NA, Zeiss, Thornwood, NY). The emission signal was filtered by a green filter (535/40, Chroma Technology, Rockingham, VT). The field size was 120 μm×120 μm with 256×256 pixels and the dwell time was 40 μs. As representative images, Fig 2.8 shows mouse tongue muscles images at 80 μm depth with and without the adaptive optics compensation. The left image is the uncompensated image and the right one is the compensated image and they were processed with background rejection. The threshold for each image was set to three times the intensity level measured in regions outside objects of interest (e.g. blood vessels in the mouse heart or the neurons in the mouse brain).

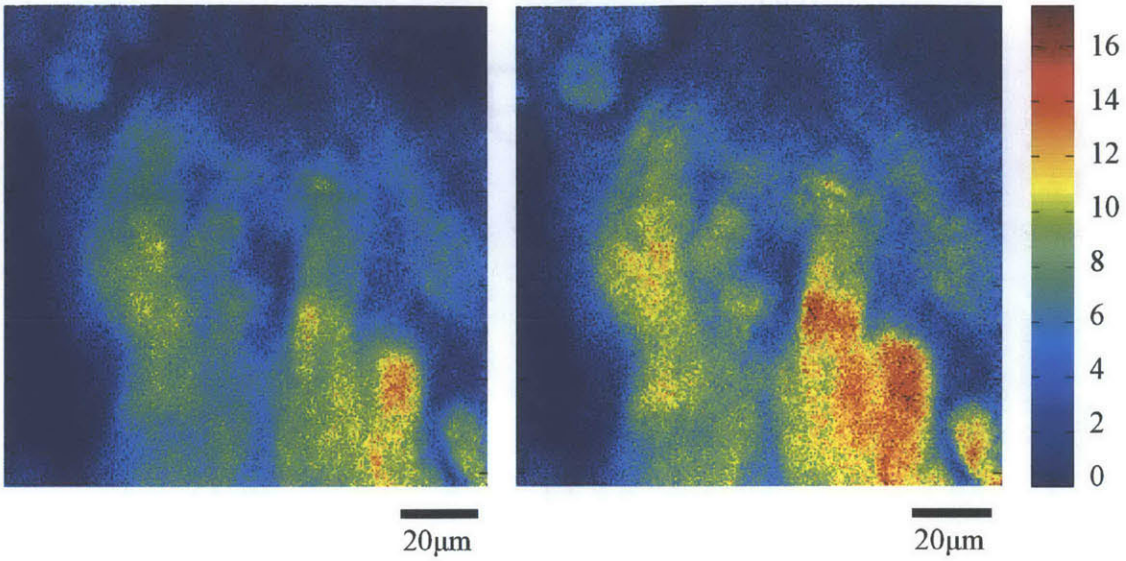

Fig 2.8. Mouse tongue images at 80 μm depth without / with AO compensation

In principle, the bandwidths of the wavefront camera and the deformable mirror are about 20 Hz and 200 Hz respectively. However, the current feedback algorithm takes significant CPU resource and it leads to a compensation time of 4~5 seconds. Therefore, the algorithm is the bottleneck for the bandwidth of the whole compensation process and it is far from practical for pixel-by-pixel correction over the whole image. Instead, with the assumption that the optical paths are similar over the scanned area of the image, adaptive optics compensation was performed only at the center pixel of the image and the rest of the image was acquired with the same deformable mirror shape setting [29]. In future studies, it would be interesting to determine the optimal number of pixels that should be corrected per image given the trade-off between imaging speed and tissue heterogeneity. It would also be interesting to improve imaging speed by developing faster, more efficient feedback algorithm or by utilizing higher performance computer hardware.

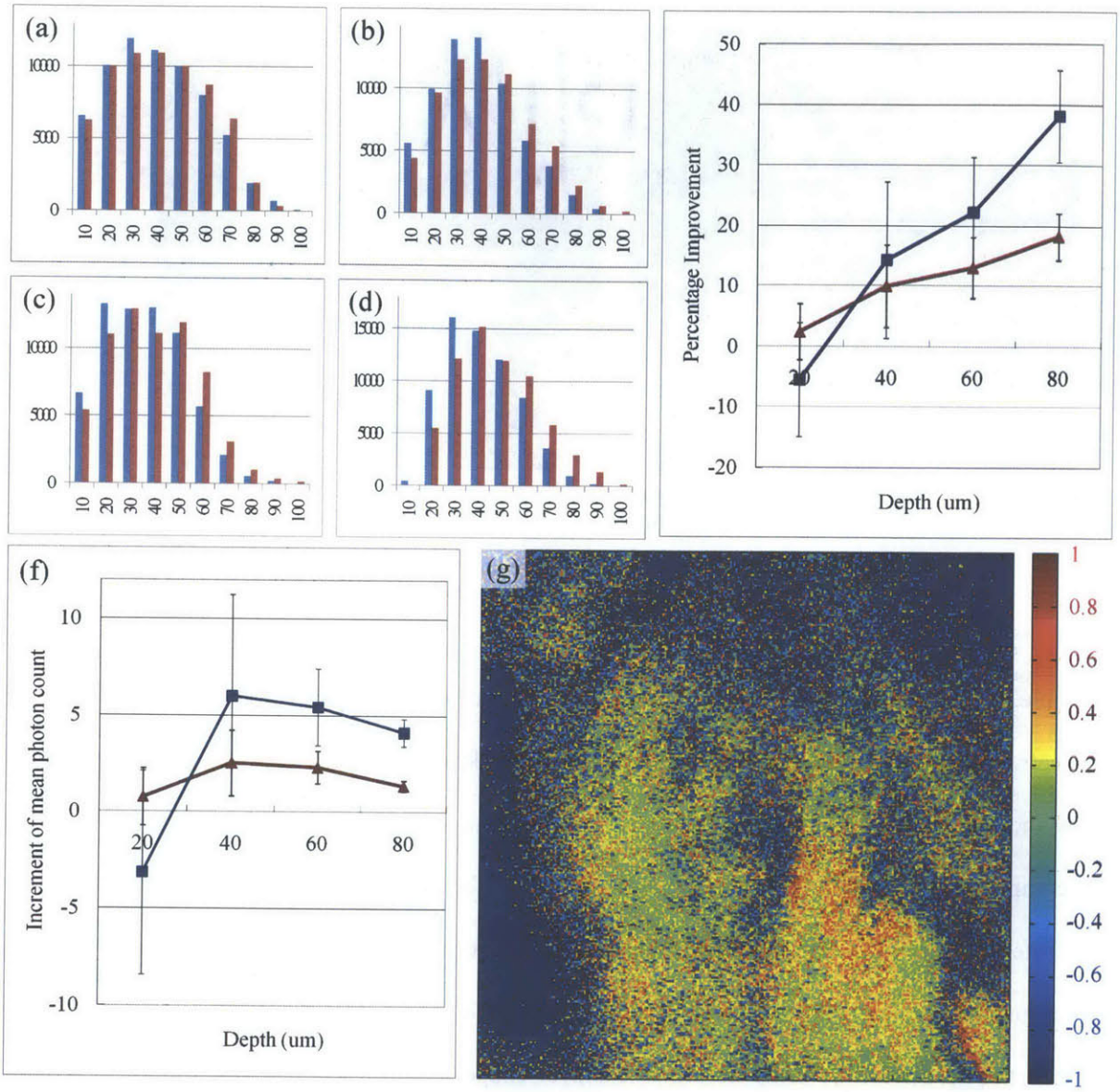

Fig 2.9. Signal improvement after AO compensation. (a) ~ (d) show histograms for number of pixels according to their intensity; x-axis represents intensity of the pixels. For example, 10 means the pixels that have 0~10% intensity of the maximum in the whole image, and 100 means 90~100% intensity pixels. Y-axis represents the number of pixels in the intensity range. The blue bars show the number of pixels before the compensation, and red bars show the result after the compensation. Each histogram was normalized to itself. (a) shows the distribution at 20 μm depth, (b) at 40 μm, (c) at 60 μm, and (d) at 80 μm imaging depth. (e) Percentage improvement according to imaging depth. Red line shows the improvement with background rejection (only fluorescent area was calculated), and blue line shows the improvement only with 90~100% intensity pixels. (f) Increment of mean photon count. Red and blue lines show same data sets as (e). (g) Improvement based on each pixel. Any pixel with more than 2 fold

improvement, that comes from mismatch of the uncompensated and compensated image, is saturated to red color. The background is set to -1 for visualization purpose.

The compensated image shows higher signal strength than the uncompensated one. To compare the signal intensity of two images, intensity distributions for all pixels were calculated. Fig 2.9(a) ~ (d) show the histograms for the intensity distributions before and after the compensation. It was shown that the number of brighter pixels increased, and the number of darker pixels decreased for all imaging depths after the compensation, which means the in-focus fluorescence signals were improved while the out-of-focus fluorescence signals were suppressed. To find the improvement trend according to imaging depth, mean photon counts were calculated with background rejection. Fig 2.9(e) shows the percentage improvement from the mean photon counts according to imaging depth. The percentage improvement shows that at greater imaging depth, the improvement becomes larger, so the improvement for 90~100% intensity pixels was 38.1% at 80 μm depth. Fig 2.9(f) shows the increment of mean photon count. In term of the increment of photon count, the result at 40 μm depth shows the greatest improvement than at greater depths. At shallow depth, there is not much to compensate and at greater depths the overall signal is significantly lower due to scattering attenuation of both excitation and emission photons [30]. Fig 2.9(g) shows the percentage improvement based on each pixel at 80μm depth calculated from Fig 2.8. Comparing the degree of improvement on the center vs. the edge, no major difference is observed. From all over the region where the fluorescence signal is generated, the improvement seems quite uniform. This may be because the aberration from the optical system is much larger than the aberration from the sample.

2.3.4. Mouse heart muscle imaging using AO compensated two-photon microscopy

As a second example, we imaged mouse heart muscular structures with nuclei based on endogenous fluorescence, second harmonic generation and exogenous labeling. Through tail-vein injection (in conjunction with an overdose of anesthetics), nuclei are labeled with Hoechst while the extracellular matrix around the cells were labeled with Texas-Red maleimide. After staining, the heart was excised and

was fixed in 4% paraformaldehyde and embedded in paraffin without a cover slip after some histological processing. The wavelength of the excitation light was 780 nm. The objective lens was a 40x oil immersion objective lens (Fluar, 1.3 NA, Zeiss, Thornwood, NY). The emission signal was filtered by a green filter (535/40, Chroma Technology, Rockingham, VT). The field size was 120 μm×120 μm with 256×256 pixels and the dwell time was 40 μs. Fig 2.10 shows representative images of mouse heart at 80 μm depth with and without the adaptive optics compensation. The left image is the uncompensated image and the right one is the compensated image. As in the mouse tongue experiment, adaptive correction was only performed at the center pixel of the image and the same deformable mirror shape was held constant throughout the whole image.

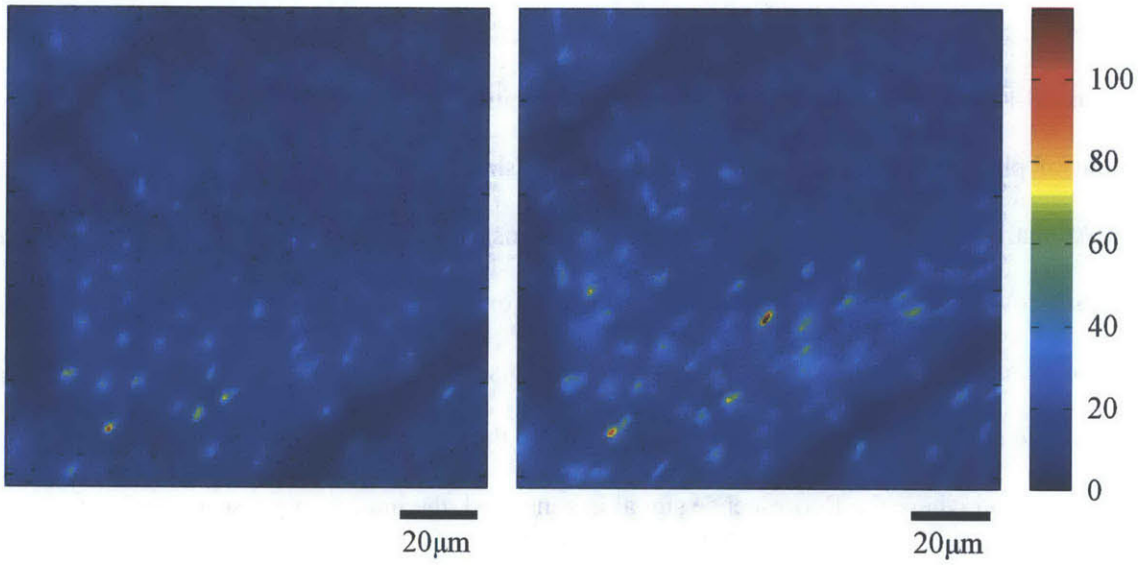

Fig 2.10. Mouse heart images at 80 μm depth without / with AO compensation

To compare the signal intensity of two images, the intensity distributions for all pixels were calculated again. Fig 2.11(a) ~ (d) show the histograms for the intensity distributions before and after the compensation. The same trend was shown as the mouse tongue result; the number of brighter pixels increased, and the number of darker pixels became less for all imaging depths after the compensation. To

find the improvement trend according to imaging depth, mean photon counts were calculated with background rejection. Fig 2.11(e) shows the percentage improvement from the mean photon counts according to imaging depth. The percentage improvement shows that as the imaging plane went deeper, the improvement became larger in general. The maximum improvement of the 90~100% intensity pixels was 123% at 80 μm depth.

In terms of the increment of photon count, the result at 20 μm depth showed the greatest increase due to the generally higher signal level. At greater depth, scattering of excitation and emission photon again dominated and the improvement due to using adaptive optics became less significant. In terms of improvement on the center compared to edge, it seemed to be uniform similar to the mouse tongue result.

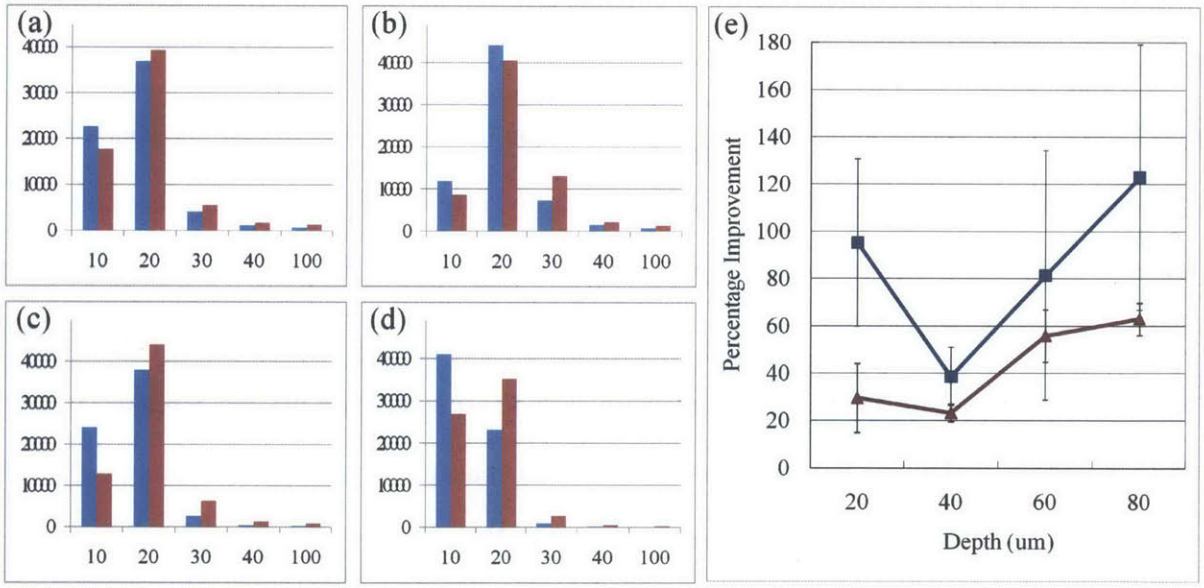

Fig 2.11. Signal improvement after AO compensation. (a) ~ (d) show histograms for number of pixels according to their intensity; x-axis represents the intensity of pixels same as Fig 2.9 except 100 (100 means 40~100% intensity pixels in the image). Y-axis represents the number of pixels in the intensity range. The blue bars show the number of pixels before the compensation, and red bars show the result after the compensation. Each histogram was normalized to itself. (a) shows the distribution at 20 μm depth, (b) at 40 μm, (c) at 60 μm, and (d) at 80 μm imaging depth. (e) Percentage improvement according to imaging depth. Red line shows the improvement with background rejection (only fluorescent area was calculated), and blue line shows the improvement only with 90~100% intensity pixels.

2.3.5. Neuronal imaging in mouse brain slices using AO compensated two-photon microscopy

Both muscle tissues have high scattering coefficients that appear to be the major limiting factor in two-photon imaging depth. It is interesting to also study tissue specimen that has significantly lower scattering and allows deeper imaging. For this propose, we chose mouse brain slices with neurons expressing GFP protein driven by thy-1 promoter. Adult thy1-GFP-S mice were perfused transcardially with 4% paraformaldehyde in PBS. Brains were removed and postfixed overnight in 4% paraformaldehyde in PBS, then coronally sectioned at 200 μm using a vibratome. The wavelength of the excitation light was 890 nm, and a 40x water immersion objective lens (Achroplan IR, 0.8 NA, Zeiss, Thornwood, NY) was used with No. 1½ cover slip. The emission signal was filtered by a green filter (535/40, Chroma Technology, Rockingham, VT). The field size was 120 μm×120 μm with 256×256 pixels and the dwell time was 40 μs.

Fig 2.12 shows representative mouse brain images at 50 μm depth with and without the adaptive optics compensation. The mouse brain specimen contained sparsely distributed gfp expressing neurons. The left image is the uncompensated image and the right one is the compensated image. The adaptive optics compensation was performed at the center of the whole view and scanning was done with the same deformable mirror shape. The compensated image showed higher signal than the uncompensated one. To compare the signal level of two images, the intensity distributions for all pixels are shown in Fig 2.13. Fig 2.13(a) and (b) show the histograms for the intensity distributions before and after the compensation. Since the structure imaged is sparse, the histogram is dominated by the zero intensity pixels. Therefore, two additional figures below (a) and (b) are added to show histogram distributions excluding the lowest intensity range.

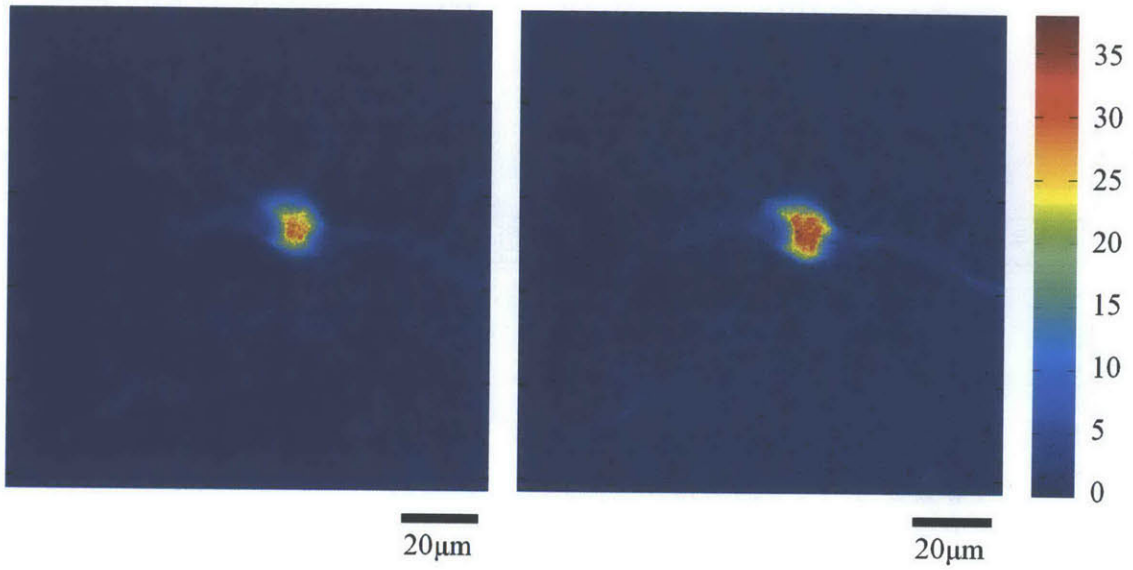

Fig 2.12. Mouse brain images at 50 μm depth without / with AO compensation

Again, the number of brighter pixels increased and the number of darker pixels decreased after the adaptive optics compensation. For the improvement trend according to imaging depth, mean photon counts were calculated with background rejection. Fig 2.13(c) shows the percentage improvement from the mean photon counts according to imaging depth. We see a general trend of increasing percentage improvement as a function of imaging depth similar to the other two tissue cases. Since the scattering coefficient in the brain is much less than that of muscles, the achievable imaging depth is deeper with equivalent excitation power. However, the improvement at the maximum achievable depth between with and without adaptive optics compensation tissues was similar in all cases ranging up to about 2 fold in terms of the maximum signal strength. In a previous report, fluorescently labeled blood plasma in wild-type zebrafish was imaged [18]. The aberrations introduced by the specimen were mainly astigmatism (254nm) at 200μm imaging depth and fluorescence signal at the center of a blood vessel was improved almost 2 fold by the wavefront correction with the coherence-gated wavefront sensing method. In our measurement, the main aberration was also astigmatism (-125nm) at 150μm imaging depth and the signal improvement was about the same, which was comparable with the previous result.

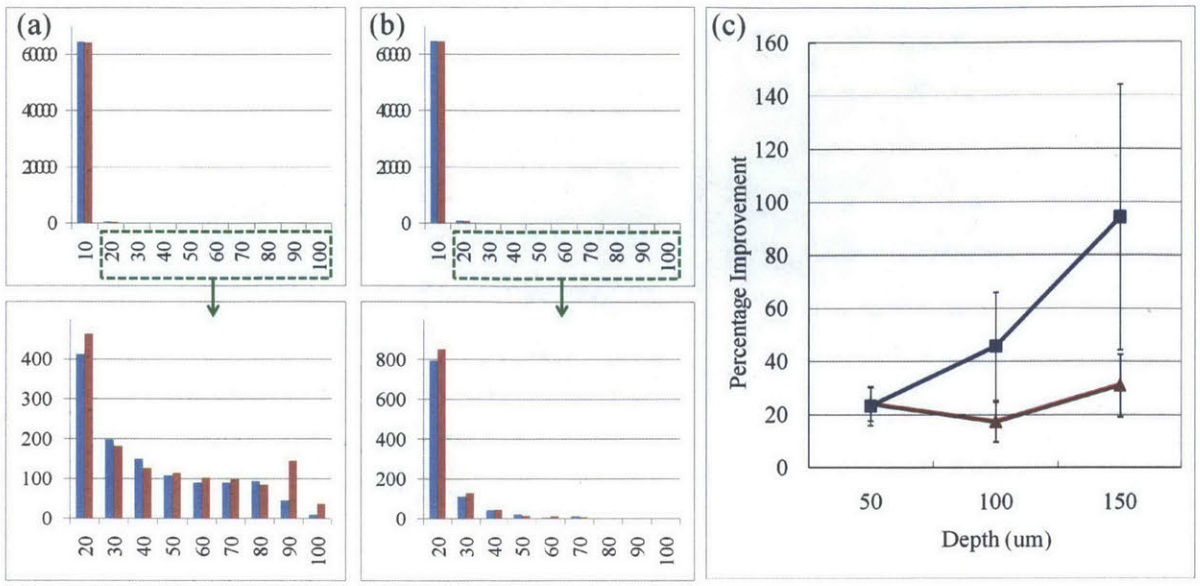

Fig 2.13. Signal improvement after AO compensation. (a) and (b) show histograms for number of pixels according to their intensity; x-axis represents intensity of the pixels, and y-axis represents the number of pixels in the intensity range. The blue bars show the number of pixels before the compensation, and red bars show the result after the compensation. Each histogram was normalized to itself. (a) shows the distribution at 50 μm depth, and (b) at 150 μm imaging depth. The bottom figures of (a) and (b) are detailed distributions in the selected range. (c) Percentage improvement according to imaging depth. Red line shows the improvement with background rejection (only fluorescent area was calculated), and blue line shows the improvement only with 90~100% intensity pixels.

2.4. Conclusion

Wavefront distortion by tissue specimens with inhomogeneous optical properties can be measured by a Shack-Hartmann wavefront sensor using a confocal depth selection mechanism. The measured wavefront distortion can then be corrected by a deformable mirror integrated into the microscope system. In specimens with large aberration, such as the artificial specimens, significant improvement in signal strength and resolution can be achieved. In more realistic tissue specimens, the imaging depth is limited to 100~200 μm depth by the respective scattering coefficients of the respective tissue type. For example, in general, achievable imaging depth for the brain tissue is approximately three times that of muscles. The measured aberration for these tissues at this depth is only on the order of a few λ/10 similar to those

reported by other investigators [18, 31]. The corresponding improvement in terms of signal strength is on the order of 20~70%. However, the improvement on the peak signals (90~100% strength intensity signals) is up to 2 fold. This means the contrast of images was increased after the adaptive optics compensation, therefore the images became more vivid, which is one of the most essential roles of the adaptive optics system in biological imaging.

Our data appear to imply two related conclusions. First, tissue scattering is the primary factor that determines the maximum imaging depth in tissue imaging by two-photon microscope. While the effect of scattering is exponential with depth, the accumulated aberration as a function of depth appears to remain at the same order of magnitude or vary at most linearly. Therefore, scattering effect is always the dominant factor. Second, adaptive optics control can improve imaging signal at depth. However, the typical improvement is relatively modest especially for highly scattering specimen because the very limited imaging depth implies relative little accumulated aberration limiting the improvement that can be obtained by the use of adaptive optics correction. These conclusions are consistent with most of the adaptive optics compensated nonlinear optical imaging studies. The only exceptions are the application of adaptive optical compensation in CARS microscope. One potential explanation may be that CARS signal is highly dependent on the overlap of the excitation volumes of the pump and probe beams and aberration may results in spatial mismatch. The correction for aberration may optimize volume overlap and results in the observed six fold improvement [11].

It may be then important to ask if adaptive optics correction is important for two-photon microscopy. Our data seems to indicate that for most tissue types with high scattering coefficient and shallow imaging depth, adaptive correction can improve signal strength. However, one should note that if excitation power is not limited and photodamage is not an issue, this level of improvement can be equivalently achieved by less than two fold excitation power increase. In the case that higher excitation power cannot be applied, adaptive optics may provide some improvement although at the expense of an increase in instrument complexity and cost.

It may also be useful to consider what situations adaptive optics correction would be useful for two-photon imaging in. Clearly, in tissue with relatively low scattering coefficients that allows deep imaging, adaptive optics is useful to correct for the larger aberration present in this case. This is of course the well known case with the classic examples of imaging in organs such as the eye [4, 32, 33]. Other potential application areas are tissues that induced unusually high aberrations. Another classic example is the skin where the stratified layers have very different indices of refraction and results in significant aberration even in relatively shallow depth. It would be interesting to examine the possible application of adaptive optics compensation in skin imaging. In addition, there are several other potentially interesting applications of adaptive optics in nonlinear microscopy imaging of tissues.

First, tissue scattering, due to a combination of Rayleigh and Mie processes, is lower for light at longer wavelength region, which corresponds to deeper penetration depth. If the adaptive optics system is combined with a two-photon microscope operating in 1.2~1.3 μm region and imaging near infrared emitting fluorophores, one may achieve deeper imaging in tissues with corresponding higher aberration effect. In this case, one may expect adaptive optics compensation to be more important.

Second, if the scattering effect becomes negligible, then the aberration due to the inhomogeneous refractive index of a sample becomes the major factor for image degradation. One obvious example in specimen with extensive optical clearing that can dramatically decreases tissue scattering by dehydration of the specimen and the addition of index matching medium [34, 35]. Optical clearing reduces scattering by index matching nanometer scale level inhomogeneity in the specimen. With the optical clearing, the imaging depth can clearly be increased by orders of magnitude. Given the deeper imaging depth, potentially adaptive optics system may play a more important role provided that this optical clearing do not similarly eliminate index of refraction inhomogeneity on the optical wavelength scale.

Finally, the adaptive optics system may be important for a number of imaging applications involving microfluidic devices. In the fabrication of many microfluidic devices, the material type or thickness used in the fabrication of the device may not match the requirement of the microscope objectives that are

typically designed for imaging through 0.17 mm thick glass. In these cases, significant aberrations may be induced and the use of an adaptive optics system may result in an improvement in image quality in these devices.

References

1. W. Denk, J. H. Strickler, and W. W. Webb, "2-photon laser scanning fluorescence microscopy," Science 248, 73-76 (1990).
2. P. T. C. So, C. Y. Dong, B. R. Masters, and K. M. Berland, "Two-photon excitation fluorescence microscopy," Annual Review of Biomedical Engineering 2, 399-429 (2000).
3. F. Rigaut, G. Rousset, P. Kern, J. C. Fontanella, J. P. Gaffard, F. Merkle, and P. Lena, "Adaptive optics on a 3.6-M telescope - results and performance," Astronomy and Astrophysics 250, 280-290 (1991).
4. J. Z. Liang, D. R. Williams, and D. T. Miller, "High resolution imaging of the living human retina with adaptive optics," Investigative Ophthalmology & Visual Science 38, 55-55 (1997).
5. M. J. Booth, M. A. A. Neil, and T. Wilson, "Aberration correction for confocal imaging in refractive-index-mismatched media," J. Microsc.-Oxf. 192, 90-98 (1998).
6. M. J. Booth, M. A. A. Neil, R. Juskaitis, and T. Wilson, "Adaptive aberration correction in a confocal microscope," Proc. Natl. Acad. Sci. U. S. A. 99, 5788-5792 (2002).
7. M. A. A. Neil, R. Juskaitis, M. J. Booth, T. Wilson, T. Tanaka, and S. Kawata, "Adaptive aberration correction in a two-photon microscope," J. Microsc.-Oxf. 200, 105-108 (2000).
8. P. N. Marsh, D. Burns, and J. M. Girkin, "Practical implementation of adaptive optics in multiphoton microscopy," Opt. Express 11, 1123-1130 (2003).
9. P. Villoresi, S. Bonora, M. Pascolini, L. Poletto, G. Tondello, C. Vozzi, M. Nisoli, G. Sansone, S. Stagira, and S. De Silvestri, "Optimization of high-order harmonic generation by adaptive control of a sub-10-fs pulse wave front," Opt. Lett. 29, 207-209 (2004).
10. A. Jesacher, A. Thayil, K. Grieve, D. Debarre, T. Watanabe, T. Wilson, S. Srinivas, and M. Booth, "Adaptive harmonic generation microscopy of mammalian embryos," Opt. Lett. 34, 3154-3156 (2009).
11. A. J. Wright, S. P. Poland, J. M. Girkin, C. W. Freudiger, C. L. Evans, and X. S. Xie, "Adaptive optics for enhanced signal in CARS microscopy," Opt. Express 15, 18209-18219 (2007).
12. O. Albert, L. Sherman, G. Mourou, T. B. Norris, and G. Vdovin, "Smart microscope: an adaptive optics learning system for aberration correction in multiphoton confocal microscopy," Opt. Lett. 25, 52-54 (2000).
13. L. Sherman, J. Y. Ye, O. Albert, and T. B. Norris, "Adaptive correction of depth-induced aberrations in multiphoton scanning microscopy using a deformable mirror," J. Microsc.-Oxf. 206, 65-71 (2002).
14. N. Ji, D. E. Milkie, and E. Betzig, "Adaptive optics via pupil segmentation for high-resolution imaging in biological tissues," Nat. Methods 7, 141-U184.
15. S. P. Poland, A. J. Wright, and J. M. Girkin, "Evaluation of fitness parameters used in an iterative approach to aberration correction in optical sectioning microscopy," Appl. Optics 47, 731-736 (2008).
16. A. Leray and J. Mertz, "Rejection of two-photon fluorescence background in thick tissue by differential aberration imaging," Opt. Express 14, 10565-10573 (2006).
17. M. Feierabend, M. Rueckel, and W. Denk, "Coherence-gated wave-front sensing in strongly scattering samples," Opt. Lett. 29, 2255-2257 (2004).
18. M. Rueckel, J. A. Mack-Bucher, and W. Denk, "Adaptive wavefront correction in two-photon microscopy using coherence-gated wavefront sensing," Proc. Natl. Acad. Sci. U. S. A. 103, 17137-17142 (2006).
19. T. Wilson and A. R. Carlini, "Size of the detector in confocal imaging-systems," Opt. Lett. 12, 227-229 (1987).
20. D. R. Sandison and W. W. Webb, "Background rejection and signal-to-noise optimization in confocal and alternative fluorescence microscopes," Appl. Optics 33, 603-615 (1994).
21. T. R. Corle and G. S. Kino, Confocal scanning optical microscopy and related imaging systems (Academic Press, San Diego, 1996).

22. P. Artal, S. Marcos, R. Navarro, and D. R. Williams, "Odd aberrations and double-pass measurements of retinal image quality," J. Opt. Soc. Am. A-Opt. Image Sci. Vis. 12, 195-201 (1995).
23. P. Artal, I. Iglesias, N. Lopezgil, and D. G. Green, "Double-pass measurements of the retinal-image quality with unequal entrance and exit pupil sizes and the reversibility of the eyes optical-system," J. Opt. Soc. Am. A-Opt. Image Sci. Vis. 12, 2358-2366 (1995).
24. M. J. Booth, "Adaptive optics in microscopy," Philos. Trans. R. Soc. A-Math. Phys. Eng. Sci. 365, 2829-2843 (2007).
25. S. Hell, G. Reiner, C. Cremer, and E. H. K. Stelzer, "Aberrations in confocal fluorescence microscopy induced by mismatches in refractive-index," J. Microsc.-Oxf. 169, 391-405 (1993).
26. P. T. Fwu, P. H. Wang, C. K. Tung, and C. Y. Dong, "Effects of index-mismatch-induced spherical aberration in pump-probe microscopic image formation," Appl. Optics 44, 4220-4227 (2005).
27. H. P. Kao and A. S. Verkman, "Tracking of single fluorescent particles in 3 dimensions - use of cylindrical optics to encode particle position," Biophys. J. 67, 1291-1300 (1994).
28. T. Ragan, H. D. Huang, P. So, and E. Gratton, "3D particle tracking on a two-photon microscope," J. Fluoresc. 16, 325-336 (2006).
29. J. M. Girkin, J. Vijverberg, M. Orazio, S. Poland, and A. J. Wright, "Adaptive optics in confocal and two-photon microscopy of rat brain: a single correction per optical section - art. no. 64420T," in Conference on Multiphoton Microscopy in the Biomedical Sciences VII, (Spie-Int Soc Optical Engineering, 2007), T4420-T4420.
30. P. Theer and W. Denk, "On the fundamental imaging-depth limit in two-photon microscopy," J. Opt. Soc. Am. A-Opt. Image Sci. Vis. 23, 3139-3149 (2006).
31. D. Debarre, E. J. Botcherby, T. Watanabe, S. Srinivas, M. J. Booth, and T. Wilson, "Image-based adaptive optics for two-photon microscopy," Opt. Lett. 34, 2495-2497 (2009).
32. N. Doble, G. Yoon, L. Chen, P. Bierden, B. Singer, S. Olivier, and D. R. Williams, "Use of a microelectromechanical mirror for adaptive optics in the human eye," Opt. Lett. 27, 1537-1539 (2002).
33. A. Roorda, F. Romero-Borja, W. J. Donnelly, H. Queener, T. J. Hebert, and M. C. W. Campbell, "Adaptive optics scanning laser ophthalmoscopy," Opt. Express 10, 405-412 (2002).
34. V. V. Tuchin, Optical clearing of tissues and blood (SPIE Press, 2005).
35. H. U. Dodt, U. Leischner, A. Schierloh, N. Jahrling, C. P. Mauch, K. Deininger, J. M. Deussing, M. Eder, W. Zieglgansberger, and K. Becker, "Ultramicroscopy: three-dimensional visualization of neuronal networks in the whole mouse brain," Nat. Methods 4, 331-336 (2007).
36. J. W. Cha, J. Ballesta, and P. T. C. So, "Shack-Hartmann wavefront-sensor-based adaptive optics system for multiphoton microscopy." J. Biomed. Opt. 15, 046022 (2010).

Chapter 3

Reassignment of Scattered Emission Photons in Multifocal Multiphoton Microscopy

3.1. Introduction

Multiphoton excitation fluorescence microscopy has inherent 3D resolution due to the nonlinear dependence of excitation upon the incident light distribution [1, 2]. Excitation region is localized to a femtoliter volume at the focal point of a high numerical aperture objective lens. Multiphoton excitation fluorescence microscopy is routinely used in a variety of tissue imaging applications due to its excellent imaging depth, high resolution, and lower photo-damage. However, one of the practical limitations of multiphoton excitation fluorescence microscopy is its imaging speed, typically up to a few frames per second. While this imaging speed is sufficient in many cases, several classes' applications require higher imaging speed. These applications include the measurement of dynamic processes including calcium signaling and action potential propagation [3], high throughput image cytometric study of tissue physiology [4-6], and clinical applications where the effects of physiological motion should be minimized.

There are several methods which have already been introduced for the high-speed multiphoton imaging. The first approach is based on using high-speed scanners such as polygonal mirrors [7], resonant mirror scanners [8], or acousto-optical deflectors (AODs) [9-12] instead of galvanometric mirror scanners used in conventional multiphoton microscopes. The high speed scanners can typically achieve the scanning speed up to about 30 frames per second in tissues with a comparable imaging depth as conventional multiphoton microscopy. However, the high speed scanning requires decreasing pixel dwell time resulting

in lower image contrast and poorer SNR. This can be partially compensated by increasing the excitation laser power, but it is not always possible due to the photo-damage on a specimen and excitation saturation [13, 14].

The second method is two-photon wide-field imaging [15, 16]. With the temporal focusing method, two-photon excitation plane is generated instead of a focus, and it realizes scanningless plane by plane imaging resulting in the fastest imaging speed. However, its performance is often limited by the lower axial resolution compared to the conventional multiphoton microscopy and blurring in large depth of tissue imaging due to the scattering of emission photons.

The third method is multifocal multiphoton microscopy (MMM), which is an intermediate approach between the previously described two techniques [17-22]. With a lenslet array or diffractive optical element (DOE) [23, 24], a number of foci are generated simultaneously and scanned together. The size of the whole scanning region corresponds to the sum of the sub-region scanned by each focus. Therefore, the imaging speed can be improved proportionally to the number of foci. One practical limitation for the imaging speed of MMM is available laser power. For typical titanium-sapphire laser with several Watts of output, approximately one hundred foci can be effectively generated for tissue imaging resulting in approximately two orders of magnitude improvement in imaging speed.

Similar to two-photon wide-field imaging, the SNR of multifocal multiphoton microscopy is also limited by the scattering of emission photons in tissues resulting in lower SNR compared to the single focus scanning multiphoton microscopy. The parallelized excitation foci and simultaneous detection requires detectors with spatial resolution that can acquire and distinguish signals from all the foci at the same time. Most multifocal multiphoton microscopes use imaging detectors such as CCD or CMOS cameras. However, when emission photons generated at one focus are scattered in turbid specimen and arrive at the locations of detector surface that record signals from other foci, the SNR of the image suffers. This lower SNR can be compensated by the use of multianode photomultiplier tubes (MAPMT) in descanned detection geometry where each anode of the MAPMT detects signal for each focus [25]. The larger

detection area of the each anode greatly reduces the crosstalk between foci due to the scattering of emission photons and significantly improves the image SNR.

However, with severe scattering in a turbid specimen, especially in large imaging depth, the scattered emission photons still arrive at neighbor anodes and result in ghost images, duplicates of an image acquired by one focus visualized in neighbor sub-images. These scattered emission photons should be reassigned to their original pixels to remove the ghost images and to increase the SNR of the original image. We have shown that this can be accomplished by estimating the scattering matrix at one location of the specimen that characterizes the crosstalk between the anodes of the MAPMT due to emission photon scattering. By applying the inverse of the scattering matrix to the acquired image, an improved SNR picture free from ghost images can be produced.

The estimation of the scattering matrix has been done experimentally [25], [Fig 3.1]. The first method of the estimation is using a tissue phantom with similar optical parameter as real tissue containing sparsely distributed fluorescence particles. These fluorescence particles are imaged by the MMM. The sparsity of the particles ensures that the ghost images of each particle can be identified. Through calculating the relationship between particle intensities in the correct pixel and all its neighbors, the scattering matrix can be calculated. However, the phantom sample is often a poor model of real tissue specimen on the microscopic level where there is significant heterogeneity. This may lead to a significant error in image post-processing. Second, the scattering matrix can be calculated with a real sample by exciting only one focus at a time in the same MMM system. This method gives the exact coefficients for the scattering matrix. However, since the scattering matrix is a function of specimen location due to heterogeneity and depth due to increased scattering, scattering matrix must be measured frequently. This labor intensive measurement process partly negates the speed advantage of applying MMM imaging.

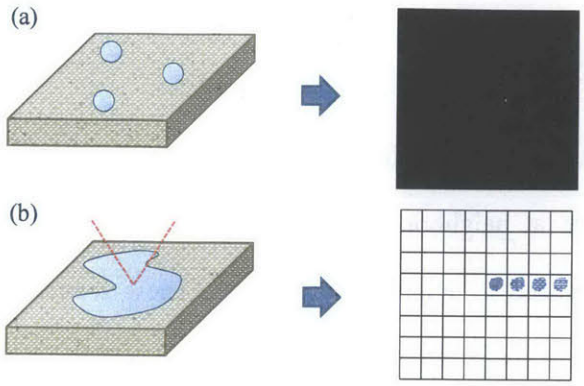

Fig 3.1. Two experimental approaches for the estimation of a scattering matrix. (a) Sparsely distributed beads sample in tissue phantom (2% Intralipid emulsion), and scattering matrix measurement from its MMM image. (b) Single focus excitation on a real sample and scattering matrix measurement from its MMM image.

Here we demonstrate pure image post-processing approach for MMM to estimate the scattering matrix without any additional experimental measurement. The proposed approach is based on maximum likelihood estimation for the quantification of the crosstalk between the different anodes of the MAPMT with utilizing the physical model of the MMM system. This approach provides the reassignment of the photons that are originally detected at wrong anodes and generated in the form of the ghost images, to the actual anode location. Therefore, it provides the improvement in the signal strength and simultaneously the minimization of the ghost images in the neighbor sub-images. Since the proposed approach uses only the primary images generated by the MMM, this allows the characterization of the scattering matrix that is independent of any specimen imaging, location and depth. Mathematical model of the proposed approach is presented and validated first with simulation data where the results show the convergence of the method to the actual fluorophores structures. The performance of the proposed method is then employed for the mouse neuron images where the results are quantitatively analyzed.

3.2. Methods

3.2.1. MMM configuration

We have developed two MMM systems; one with 45 μm foci separation, and the other with 85 μm foci separation. Fig 3.2 shows the schematic of the MMM with 85 μm foci separation based on a diffractive optical element (DOE) for multiple foci generation and the MAPMT in descanned detection geometry. The light source used is Chameleon Ultra II (Coherent, Santa Clara, CA). The excitation laser beam is expanded and illuminates the 8 × 8 or 4 × 4 DOE (customized, Holo/Or, Rehovoth, Israel) depending on the excitation wavelengths (8 × 8 for 780 nm and 4 × 4 for 910 nm). The beamlets are shrunk according to the size of x-y galvanometric mirror scanners (6215H, Cambridge Technology, Lexington, MA), and overlapped on the scanning mirrors. The beamlets reflected by the scanners are expanded again to fill the back focal plane of a 20 × water immersion objective lens with 1.0 NA (W Plan-Apochromat, Zeiss, Thornwood, NY), and enter the aperture with different entrance angles. The objective lens generates an array of 8 × 8 excitation foci on the focal plane in a specimen. The image is formed by raster scanning of the excitation foci across the specimen using the scanning mirrors. The excitation foci are separated each other by 85 μm, and each focus scans slightly larger than the area of 85 μm × 85 μm in the sample plane for montage. The whole scanning size covered by the 8 × 8 foci is 680 μm × 680 μm with the 85 μm separation. The emission photons are collected by the same objective lens and descanned by the scanning mirrors. The descanned emission beamlets become stationary regardless of the scanning. The emission beamlets are reflected by a dichroic mirror (Chroma Technology, Bellows Falls, VT) toward the MAPMT and are focused onto the center of each corresponding anode of the MAPMT (H7546B-20, Hamamatsu, Bridgewater, NJ). An IR blocking filter (BG39, Chroma Technology, Bellows Falls, VT) and a short-pass filter (ET680sp-2p, Chroma Technology, Bellows Falls, VT) is installed before the MAPMT to block the excitation light. The other MMM system with 45 μm foci separation has very similar system configuration, but it uses a different model's Ti-Sapphire (Ti-Sa) laser (Tsunami, Spectra-Physics, Mountain View, CA) pumped by a continuous wave Nd:YVO_4 laser (Millennia, Spectra-Physics,

Mountain View, CA) as a light source, the 8 × 8 micro-lenses of a square lenslet array (1000-17-S-A, Adaptive Optics, Cambridge, MA), and a 0.95 NA objective lens (XLUMPLFL20XW, Olympus, Melville, NY). The 45 μm foci separation in a specimen provides total 360 μm × 360 μm imaging size.

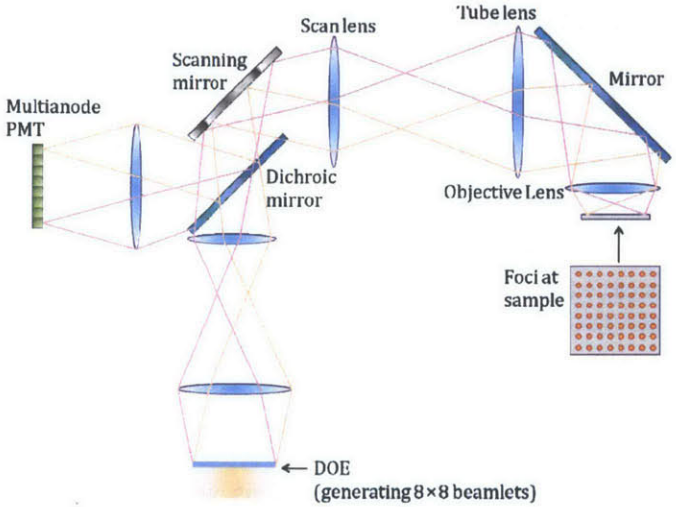

Fig 3.2. Schematic of MMM based on the MAPMT.

3.2.2. Image reconstruction methodology

Let $O(x,y,z)$ be the fluorophores distribution in the specimen assuming constant irradiance per unit volume with the specimen. For two-photon point excitation at scan position $\vec{x}'$, the excitation intensity distribution at the specimen projected by an objective with a normalized 3D intensity PSF $h(\vec{x})$ is $E(\vec{x},\vec{x}') = E_o\delta(\vec{x}-\vec{x}') \otimes h(\vec{x}) = E_o h(\vec{x}-\vec{x}')$. Here E_0 is the maximum intensity and the symbol, $\otimes$, represents the 3D convolution operator . The fluorescence intensity generated at the specimen due to two-photon process is:

$$F(\vec{x},\vec{x}') = E_0^2 h^2(\vec{x}-\vec{x}') \cdot O(\vec{x}) \qquad (1)$$

The effect of emission photon scattering can be modeled by a more general form of the emission PSF $h_m(\vec{x})$, assuming $h_m(\vec{x}) = h(\vec{x})$ in the absence of scattering and $h'(\vec{x})$ represents the PSF for the scattered emission photon.

$$h_m(\vec{x}) = (1-\alpha)h(\vec{x}) + \alpha h'(\vec{x}) \qquad (2)$$

Without emission scattering effect, α is zero. In general [25], even in the presence of scattering, the amplitude of the modification term is generally small, i.e., $\alpha < 1$. Also, it has been observed that $h'(\vec{x})$ typically has full-width-at-half maximum that is orders of magnitude larger than that of $h(\vec{x})$ [25].

The intensity distribution at the image plane in epi-detection geometry is:

$$I(x,y,\vec{x}') = [E_0^2 h^2(\vec{x}-\vec{x}')\cdot O(\vec{x})] \otimes h_m(\vec{x})\big|_{z=0} \tag{3}$$

For the MMM system, let $N \times N$ equally spaced foci be arranged on a rectilinear grid with reference positions $\{\vec{x}_{1,1}^0,.....\vec{x}_{N,N}^0\}$, where $\vec{x}_{m,n}^0 = \{m\Delta, n\Delta, 0)$, m and n are the foci indices, and Δ is the separation distance between foci. In order to generate an image using MMM, this grid of foci must be scanned to cover each $\Delta \times \Delta$ sub-regions for the corresponding axial plane. The signal for an MMM system at location (x, y) of an imaging sensor (CCD or CMOS) at any scan location (i, j, k) can be written as,

$$I_{MMM}(x,y,i,j,k) = \sum_{m,n}^{N,N} I(x,y,\vec{x}_{m,n}^0 + \vec{x}'_{i,j}, \vec{x}'_k) = \sum_{m,n}^{N,N} \{[E_0^2 h^2(\vec{x}-\vec{x}_{m,n}^0 - \vec{x}'_{i,j})\cdot O(\vec{x}+\vec{x}'_k)] \otimes h_m(\vec{x},k)\}\big|_{z=0} \tag{4}$$

For a given z-plane, k, using an imager (such as a CCD or CMOS camera with sensor size M x M) that integrates the signal for all the lateral scan steps, the final single plane image can be written as:

$$I_{MMM}(x,y,k) = \sum_{i,j}^{M,M} I_{MMM}(x,y,i,j,k) = \sum_{i,j}^{M,M} \sum_{m,n}^{N,N} \{[E_0^2 h^2(\vec{x}-\vec{x}_{m,n}^0 - \vec{x}'_{i,j})\cdot O(\vec{x}+\vec{x}'_k)] \otimes h_m(\vec{x},k)\}\big|_{z=0} \tag{5}$$

It is clear that in this case, the final image is "blurred" by the emission PSF and SNR is degraded. Instead of using an imager such as a CCD, we can also use a multianode PMT. By doing so there are two main differences [25]; (i) The image is descanned in the multianode PMT to ensure that the foci are center at each anode of the PMT, and (ii) The signal at each anode is integrated at each scanning step.

$$I_{MD}(x,y,i,j,k)=\sum_{m,n}^{N,N}\{[E_0^2h^2(\vec{x}-\vec{x}_{m,n}^0-\vec{x}_{i,j}')\cdot O(\vec{x}+\vec{x}'_k)]\otimes h_m(\vec{x},k)\}\Big|_{z=0,x=x+i\Delta/M,y=y+j\Delta/M}$$

$$=\sum_{m,n}^{N,N}\int dx''dy''dz''E_0^2h^2(x''-m\Delta-i\Delta/m,y''-n\Delta-j\Delta/M,z'')$$

$$\cdot O(x'',y'',z''+k\Delta')h_m(x-x'',y-y'',z-z'',k)\Big|_{z=0,x=x+i\Delta/M,y=y+j\Delta/M}$$

$$=\sum_{m,n}^{N,N}\int dx''dy''dz''E_0^2h^2(x''-m\Delta-i\Delta/M,y''-n\Delta-j\Delta/M,z'')$$

$$\cdot O(x'',y'',z''+k\Delta')h_m(x+i\Delta/M-x'',y+j\Delta/M-y'',-z'',k) \tag{6}$$

Therefore, within these limited domains, since $h'(\vec{x})$ is broad and smooth on the length scale of Δ, the integrand of the integral may be replaced by a set of constant values $C_{(a,b),(m,n),k}$ that are related to the radially integrated PSF (H_0) of the scattered light. Here (a,b) are the anode index and (m,n) are the foci index. The C matrix is depth dependent, specified by k for the given z-plane. Considering that the emission PSF can be further separated into a part taking into account of scattering, Eqn. (6) can now be rewritten as,

$$I_{MD}(a,b,i,j,k)=(1-\alpha(k))E_0^2H_0\int dx''dy''dz'h^2(x'',y'',z')\cdot O(x''+a\Delta+i\Delta/M,y''+b\Delta+j\Delta/M,z'+k\Delta')$$

$$+\alpha(k)E_0^2\sum_{m,n}^{N,N}C_{(a,b),(m,n),k}\int dx''dy''dz'h^2(x'',y'',z')\cdot O(x''+m\Delta+i\Delta/M,y''+n\Delta+j\Delta/M,z'+k\Delta') \tag{7}$$

Then equation (7) can be further simplified as:

$$I_{MD}(a,b,i,j,k)=(1-\alpha(k))H_0I(a,b,i,j,k)+\alpha(k)\sum_{m,n}^{N,N}C_{(a,b),(m,n),k}I(m,n,i,j,k) \tag{8}$$

The detection process consists of measured photon count by each anode (a,b) at each scan location (i, j, k), i.e. $N(a,b,i,j,k)$. $N(a,b,i,j,k)$ should follow Poisson statistics with a mean given by $I_{MD}(a,b,i,j,k)$.

2.2.1 Maximum Likelihood Estimation

The log-likelihood function of this readout process, described in eqn. (8), can be written as.

$$l_S = \sum_{a,b,i,j,k} [N(a,b,i,j,k) \ln I_{MD}(a,b,i,j,k) - I_{MD}(a,b,i,j,k)] \tag{9}$$

The log-likelihood function utilizes the physical modeling of the MMM for the maximum likelihood estimation of specimen fluorophores distribution. Our approach provides maximization of log-likelihood function, thus provides the quantification of scattering matrix that is used for the reassignment for the image photons to the correct spatial location, which are originally recorded as ghost image photons by the neighboring anodes of MAPMT. Therefore, photon reassignment can be casted as a blind deconvolution problem that seek to recover the image $I_{MD}(a,b,i,j,k)$ and the mixing kernel, $C_{(a,b),(m,n),k}$ given $N(a,b,i,j,k,\alpha)$ for a emission scattering condition.

The original fluorophores distribution at the corresponding axial depth recorded by the MMM system can be considered as the 'first guess' for the iteration process and the maximization of log-likelihood function can be performed using numerical optimization method which iteratively improves the strength of the actual signal by reassignment of ghost-image photons to correct spatial location. We adopted Newton's method for maximizing the log-likelihood function and the iteration step for maximum likelihood estimation of fluorophores distribution can be written as:

(i) Maximize the likelihood function with respect to $I(a,b,i,j,k)$ to get a better estimation for this variable:

$$\hat{I}^{(k+1)}(a,b,i,j,k)=\hat{I}^{(k)}(a,b,i,j,k)-\frac{\left\{\dfrac{\partial l_s(I,H_0,C,\alpha,k)}{\partial I(a,b,i,j,k)}\right\}_{I(a,b,i,j,k)=\hat{I}^{(k)}(a,b,i,j,k)}}{\left\{\dfrac{\partial^2 l_s(I,H_0,C,\alpha,k)}{\partial I^2(a,b,i,j,k)}\right\}_{I(a,b,i,j,k)=\hat{I}^{(k)}(a,b,i,j,k)}} \tag{10}$$

(ii) Maximization of Likelihood function with respect to C to get a better estimation for this variable:

$$\hat{C}^{(k+1)}_{(a,b),(m,n),k}=\hat{C}^{(k)}_{(a,b),(m,n),k}-\frac{\left\{\dfrac{\partial l_s(I,H_0,C,\alpha,k)}{\partial C_{(a,b),(m,n),k}}\right\}_{C_{(a,b),(m,n),k}=\hat{C}^{(k)}_{(a,b),(m,n),k}}}{\left\{\dfrac{\partial^2 l_s(I,H_0,C,\alpha,k)}{\partial C^2_{(a,b),(m,n),k}}\right\}_{C_{(a,b),(m,n),k}=\hat{C}^{(k)}_{(a,b),(m,n),k}}} \tag{11}$$

(iii) Maximization of Likelihood function with respect to α to get a better estimation for this variable:

$$\hat{\alpha}^{(k+1)}=\hat{\alpha}^{(k)}-\frac{\left\{\dfrac{\partial l_s(I,H_0,C,\alpha,k)}{\partial \alpha}\right\}_{\alpha=\hat{\alpha}^{(k)}}}{\left\{\dfrac{\partial^2 l_s(I,H_0,C,\alpha,k)}{\partial \alpha^2}\right\}_{\alpha=\hat{\alpha}^{(k)}}} \tag{12}$$

Here $\hat{I}^{(k)}$, $\hat{C}^{(k)}$, and $\hat{\alpha}^{(k)}$ are the estimated fluorophores distribution, scattering matrix coefficients, emission scattering coefficient respectively at k^{th} iteration step. The maximization process updates the new estimate of $\hat{I}^{(k+1)}$, $\hat{C}^{(k+1)}$, and $\hat{\alpha}^{(k+1)}$ for iterative step k. The log-likelihood function is evaluated at each iteration step for maximum likelihood estimation of fluorophores distribution. The accuracy of this estimation partly depends on the initial estimates chosen and on the constrained parameters, i.e., positivity of the fluorophores. Fig 3.3 provides the summary of the proposed photon reassignment algorithm for MMM system.

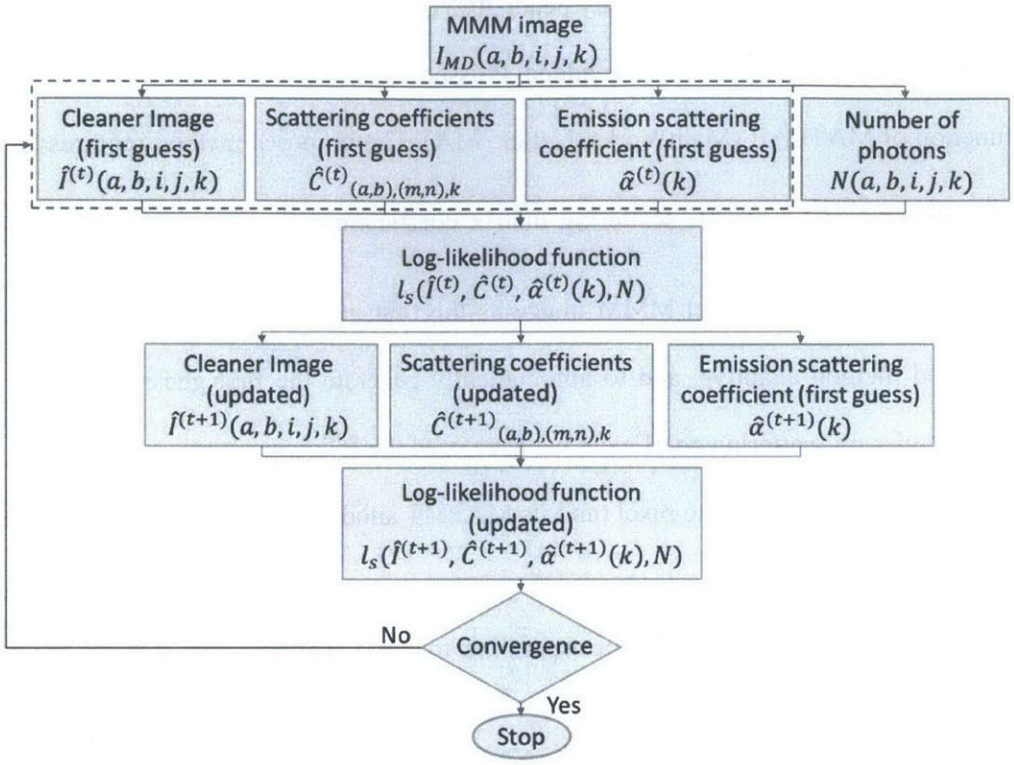

Fig 3.3. Summary of the photon reassignment process for MMM

3.3. RESULTS

3.3.1. Simulation results

3.3.1.1. 4 Spots in a 2 by 2 MMM image

To see the feasibility of our approach, we started from the simplest case using simulations. We simulated a replica of 4 beads image in a 2 by 2 MMM [Fig 3.4 (a)-(b)]. First, Fig 3.4 (a) showed the original image of 4 beads without ghost images, which would be the target of our simulation result. Then, for the MMM image, one sub-image contained one primary bead image with three ghost bead images, and there was no overlap between the beads for simplicity, as shown in Fig 3.4 (b). Any scattering-simulated sub-image

contained 100% of the intensity of the primary bead, 20% of the intensity of the adjoining beads, and 14% of the intensity of the diagonal bead. We added Poisson noise in the simulated image by using the '*imnoise*' function of MATLAB (MathWorks, Natick, MA). The proposed method requires the first guess of the cleaner image $\hat{I}^{(1)}(a,b,i,j,k)$, scattering matrix coefficients $\hat{C}^{(1)}_{(a,b),(m,n),k}$, and emission scattering coefficient $\hat{\alpha}^{(1)}$. We chose the actual MMM image as the first guess for the cleaner image. In order to keep the proposed method adaptive, and to automatically generate the first guess for scattering matrix coefficients and emission scattering coefficient we have used the following steps:

(i) Identify the spatial position of the pixel (and its MAPMT anode) that contains the maximum intensity in the entire MMM image.

(ii) Observe the intensities at the pixels corresponding to same spatial location of all the neighboring anodes identified in step (i).

(iii) Generate the intensity ratios of the maximum value pixel to neighboring anode pixels.

(iv) Repeat the steps (i)-(iii) for a few more values next to the maximum intensity, if possible, and take the mean of the all these values.

(v) More coefficients of the scattering matrix for the other anodes are calculated in the same manner described in the previous steps. All these calculated coefficients are used for the first guess of the scattering matrix. In order to conserve the photon count, the sum of each row of scattering matrix (representing one anode under observation and its contribution in all other anodes of MAPMT) is normalized to 1.

(vi) The mean value observed in step (iv) is also considered as the first guess of emission scattering coefficient i.e. $\hat{\alpha}^{(1)}$.

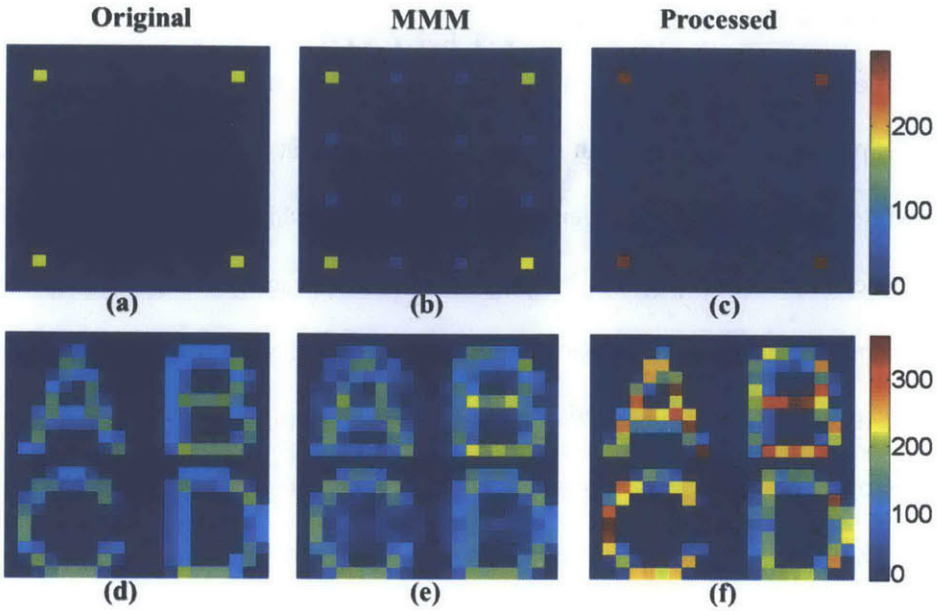

Fig 3.4. (a) Original 4 beads image in a 2 by 2 MMM. (b) A scattering-affected image of (a); one sub-image contains one primary bead image and three ghost bead images with the specified proportions. (c) The processed image of (b). (d) Original alphabet image in a 2 by 2 MMM. (e) A scattering-affected image of (d) in the same fashion. (f) The processed image of (e).

We process the simulated MMM image by initializing of the parameters as discussed above. The iteration process, as shown in Fig 3.3, started to maximize the log-likelihood function and this also performed reassigning the scattered emission photons of the ghost images to the original spatial locations. During iterative process we defined two constraints; first total number of photons of the MMM images is constant before and after the processing, and second the positivity of the pixel values (as the fluorescence signal cannot be negative). The reconstruction process took around 10 iterations and Fig 3.4 (c) shows the processed image. It can be visually observed that all the ghost images are completely suppressed in the final reconstructed image. It can be clearly observed that the intensity of processed beads image is increased, and this represents the increase in the photon count of the beads location came from the ghost image locations. More quantified results for the improvement of the signal strength and signal-to-ghost image ratio (SGR) will be presented later in this paper.

3.3.1.2. Alphabets in a 2 by 2 MMM image

As a next simulation, an alphabet image was examined with our method. Compared to the simulated beads image, the alphabet image has certain shapes and overlaps that provide more complexity. Again, an original image without ghost images was generated [Fig 3.4 (d)], which would be our target. Then, ghost images were imposed on all sub-images in the way that one sub-image in a 2 by 2 MMM image contains one primary alphabet image with the ghost images of the other three alphabets [Fig 3.4 (e)]. The one scattering-affected sub-image contains 100% of the intensity from a primary sub-image, 20% of the intensity from the other neighbor sub-images, and 14% of the intensity of the diagonal image. The final processed image, shown in Fig 3.4 (f) showed cleaner reconstruction of alphabets similar to the original. Clearly, the effects of ghost images are significantly suppressed from the MMM images by using the proposed approach. To start the iteration process the first guess of the scattering matrix and scattering coefficient was calculated same as for the simulated bead image. Again, as discussed before, the image intensity of the processed image is higher than the original simulated image because of the reassignment of the ghost image photons to the original spatial locations from where they are generated due to emission scattering.

Quantitative analysis of the reconstruction results is performed to analyze the performance of the proposed method. Fig 3.5 (a) shows the intensity comparison of the MMM and processed image of simulated beads. The sum of the intensity of the simulated bead and its ghost images, in MMM image, is compared with the intensity of the same bead of the processed image. The error bar, in the MMM, are showing the range of Poisson noise, added in the simulated MMM image used for processing using the proposed method. Clearly, reconstruction intensities at different anode locations are within the Poisson noise range showing the accuracy of the photon reassignment process from ghost images to correct spatial locations. Next, comparison of elements of the scattering matrix corresponding to different anodes is performed. The scattering matrix elements for (1,1) anode should be [0.61 0.14 0.14 0.1] based on the preset parameters and the acquired emission scattering coefficient with normalization, and the same ratio

follows for other anodes depending on their spatial locations. Our target is to compare the recovered scattering matrix elements, based on the proposed approach, with the original one used for simulation. Fig 3.5 (b) shows the original scattering matrix elements used for simulation for both beads and alphabets images. Fig 3.5 (c) and (d) show the reconstructed scattering matrix elements for the beads images and alphabets images respectively.

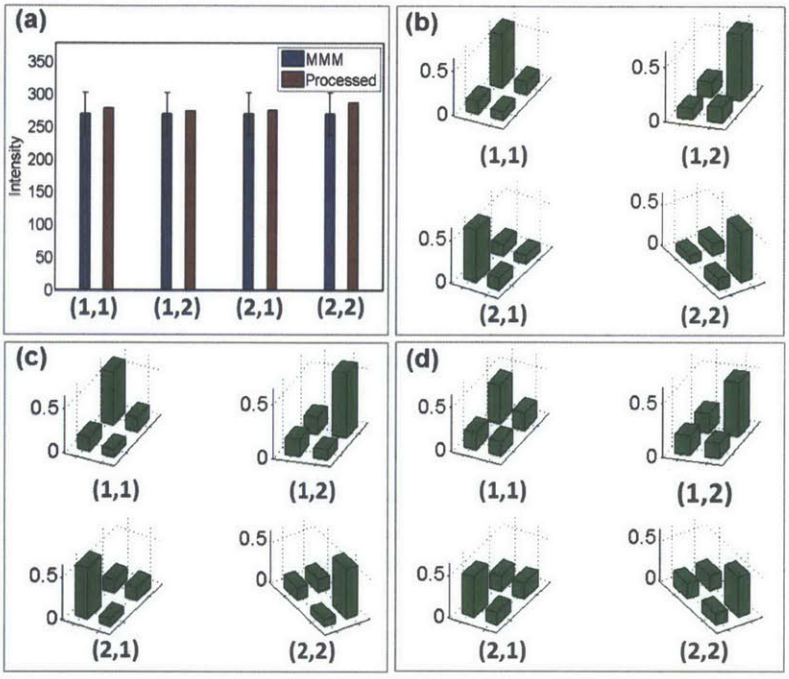

Fig 3.5. (a) Intensity comparison of the primary beads in the simulated MMM image (blue, main anode + ghosts, subjected to Poisson noise) and their processed images (red). (b-d) Scattering coefficients distribution at 2by2 MMM anodes. (b) Original distribution used in simulation, (c) estimated distribution of the processed bead image, and (d) the alphabet image. One sub-image contains a primary coefficient from the corresponding image and three scattering coefficients showing the leakage of emission photons to the neighbor anodes due to scattering.

3.3.2. Experimental results

3.3.2.1 Fluorescent beads image in 6 by 6 MMM with 85 μm foci separation

We tested our proposed approach with fluorescent beads image taken from 6 by 6 MMM system (with foci separation 85 μm) as described in Sec. 2.1. The sample was prepared with 10 and 15 μm diameter fluorescent latex microspheres (F8836 and F21010, Molecular Probes, Eugene, OR) immobilized in 3D by 2 % agarose gel. Fat emulsion (Microlipid, Nestle, Vevey, Switzerland) was added as a scatterer in 2 % concentration to mimic the scattering characteristic of a tissue specimen.

The left column of Fig 3.6 shows the acquired fluorescent beads MMM images at four different depths (0 μm, 40 μm, 85 μm, and 135 μm). As expected, the scattering effect increases with increase in imaging depth and thus the effect of ghost images are more prominent for the larger imaging depth. To suppress the effect of the ghost images and to reassign the photons of the ghost images to their original spatial locations, we used our proposed method. For the 6 by 6 MMM image, total $36 \times 36 = 1296$ coefficients are necessary for the scattering matrix C. Apparently, it is required to separately estimate the first guess of the scattering matrix and scattering coefficient for each depth as the effect of scattering is different. To start the photon reassignment iteration process, we have used the same criteria as explain in section 3.1.1 to evaluate the first guess of the scattering matrix and scattering coefficient. The iteration process took around 30 iterations and the right column of Fig 3.6 shows the processed images at their corresponding depths. Clearly, most of the strong ghost images were removed successfully, and only the primary bead images were left, with better signal strength. In order to understand the performance of the proposed method on the signal levels of the imaging bead and its effect on the ghost image, we analyzed some of the relevant imaging parameters of the original and the processed MMM image. Fig 3.7 (a) shows the strength of the signal of the bead at its original spatial location before and after processing. Clearly, the strength of the signal is higher for the processed images, particularly at the larger imaging depth. It is due to the fact that the processing provides the reassignment of the photons from the ghost image locations to the original beads location and thus increases the strength of the signal. This improvement in the signal is expected to be higher for the larger imaging depth as the ghost images are strong corresponding to the higher scattering effect. Fig 3.7 (b) shows the effect of the photon reassignment by calculating the ratio of

the signal at original bead location to the signal detected at its strongest ghost image location, called signal-to-ghost ratio (SGR). We calculated SGR for original and the processed images at each imaging depth. Evidently, the SGR is supposed to be the highest for the smallest imaging depth because of the least scattering effect. The SGR of the original image, which is significantly lower for the large imaging depth because of severe scattering, is substantially recovered for the processed image.

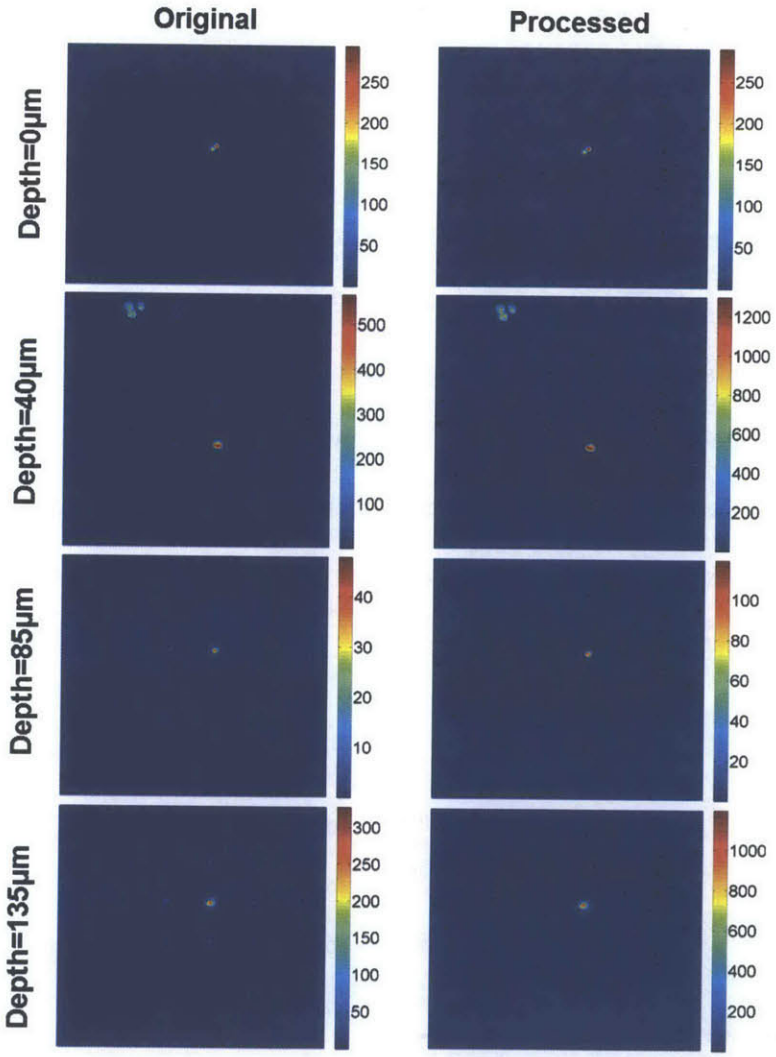

Fig 3.6. Left column: fluorescent beads images with the 6 by 6 MMM system at three imaging depth. Right column: Corresponding processed images

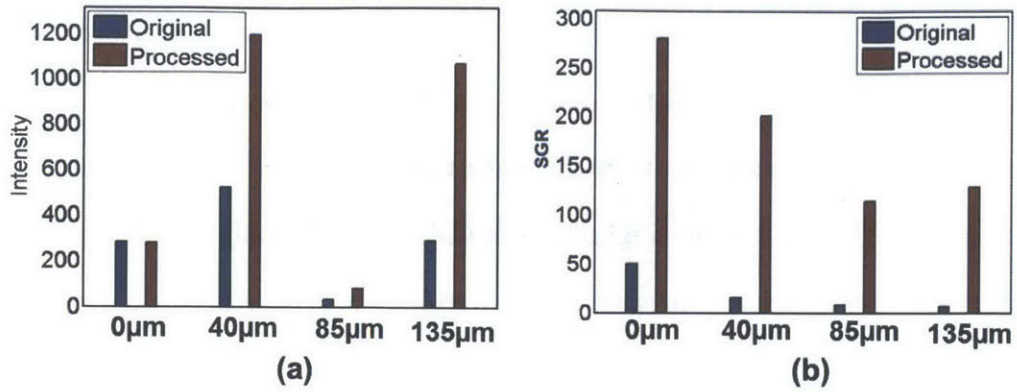

Fig 3.7. (a) Bead's signal comparison at different depths for original and processed image. (b) Signal-to-Ghost ratio (SGR) of the imaging beads at different depths.

Elements of scattering matrix at the image bead location anode and adjacent nearest neighbors are analyzed for different imaging depth, as shown in Fig 3.8 (a). As the imaging depth increases, due to increase in the emission scattering the scattering matrix elements become flatter and the ratio of main anode to neighboring anodes decreases as previously investigated in the Ref [25]. This effect is further elaborated by plotting the values of scattering coefficient acquired at the different imaging depths, as shown in Fig 3.8 (b). As the imaging depth increases, the scattering coefficient expectedly increases showing the increased scattering effect.

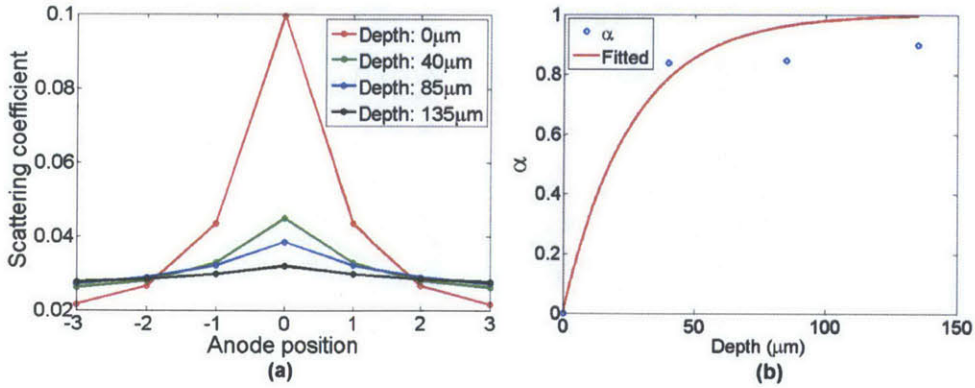

Fig 3.8. (a) Plot of scattering coefficient for an anode and its distribution at neighboring anodes corresponding to different imaging depths of fluorescence beads image, (b) Plot of emission scattering coefficient as function of depth.

3.3.2.2. Mouse brain imaging in 4 by 4 MMM with 85 μm foci separation

We tested our approach with mouse brain image taken in the 4 by 4 MMM system. Thy1-GFP transgenic mice [26] had surgery for cranial windows that were bilaterally implanted over the visual cortices between 6-8 weeks of age. These mice express green fluorescent protein (GFP) in a sparse pseudo-random subset of neocortical neurons. Imaging was performed on adult mice (>3 months) previously implanted with cranial windows. Mice were anesthetized with isoflurane (3% for induction and 1.5% during imaging). Anesthesia was monitored by breathing rate and foot pinch reflex. The head was positioned in a custom made stereotaxic restraint affixed to a stage. Cell body and dendritic arbors of inhibitory neurons labeled with GFP in layers 2/3 of visual cortex were imaged. The excitation wavelength was 910 nm, , the laser power per focus was about 42 mW, the dwell time was 40 μs with 0.5 μm pixel, and the image size was 340 μm × 340 μm with 4 × 4 foci..

The left column of Fig 3.9 shows the MMM images of the mouse brain at 100 μm and 190 μm imaging depths. Ghost images can be visually observed in at both depths, particularly they are more prominent for the larger imaging depth. The proposed approach was used to suppress the effect of the ghost images and to reassign the photons of the ghost images to their original spatial locations. For the 4 by 4 MMM image, total $16 \times 16 = 256$ coefficients are necessary for the scattering matrix C. We have used the same criteria as explained before to evaluate the first guess of the scattering matrix and scattering coefficient. Processed images are shown in Fig 3.9, the right column at the corresponding depths. Most of the strong ghost images were clearly removed. With the expectation of the similar behavior of imaging parameters as shown in Fig 3.7, we also analyzed the behavior of elements of scattering matrix and scattering coefficient at different depth and Fig 3.10 show the plot of their values as a function of depth. Similar to the result of the bead sample in section 3.2.1, the scattering matrix becomes flatter and the scattering coefficient increases as the imaging depth increases.

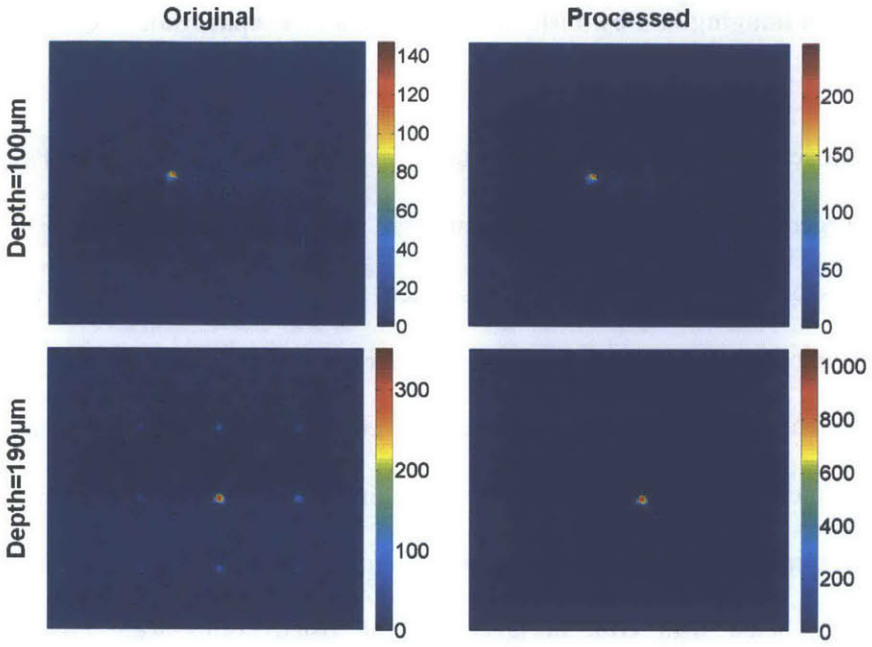

Fig 3.9. A mouse brain image with the 4 by 4 MMM system. Left acquired images at 100 μm and 190 μm imaging depths, and Right are the corresponding processed images.

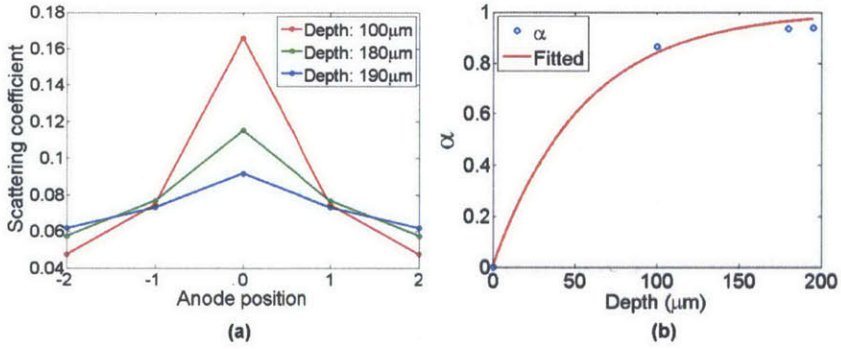

Fig 3.10. (a) Plot of scattering coefficient for an anode and its distribution at neighboring anodes corresponding to different imaging depths of mouse brain, (b) Plot of emission scattering coefficient as function of depth.

3.3.2.3 Fluorescent beads and Mouse brain imaging in MMM with 45 μm foci separation

We further tested our proposed approach with a fluorescent beads and Mouse brain image taken from MMM system with foci separation 45 μm. The reduced separation of the foci, for the same scattering conditions, will increase the crosstalk between the foci and it results as the strong ghost images. The beads sample was prepared with 4 μm diameter fluorescent latex microspheres (F8858, Molecular Probes, Eugene, OR) immobilized in 3D by 2 % agarose gel. Intralipid emulsion (Liposyn III, Abbott Laboratories, North Chicago, IL) was added as a scatterer in 2 % concentration to mimic the scattering characteristic of a tissue specimen. For the mouse brain imaging, a Thy1-GFP transgenic mouse [26] was deeply anesthetized with 2.5% Avertin (0.025 ml/g i.p.) and transcardially perfused with PBS, followed by 4% paraformaldehyde. Its brain was dissected and placed overnight in cold 4% paraformaldehyde. 300 μm thick coronal sections were sectioned with a vibrotome, then mounted and coverslipped on microscope slides using adhesive silicone isolators (JTR20-A2-1.0, Grace Bio-Labs, Bend, OR).

Fig 3.11 (a) shows the fluorescence beads image taken from the 6 by 6 MMM with foci separation of 45 μm at 150 μm imaging depth and (b) is its corresponding processed image. Clearly, due to the smaller foci separation the scattered emission photons were scattered into the adjacent neighboring anodes of the MAPMT and resulting in the formation of ghost images. We used our proposed approach to suppress the ghost images in such a severe scattering case. From the processed image shown in Fig 3.11 (b), we can visually observe that the ghost images are significantly suppressed, and the remaining dim beads are some signals from the beads situated at neighboring axial planes. However, even with the same scattering in sample but because of different foci separation, the scattering coefficients were 0.88 for 85μm at 135μm imaging depth, and 0.98 for 45μm imaging 150μm depth. Finally, Fig 3.11 (c) shows the mouse brain imaging taken at 90 μm imaging depth using the 8 by 8 MMM system with foci separation 45 μm, and Fig 3.11 (d) is its corresponding processed image. The same criteria, as discussed before, were used to estimate the first guess of the scattering matrix and scattering coefficient.

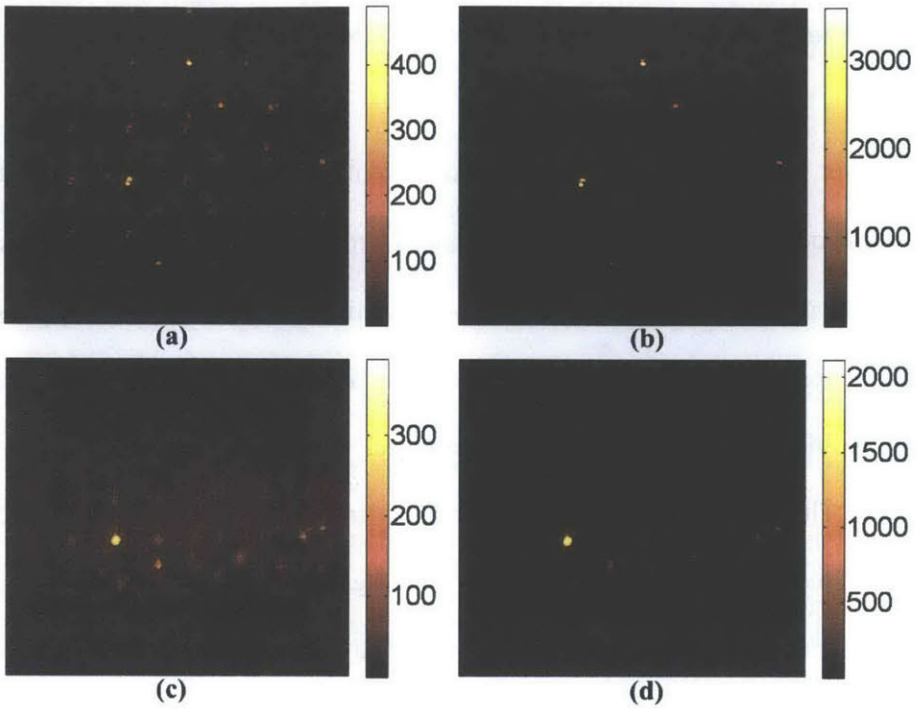

Fig 3.11. MMM images (with foci separation 45μm) and its processing. (a) Fluorescent beads image with the 6 by 6 MMM system, and (b) is the corresponding processed image. (c) Image of GFP expression neurons in mouse brain acquired using 8 by 8 MMM system at 90μm depth, and (b) is the corresponding processed image.

3.4. CONCLUSIONS

MMM has an advantage of imaging speed improvement realizing high throughput *in vivo* imaging. However, MMM images suffer from ghost images due to scattering of a turbid specimen especially when the imaging depth is large. The ghost images have been processed by acquiring the scattering coefficients experimentally. However, the experimental estimation requires frequent measurement with different specimen and even with different locations and imaging depths. In this paper, we have proposed to estimate the scattering coefficients with the photon reassignment process established based on the maximum likelihood (ML) estimation. This image post-processing method increases the SNR and SBR of the final processed image by reassigning the scattered photons to the original spatial locations, and also avoids experimental measurements resulting in saving time and minimizing possible errors. We have

shown the feasibility of our approach with simulated results and confirmed that the algorithm can estimate the scattering coefficients and reassign the ghost images. Further we examined it with fluorescent bead samples in the turbid medium, and *in vivo* mouse brain images. The processed images showed that the scattered emission photons were reassigned to their original spatial locations resulting in higher signal at the original location. The SGR was improved by up to a factor of 10. The algorithm also confirmed that the shorter foci separation generated more crosstalk, and the scattering coefficient has increased as a function of imaging depth. To minimize the crosstalk between foci and the resulting ghost images inherently, it is recommended to adopt a large field of view objective lens and maximize the foci separation. However, in the case that only small field of view objective lenses are available or a region of interest is small, our proposed approach will be a good solution for image post processing and image recovery. Fig 3.12 shows the plot of log-likelihood function versus number of iterations for the processing of mouse brain imaging as shown in Fig 3.9. Convergence of the log-likelihood function starts at around 15 iterations, which provides the final processed image. The total computational time taken for processing two imaging planes was 40 seconds by using the normal desktop computer with i5 processor.

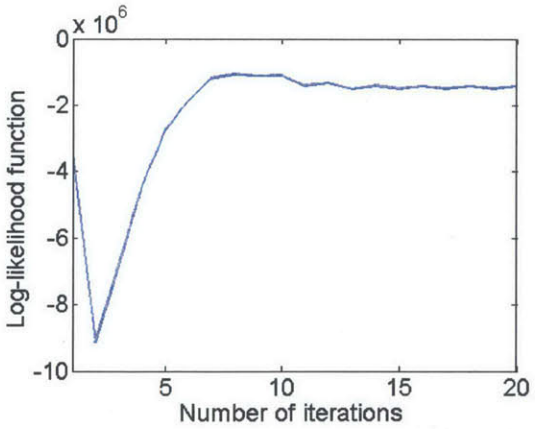

Fig 3.12. Plot of log-likelihood function for number of iterations.

References

1. Denk, W., J.H. Strickler, and W.W. Webb, *2-PHOTON LASER SCANNING FLUORESCENCE MICROSCOPY.* Science, 1990. **248**(4951): p. 73-76.

2. So, P.T.C., et al., *Two-photon excitation fluorescence microscopy.* Annual Review of Biomedical Engineering, 2000. **2**: p. 399-429.
3. Svoboda, K., et al., *In vivo dendritic calcium dynamics in neocortical pyramidal neurons.* Nature, 1997. **385**(6612): p. 161-165.
4. Lee, W.C.A., et al., *A dynamic zone defines interneuron remodeling in the adult neocortex.* Proceedings of the National Academy of Sciences, 2008. **105**(50): p. 19968-19973.
5. Ragan, T., et al., *Two-photon tissue cytometry.* Methods in cell biology, 2004. **75**: p. 23-39.
6. Kim, K.H., et al., *Three-dimensional tissue cytometer based on high-speed multiphoton microscopy.* Cytometry Part A, 2007. **71**(12): p. 991-1002.
7. Kim, K.H., C. Buehler, and P.T.C. So, *High-speed, two-photon scanning microscope.* Applied optics, 1999. **38**(28): p. 6004-6009.
8. Fan, G., et al., *Video-rate scanning two-photon excitation fluorescence microscopy and ratio imaging with cameleons.* Biophysical journal, 1999. **76**(5): p. 2412-2420.
9. Iyer, V., B.E. Losavio, and P. Saggau, *Compensation of spatial and temporal dispersion for acousto-optic multiphoton laser-scanning microscopy.* Journal of Biomedical Optics, 2003. **8**: p. 460.
10. Reddy, G.D. and P. Saggau, *Fast three-dimensional laser scanning scheme using acousto-optic deflectors.* Journal of Biomedical Optics, 2005. **10**: p. 064038.
11. Zeng, S., et al., *Simultaneous compensation for spatial and temporal dispersion of acousto-optical deflectors for two-dimensional scanning with a single prism.* Optics Letters, 2006. **31**(8): p. 1091-1093.
12. Katona, G., et al., *Fast two-photon in vivo imaging with three-dimensional random-access scanning in large tissue volumes.* Nature methods, 2012. **9**(2): p. 201-208.
13. Cianci, G.C., J. Wu, and K.M. Berland, *Saturation modified point spread functions in two-photon microscopy.* Microscopy research and technique, 2004. **64**(2): p. 135-141.
14. Zipfel, W.R., R.M. Williams, and W.W. Webb, *Nonlinear magic: multiphoton microscopy in the biosciences.* Nature biotechnology, 2003. **21**(11): p. 1369-1377.
15. Oron, D., E. Tal, and Y. Silberberg, *Scanningless depth-resolved microscopy.* Optics Express, 2005. **13**(5): p. 1468-1476.
16. Zhu, G., et al. *Simultaneous spatial and temporal focusing of femtosecond pulses*. 2005: Optical Society of America.
17. Bewersdorf, J., R. Pick, and S.W. Hell, *Multifocal multiphoton microscopy.* Optics Letters, 1998. **23**(9): p. 655-657.
18. Buist, A.H., et al., *Real time two-photon absorption microscopy using multi point excitation.* Journal of Microscopy-Oxford, 1998. **192**: p. 217-226.
19. Nielsen, T., et al., *High efficiency beam splitter for multifocal multiphoton microscopy.* Journal of microscopy, 2001. **201**(3): p. 368-376.
20. Kurtz, R., et al., *Application of multiline two-photon microscopy to functional in vivo imaging.* Journal of neuroscience methods, 2006. **151**(2): p. 276-286.
21. Jureller, J.E., H.Y. Kim, and N.F. Scherer, *Stochastic scanning multiphoton multifocal microscopy.* Optics Express, 2006. **14**(8): p. 3406-3414.
22. Amir, W., et al., *Simultaneous imaging of multiple focal planes using a two-photon scanning microscope.* Optics Letters, 2007. **32**(12): p. 1731-1733.
23. Sacconi, L., et al., *Multiphoton multifocal microscopy exploiting a diffractive optical element.* Optics Letters, 2003. **28**(20): p. 1918-1920.
24. Watson, B.O., V. Nikolenko, and R. Yuste, *Two-photon imaging with diffractive optical elements.* Frontiers in neural circuits, 2009. **3**.
25. Kim, K.H., et al., *Multifocal multiphoton microscopy based on multianode photomultiplier tubes.* Optics Express, 2007. **15**(18): p. 11658-11678.
26. Feng, G., et al., *Imaging neuronal subsets in transgenic mice expressing multiple spectral variants of GFP.* Neuron, 2000. **28**(1): p. 41-51.

Chapter 4

Non-descanned Multifocal Multiphoton Microscopy with Multianode Photomultiplier Tube

4.1. Introduction

Multiphoton excitation fluorescence microscopy has inherent 3D resolution due to the nonlinear dependence of excitation efficiency on the incident light flux distribution [1, 2]. Multiphoton excitation can be localized to a femtoliter region at the focal point of a high numerical aperture objective. This power microscope modality has become one of the common solutions for non-invasive, deep imaging in many turbid biological specimens. Improving multiphoton microscope imaging speed is important for many research areas including studies of fast intra- and inter-cellular signaling events involving voltage or calcium transients and studies involving animal models where motion artifacts and anesthetic use should be limited. Several methods have been developed to improve imaging speed beyond conventional point scanning approach based on galvanometric mirror scanners. One approach is based on the use higher speed scanners such as polygonal mirrors [3], resonant mirror scanners [4], or acousto-optical deflectors [5-8]. These high speed scanners can typically achieve frame rate up to about 1 kHz in tissues with a comparable imaging depth as conventional multiphoton microscopy. However, the higher speed scanning requires a correspondingly decreased pixel dwell time resulting in poorer signal-to-noise ratio (SNR). This tradeoff can be partially compensated by increasing the excitation laser power but laser power is ultimately limited by specimen photodamage and excitation saturation [9, 10]. Another approach is two-photon wide-field imaging based on temporal focusing [11, 12]. In this case, two-photon excitation is localized to a plane, instead of a point, by controlling the spectrally dispersing the light pulse away from

the focal plane. However, wide-field two-photon imaging is often limited by the lower axial resolution and the smaller field-of-view (FOV) due to the need for much higher peak power laser pulses. Another popular approach to improve imaging speed is multifocal multiphoton microscopy (MMM) [13, 14]. With a lenslet array or a diffractive optical element (DOE) [15, 16], multiple foci are generated and scanned simultaneously. Within the limit of available laser power, about 100 foci can be effectively generated with a standard Ti-Sapphire oscillator resulting in approximately two orders of magnitude improvement in imaging speed proportionally. For MMM system, simultaneous acquisition of data from many foci often require the use of an area detector, such as a CCD or a CMOS sensor [13, 14]. The spatial registration is achieved by telecentric mapping of the image plane into the image sensor plane. In the presence of a turbid specimen, the emission photons can be scattered resulting in image blurring. More important, as scattered emission photons are scattered away from the correct location, they contribute to an increased background and degrading image SNR. To overcome this limit of emission light scattering, MMM with a descanned detection configuration using a multianode photomultiplier tube (MAPMT) has been developed [17, 18]. As in most confocal microscopes, the descanned geometry guides the emission photons from each focus backward along the same optical path shared with the excitation beams. Since the motion of the scanning mirror is much slower than the speed of light, the emission light rays after the scanning mirror becomes stationary independent of scanner motion and can be separated from the excitation beams with a dichroic mirror. The unscattered ballistic emission photons generated by each focus are focused at the cathode which is corresponding to the center of each anode of the MAPMT. This approach is described as "descanned" detection. The scattered emission photons will not be focused at the center but many can still be collected effectively by the appropriate anode. Very intuitively, the larger area projected by each anode at the specimen plane will result in greater collection efficiency of these scattered emission photons. At the limit of infinitely large anode, the collection efficiency of scattered emission photons will be comparable to that of a point focusing multiphoton system. Since the infinitely large anode limit cannot be completely realized, if the sample is highly scattering and imaging depth is

large, the scattered emission photons will reach neighbor anodes resulting in ghost images in the neighbor sub-images. We have shown that a number of post-processing algorithms can be developed to reassign the scattered photons into the neighboring pixels and mostly eliminating these ghost images [17]. In any case, to minimize the deleterious effect of the scattering of emission photons it is best to image using a high numerical aperture (NA), low magnification objective so that the foci can be physically separated as far as possible over the FOV on the specimen plane. Today, the most advanced objectives for multiphoton imaging typically has NA on the order of 1.0 and FOV of about 1 mm. This large FOV presents significant challenge in microscope intermediate optics design. The edge foci are generated from rays that subtend large angles with the optical axis and are far from paraxial and significant aberration can result from the use of intermediate optics with low f-number. This challenge is compounded by the fact that the excitation ray beams must be first de-magnified to fit onto the millimeter size galvanometric scan mirrors, their small size and light weight are important for fast scanning. The excitation beams must be magnified again to backfill the several centimeter diameter back aperture of these large FOV objectives to ensure diffraction limited focusing. These beam size control requirements are difficult to satisfy with using commercially available high f-number lenses that have short focal distances that are not compatible with the placement with components in the optical path with substantial physical sizes such as the galvanometric scanning mirror system. The need for some low f-number lenses results in aberrated point spread function (PSF), especially at the edge and corner foci, resulting in resolution and signal strength degradation at the edge of the image. Another major problem of the descanned MMM design is the loss of the emission signal in the descanned detection configuration that not only has many more optical surfaces that resulting in attenuating both un-scattered and scattered emission photons. The much longer optical path further results in losing a majority of scattered emission photons that are often scattered at large angles relative to the optical axis. Signal attenuation in the descanned geometry can become quite severe [17]. This problem is, of course, well known in point scanning multiphoton microscope and the preferred method to overcome this limitation is using a non-descanned configuration [19, 20]. In this work, we

propose a novel non-descanned MMM with a MAPMT detector that preserve the SNR immunity to scattered emission photon scattering but allows scanning over millimeter scale FOV with minimal aberration and improve emission photon collection by up to four times.

4.2. Method

4.2.1. Non-descanned MMM with an imaging detector

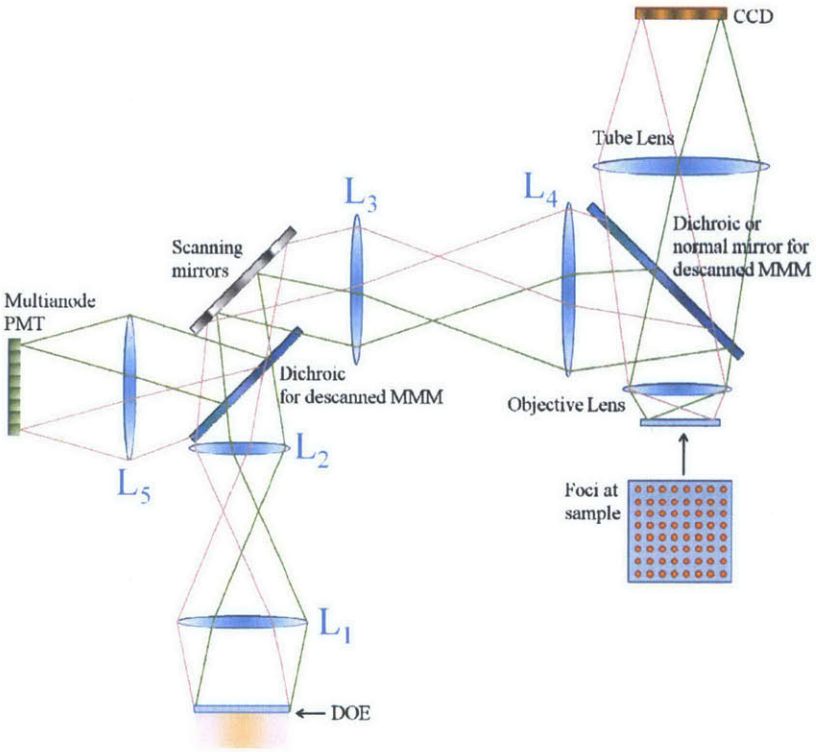

Fig 4.1. The schematic of older generations of MMM. Two generations of MMM are implemented here including a non-descanned MMM acquiring signal with a camera and a descanned version acquiring signal with a MAPMT.

Fig 4.1 shows the system configuration of a non-descanned MMM with an imaging detector similar to previous publications [13, 14]. The light source is a Chameleon Ultra II (Coherent, Santa Clara, CA). The excitation laser beam is split into a number of beamlets with a DOE (customized, 8 × 8 for 780 nm and 4 × 4 for 910 nm, Holo/Or, Rehovoth, Israel). The multiple beamlets are sent to x-y galvanometric mirror

scanners (6215H, Cambridge Technology, Lexington, MA), and scanned simultaneously. The scanned beamlets are expanded to overfill the back aperture of a 20× water immersion objective lens (W Plan-Apochromat, 1.0 NA, Zeiss, Thornwood, NY) with different entrance angles. The objective lens generates an array of excitation foci on the focal plane in a specimen. The emission photons are collected by the same objective lens. In the very early design of MMM the emission photons pass through the dichroic mirror after the objective lens according to the separation wavelength, and arrive at an imaging detector, such as a CCD camera. The camera acquires all the emission photons until scanning is done. As discussed, this configuration is very susceptible to SNR loss due to scattering of emission photons.

4.2.2. Descanned MMM with a MAPMT

Fig 4.1 also shows the descanned detection configuration with a MAPMT. For descanning, the dichroic mirror between the objective lens and lens L_4 is replaced by a normal mirror, and the dichroic mirror is located between the scanning mirrors and lens L_2. The emission photons from the sample travel backward through the optical path shared with the excitation beam. After the emission rays travel through the scanning mirrors they become stationary independent of scanner position; this process is called "de-scanning" and is well known in the design of confocal microscopes [21-24]. De-scanning is possible because the transit time of the excitation photon, the fluorescence lifetime, and the arrival time of the emission photons in combination is much faster than the motion of the scanner and the scanner is virtually motionless relative to the light. The symmetry of the light path between excitation and emission light rays ensures that the emission rays directions are constant independent of scanner motion. The stationary emission rays from the foci are reflected by the dichroic mirror (Chroma Technology, Bellows Falls, VT) and focused at cathode locations that correspond to the centers of each of the anodes of the MAPMT (H7546B-20, Hamamatsu, Bridgewater, NJ). An IR blocking filter (BG39, Chroma Technology, Bellows Falls, VT) and a short-pass filter (ET680sp-2p, Chroma Technology, Bellows Falls, VT) are installed before the MAPMT to block the excitation light. As long as the anode surface corresponds to a

sufficiently large area on the specimen plane, we can ensure that most of the scattered emission photons are collected in the designated channels. Therefore, the use of de-scanning and MAPMT detector can suppress the scattering effect of emission photon and resulting in higher SNR. However, as described above, there is significant loss of the emission signal due to having many optical surfaces and the long descanning path with limited size of optics (e.g. scanning mirrors). Important, significant aberration of edge foci is observed with using high NA, large FOV objectives.

4.2.3. Non-descanned MMM with MAPMT

The use of a high NA, large FOV objective allow excitation to be spaced far apart in the specimen plane minimizing crosstalk between the emission signals from neighboring foci. Unfortunately, the aberrations from the intermediate optics prohibit fully utilizing the FOV of the objective lens in the descanned configuration. In Fig 4.1, after the DOE, the size of the multiple excitation beamlets must be decreased with lens L_1 (f 300 mm, singlet, KPX232AR.16, Newport, Irvine, CA) and lens L_2 (f 75 mm, doublet, AC508-075-B-ML, Thorlabs, Newton, NJ) in a 4-f geometry to fit onto small, 5 mm size scanning mirrors (6215H, Cambridge Technology, Lexington, MA) to allow fast mechanical scanning. The lens L_3 (f 35 mm, doublet, AC254-035-B-ML, Thorlabs, Newton, NJ) and lens L_4 (f 175 mm, singlet, KPX196AR.16, Newport, Irvine, CA) in another 4-f configuration expand the beamlets to slightly overfill the 2 cm diameter back aperture of the objective lens ensuring diffraction limited focusing. Given the finite physical size of the scanning mirror assembly, lenses L_2 and L_3 must have sufficiently long focal lengths and relative poor (low) f-numbers, and generate large aberrations especially for edge and corner foci. Consequently, the final FOV becomes very limited (only around 300 μm × 300 μm from the available size of 700 μm × 700 μm). Large size scanning mirrors are available to avoid the aberrations from the reduction and the expansion processes, but scanning with them is slow. In addition, the use of larger mirror will also result in larger physical separation between the x-axis scanning mirror and y-axis scanning mirror resulting in greater non-uniformity of excitation over the FOV [25].

Fig 4.2 shows the schematic of the non-descanned MMM with MAPMT. The scanning mirrors are positioned before the DOE. In this configuration the excitation beam can be expanded gradually with two 4-f beam expanders corresponding to lens pairs of L_1 (Eyepiece E-PL 10x/20, Zeiss, Thornwood, NY) and L_2 (f 100 mm, doublet, AC508-100-B-ML, Thorlabs, Newton, NJ), and L_3 (f 200 mm, doublet, AC508-200-B-ML, Thorlabs, Newton, NJ) and L_4 (f 300 mm, singlet, KPX232AR.16, Newport, Irvine, CA). This arrangement improves the overall f-numbers of the intermediate optics and minimizes the aberrations. After the lens L_2, the scanned laser beam enters the DOE with various angles of incidence (AOI). Within a small range of AOI (in our design ±0.4 °), the performance of the DOE was consistent. The dichroic mirror is located at the mirror position between lens L_4 and the objective lens so that the emission photons reach the MAPMT with a shorter path length (500 mm versus 872 mm of the descanned configuration in Fig 4.1). The same IR blocking filter (BG39, Chroma Technology, Bellows Falls, VT) and the short-pass filter (ET680sp-2p, Chroma Technology, Bellows Falls, VT) are installed before the MAPMT to block the excitation light. Fig 4.3 shows the f-numbers of our two MMM systems optimized for each descanned and non-descanned case using commercially available lenses.

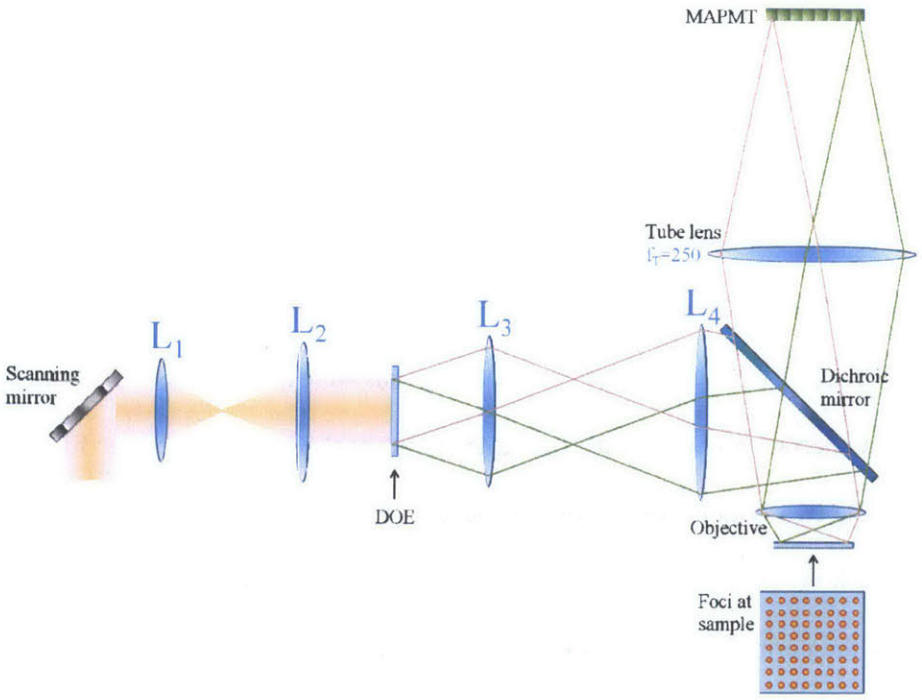

Fig 4.2. The schematic of MMM system with non-descanned detection.

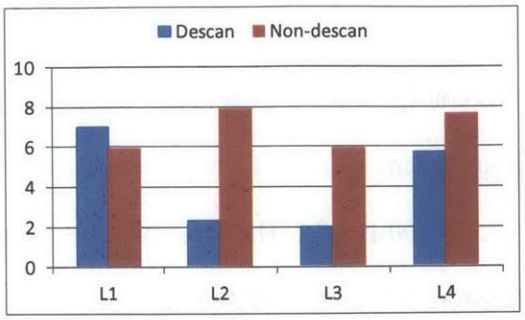

Fig 4.3. The f-numbers of Lens L_1, L_2, L_3, and L_4 in the descanned and non-descanned MMM.

The four lenses in each case were optimized to utilize the full FOV of the 20× objective lens (FOV: 1 mm diameter at a sample plane), which provides about 700 μm × 700 μm scanning area. The lenses that have lower f-numbers generate dominant aberrations for the final PSF at the sample plane. Generally, if the f number is smaller than 10, a doublet or more complex compound lens should be used, instead of a singlet, to minimize aberration [26, 27]. The descanned MMM design contains two low f-number doublet lenses before and after the scanning mirrors (L_2 and L_3), but their f-numbers improves from about 2 in the descanned configuration to over 5 in the non-descanned configuration. The f-number of the lens L_1 is slightly decreased, but it is a theta lens that can be normally used as a scan lens and easily afford the f number 5.9.

4.2.4. ZEMAX simulation for the corner and edge foci of the non-descanned MMM

As discussed above, the non-descanned MMM geometry can avoid low f-numbers optics resulting in less aberrations. With the optical system design software, ZEMAX (Radiant ZEMAX LLC, Bellevue, WA) the aberration coefficients were calculated and spot diagrams were simulated.

With the improved aberration coefficients, the RMS radius of the simulated corner focus became smaller by a factor of 3. The two bottom rows show the actual focus images taken by a camera at the MAPMT location of Fig 4.2. It is visually shown that the second corner focus and edge focus were improved. The middle plots show the normalized PSF profiles of the displayed actual foci, and the improvement was up to two-fold. For more effective comparison, the first corner foci should have been compared, but they

could not be imaged due to beam clipping at the location of lens L_3 of Fig 4.1 in the descanned MMM since there was not an available commercial lens that had the designed focal length with a sufficient diameter to avoid the beam clipping for the four corner beamlets. It should be noted that the actual resolutions of the displayed foci can be different from the measurement by the camera since the images taken by the camera is accumulated intensity signals in 3D rather than 2D PSF measurement for lateral resolution.

Zernike coefficients	Descanned geometry	Non-descanned geometry
Z5 (astigmatism 2,-2)	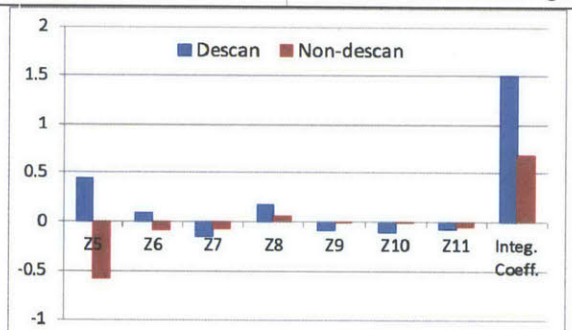	
Z6 (astigmatism 2,2)		
Z7 (coma 3,-1)		
Z8 (coma 3,1)		
Z9 (trefoil 3,-3)		
Z10 (trefoil 3,3)		
Z11 (spherical)		
Integrated coefficient		
Spot diagram of the corner focus (scale bar; left: 40 μm, right: 20 μm)	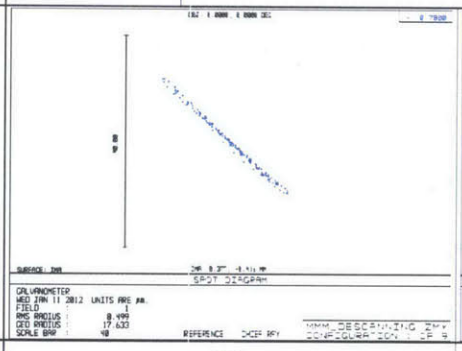	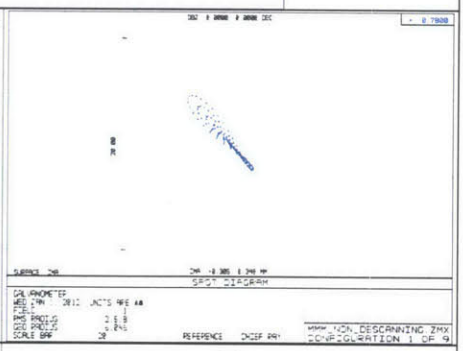
RMS radius (μm)	8.5	2.5
Actual second corner foci (red: non-descan PSF profile, blue: descan PSF profile)	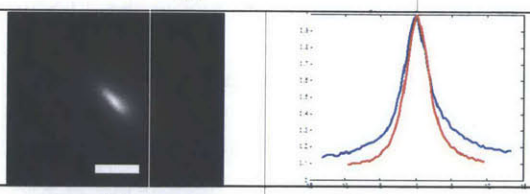	
FWHM	4.5	1.1 × improvement	4.1
Actual edge foci (red: non-descan PSF profile, blue: descan PSF profile)	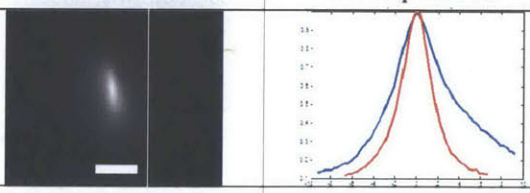	
FWHM	6.6	2 × improvement	3.4

Fig 4.4. The ZEMAX simulation of the excitation foci in the descanned and non-descanned geometry, and their actual images. The scale bars in the actual images are 5 μm long.

4.2.5. Detection strategy: image shifting

The non-descanned MMM is expected to achieve a large FOV with improved PSF. However, in the non-descanned geometry, the emission photons from the n × n excitation foci are no longer stationary at the cathode surface of the MAPMT. Since there are dead spaces between anodes in the MAPMT, the direct telecentric mapping of the emission photons onto the MAPMT results in a loss of information when the foci move onto the dead space during scanning (Fig 4.5 (a)). To avoid the dead spaces of the MAPMT, we demonstrate a detection scheme that involves shifting the specimen and acquiring multiple exposures. Consider a portion of the image (a sub-image) corresponding to the surface area of four neighboring anodes (Fig 4.5(b)). By moving a specimen four times, each quadrant of the sub-image can be collected by the center area of each anode avoiding the dead space (Fig 4.5 (c) and (d)). In addition, when the emission focus is close to the edge of the anode of the MAPMT in one acquisition, another acquisition can collect the same emission photons close to the center of its anode providing the information for the emission photon reassignment to minimize the crosstalk between the anodes. In terms of the number of shift, the minimally required sample shifts to cover the dead spaces is three times (Fig 4.5 (e)), but a four-step movement is preferable to better utilize the center area of each anode where there is less aberration and to ensure more uniform SNR across the final image when the individual captures are synthesized. In our implementation, the specimens were translated by a custom-built manual stage. While our stage is currently slower (a few seconds), the time required for producing the 42.5 μm shift can be accomplished with a commercial high performance stage within a couple of milliseconds. We kept a constant pixel dwell time of 40 μs for both single focus scanning experiment and the descanned MMM experiment. The total data acquisition time was $4/n^2$ shorter than single focus scanning assuming that n × n foci are used. With this approach, most the image acquired 4 times more photons with the exceptions of the small dead spaces where signal either does not increase or increases only twice (Fig 4.5 (d-e)). The four times higher signals result in two times higher SNR according to Poisson noise statistics. The SNR dependences in different regions of the image can be seen from imaging a 300 μM fluorescein solution (Fig 4.5 (f)).

However, it should be noted that we can in principle keep SNR same and shorter acquisition time by 4 and maintain a speed gain of n^2 for n × n foci.

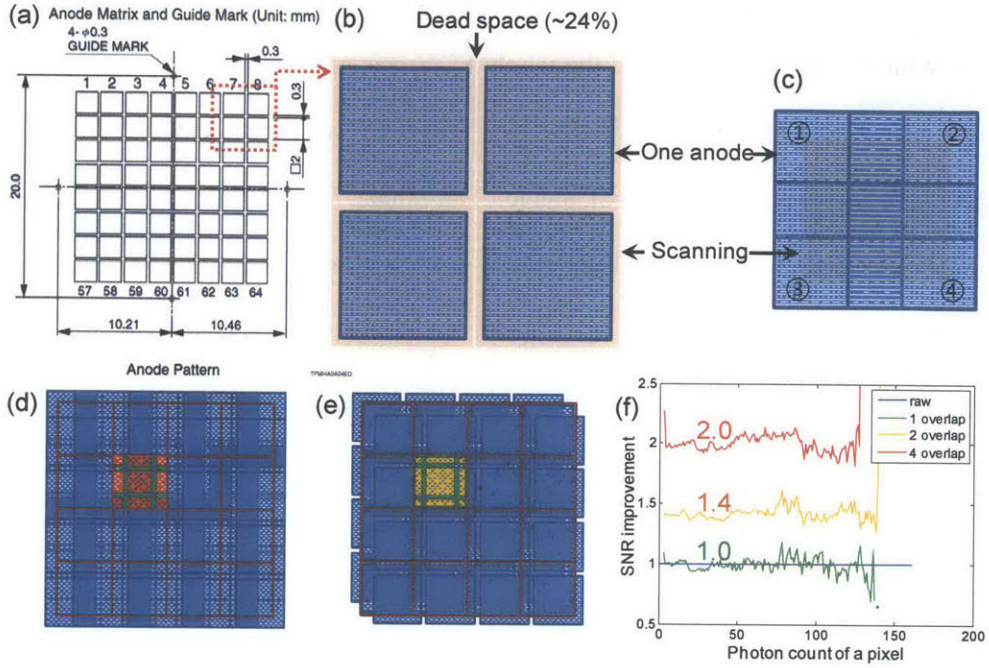

Fig 4.5. The detection scheme of the sample shift. (a) The anode matrix of the MAPMT with 0.3mm dead spaces [28]. (b) The scan areas in a specimen (orange) and the areas covered by the anodes (blue). (c) One scan area covered by 4 time sample shift. (d) Overlapped scan areas with 4 time and (e) 3 time movement in the 4 × 4 MMM case. Red: 4 time, yellow: 3 time, green: 2 time, and violet: 1 time overlap. (f) SNR improvement of each case.

4.3. Result

4.3.1. Fluorescent beads images with 8 × 8 MMM

As a demonstration of the capability of this non-descanned MMM, we started with imaging a fluorescent bead sample. The sample was prepared with 4 μm diameter fluorescent polystyrene microspheres (F8859, Molecular Probes, Eugene, OR) immobilized in 3D by 2 % agarose gel (UltraPure Low Melting Point Agarose, Invitrogen, Carlsbad, CA). Fat emulsion (Microlipid, Nestle, Vevey, Switzerland) was added to the sample in 2 % concentration to mimic the scattering characteristic of typical tissue specimens [29, 30]. The excitation wavelength was 780 nm, and the laser power per focus was adjusted according to the

imaging depth to maximize signal with no excitation satuarion (2.5 mW and 5 mW for 40 μm and 80 μm depth respectively in the non-descanned MMM case, and 15 mW for the single focus scanning case). The dwell time was 40 μs for both cases. The scanning size of one focus in the non-descanned MMM was 85 μm × 85 μm with 0.4 μm resolution and the whole FOV was 680 μm × 680 μm with imaged 8 × 8 foci. As described in section 2.5, the sample was images four times with the x and y shift by 42.5 μm, and the four images were integrated to one final image. The single focus image was scanned with the same resolution (0.4 μm) over a FOV of 410 μm × 410 μm (1024 × 1024 pixels). Cropped images acquired with either methods were displayed in the Fig 4.6 for the better presentation of the 4 μm beads. The acquired raw images are typically not uniform (the center area is brighter than the edge area) because while the x and y scanning mirrors were closely spaced, they cannot be both at the eye-point of the scanning system. Further, there were aberrations due to the large FOV. In addition, the emission signal of the non-descanned MMM is focused and scanned on the cathod surface of the MAPMT, so the acquired image contains the physical pattern of the cathode. To avoid the non-uniformity in the raw images, they were normalized with a 20 time averaged (minimal shot noise) image of a 300 μM uniform fluorescein solution measured as calibration.

Fig 4.6 showed that the non-descanned MMM could successfully image the beads sample. The measured full-width at half-maximum (FWHM) of the bead for the non-descanned MMM and the single focus scanning image were same 4.1 μm at 40 μm depth, and 4.2 and 4.1 μm at 80 μm depth showing the comparable imaging capability of the non-descanned MMM to the single focus scanned image with 16 times improved imaging speed (excluding the four time manual movement of the sample). For further verification we investigated the capability of large fleid of view imaging and compared the emission signal loss between the descanned and non-descanned MMM.

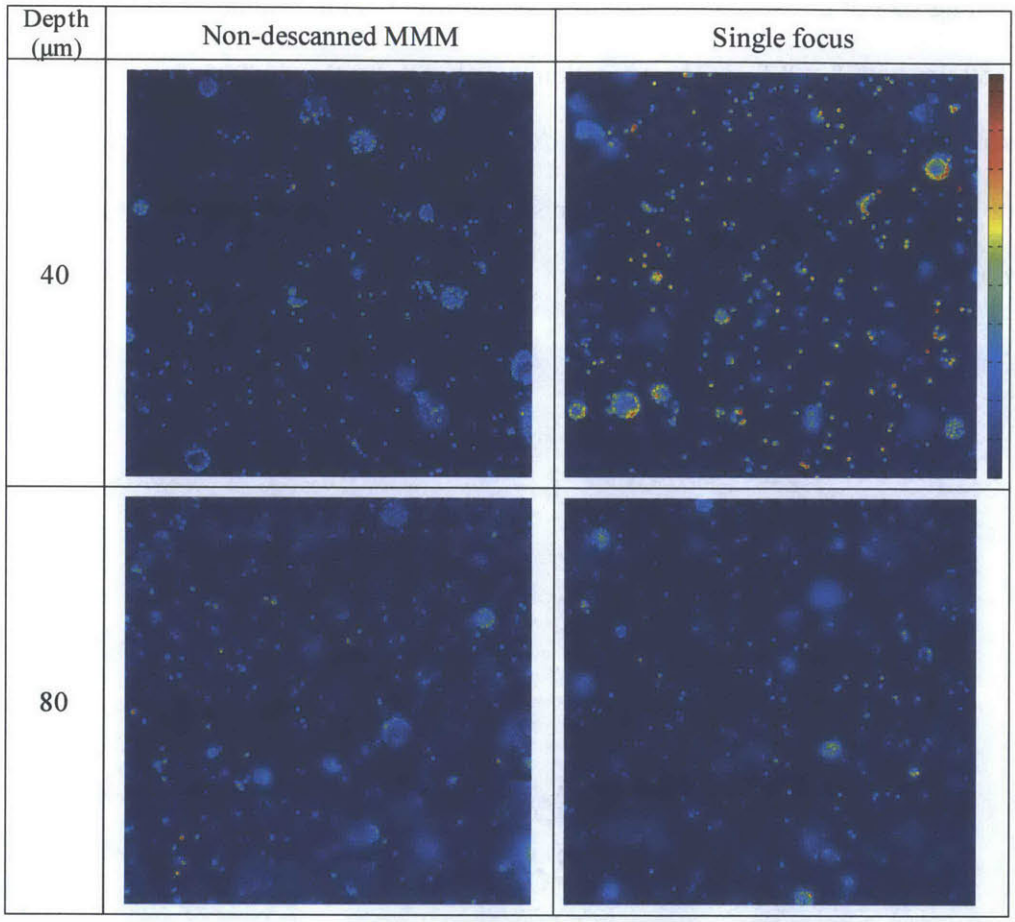

Fig 4.6. Fluorescent bead images in the non-descanned MMM and the standard single focus scanning microscope at 40, and 80 μm imaging depths. The images are 410 μm × 410 μm with 0.4 μm resolution.

4.3.2. Field-of-view comparison

To compare the FOV of the descanned and non-descanned MMM, the same sample was imaged in both systems. The sample was a mouse kidney section labeled with three fluorescent dyes (FluoCells® Prepared Slide #3, F24630, Molecular Probes, Eugene, Oregon). Alexa Fluor® 488 wheat germ agglutinin was used to label elements of the glomeruli and convoluted tubules. The filamentous actin prevalent in glomeruli and the brush border were stained with red-fluorescent Alexa Fluor® 568 phalloidin. Finally, the nuclei were counterstained with the blue-fluorescent DNA stain DAPI. The excitation wavelength was 780 nm, the laser power per focus was about 6 mW, and the dwell time was 40

μs. The scanning size of one focus was 85 μm × 85 μm with 0.4 μm resolution, and the whole FOV was 680 μm × 680 μm with 8 × 8 foci. The excitation wavelength for the single focus scaning was same 780 nm, the laser power was about 10 mW, and the dwell time was 40 μs. The scan size was same 680 μm × 680 μm with 0.5 μm resolution. All the emission signals were collected without spectral separation for all three fluorophores.

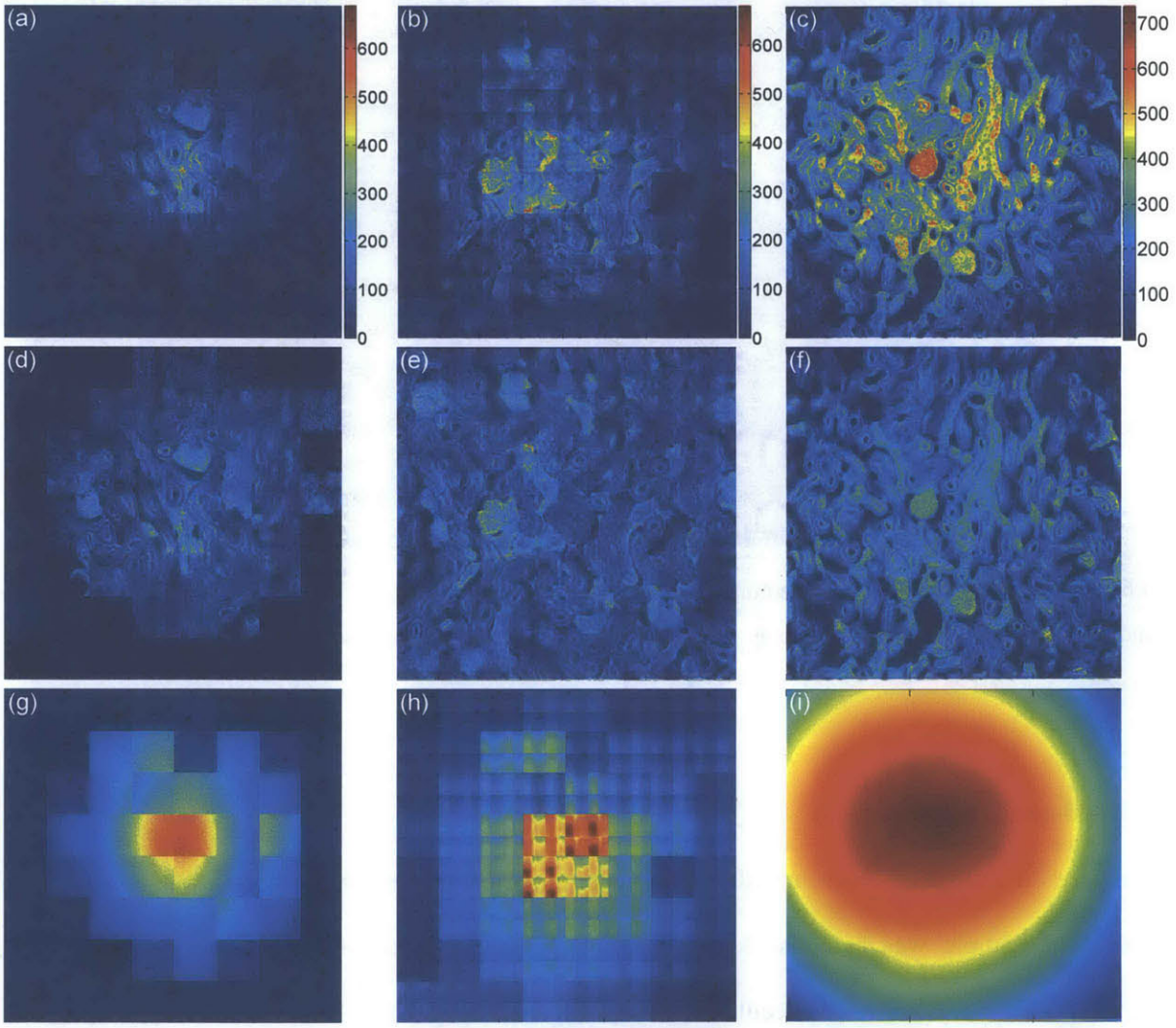

Fig 4.7. Mouse kidney image. (a) Raw image of the descanned MMM, image size: 680 μm × 680 μm with 8 × 8 foci. (b) Raw image of the non-descanned MMM image with the same FOV with the same number of foci. (c) Raw image of the single focus scanning with the same FOV. (d-f) Normalized images of (a-c) with (g-i). (g-i) 20 time averaged fluorescein solution image of each system. The periodic pattern in (h) is the actual shape of the faceplate in front of the cathod in the MAPMT.

Fig 4.7 shows the mouse kidney images taken in the descanned MMM, non-descanned MMM, and the standard single focus scanning microscope. Fig 4.7 (a-c) show the raw images acquired from the three systems. For uniform signal intensity over the full FOV, the three raw mouse kidney images were normalized with the fluorescein solution images (Fig 4.7 (g-i)) acquired in each system with the same imaging condition as described in section 3.1. The final processed non-descanned MMM image (Fig 4.7 (d)) showed that the majority of the FOV of the objective lens can be readily utilized whereas the descanned MMM (Fig 4.7 (e)) had a much more limited FOV. The center area of the both images showed similar SNR but signal attenuation in the radial direction was much more severe in the descanned MMM. Quantitative comparison was shown in Fig 4.8. From around 300 μm radial location, the descanned MMM could not get any signal, but the non-descanned MMM could maintain the emission signals up to the full field size. This signal attenuation of the descanned MMM is due to increasing aberration at the image edge and the subsequent reduction in two-photon excitation efficiency. The non-descanned MMM showed about half signal level compared to the single focus image. This lower signal is mainly due to the non-uniformity of the DOE. The power of the corner beamlet is about 70 % of the center beamlet, which is within the specification (target uniformity of all beamlets: ±15 %). Therefore, inherently the two-photon excitation of the corner focus has only half of the efficiency of the center focus. Due to the non-uniformity of the DOE and the aberrations from the intermediate optics the signal of the non-descanned MMM was lower than the single focus image. However, the non-descanned MMM can image the whole FOV with 16 times faster acquisition time (5 seconds of the non-descanned MMM excluding the manual sample movement time versus 77 seconds of the single focus scanning with the same number of pixels and same pixel size). In addition, it should be noted that the speed improvement can be eventually 64 times maintaining comparable SNR as descrived in section 2.5.

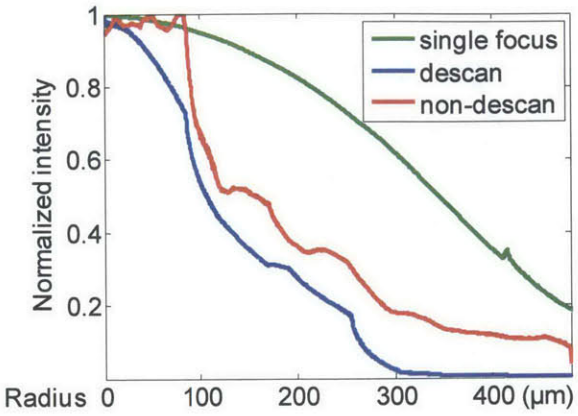

Fig 4.8. Normalized intensity profile comparison of Fig 4.7 (g-i). The distance from the center to the corner of the 680 μm × 680 μm image is 481 μm.

4.3.3. Signal attenuation comparison

We proceed to compare the signal collection efficiency between the descanned and non-descanned MMM in turbid medium. Fat emulsion (Microlipid, Nestle, Vevey, Switzerland) was added to the 300 μM fluorescein solution at 2% concentration same as section 3.1. Images were acquired as a function of imaging depths at every 10 μm. Fig 4.9 shows the signal attenuation in the non-descanned (red) and descanned (blue) MMM. The power of the excitation laser was adjusted to keep the same powers under the objective lens in the both systems. To avoid the non-uniformity of the excitation over the scanning area described above, only the signal at the center area was analyzed in this measurement. With the same excitation laser power and the dwell time, the signal of the non-descanned MMM was higher than that of the descanned MMM. The improvement was shown even at the surface since the forward emission photons were also scattered backwards and collected more in the non-descanned MMM with the shorter optical path and less optical components. The attenuation of the emission signal of the descanned MMM was much faster than the non-descanned MMM. For example, at 30 μm depth, the signal collection efficiency of the non-descanned MMM was three times higher than the descanned MMM. Up to about 150 μm depth, the signal improvement was observed about two-fold.

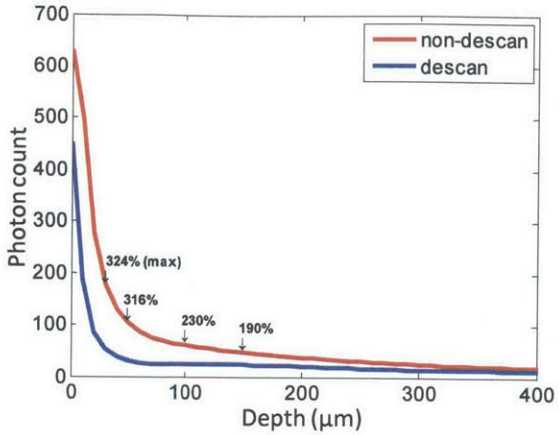

Fig 4.9. Fluorescence emission signal attenuation in the descanned and non-descanned MMM. Data points are connected by lines for eye guidance.

4.3.4. Mouse brain images with 4 × 4 MMM

We further demonstrate the use of non-descanned MMM for thick biological specimen. A Thy1-GFP transgenic mouse [31] was deeply anesthetized with 2.5% Avertin (0.025 ml/g i.p.) and transcardially perfused with PBS, followed by 4% paraformaldehyde. Its brain was dissected and postfixed overnight in cold 4% paraformaldehyde. 300 μm thick coronal sections were sectioned with a vibratome, then mounted and coverslipped on microscope slides using adhesive isolators. To excite the GFP efficiently, the excitation laser wavelength was adjusted to 910 nm. In the previous results the laser power at 780 nm was enough to generate 8 × 8 excitation foci, but the available laser power at 910 nm from the Ti-Sapphire laser was about one third of the power at 780m. Therefore, in this case 4 × 4 foci were generated with the same foci separation, and the total imaging size was 340 μm × 340 μm. The excitation laser power was approximately 35 mW per each excitation focus. Fig 4.10 shows the mouse brain images taken in the descanned MMM, non-descanned MMM, and the standard single focus scanning microscope at 40, 100, and 160 μm imaging depths. For uniform signal intensity, all the images were normalized with the fluorescein solution images acquired in each system with the same imaging condition as described above. The imaging size was 340 μm × 340 μm with 4 × 4 foci (previously 680 μm × 680 μm with 8 × 8 foci). For the smaller FOV, the descanned MMM did not show significant signal loss at the image edge due to

the aberrations as in mouse kidney images. However, the non-descanned MMM could collect more emission signals as confirmed in section 3.3, and show more structural details at 160 μm depth. In the comparison between the non-descanned MMM images and the single focus scanned images, the single focus scanned images showed higher SNR as shown in section 3.2. However, the acquisition of the non-descanned MMM is 4 times faster than the single focus scanning reducing the 1~2 hour imaging time of some neurobiology experiments [32, 33] to 15~30, and possibly 4~8 minutes with further improvement described in section 2.5.

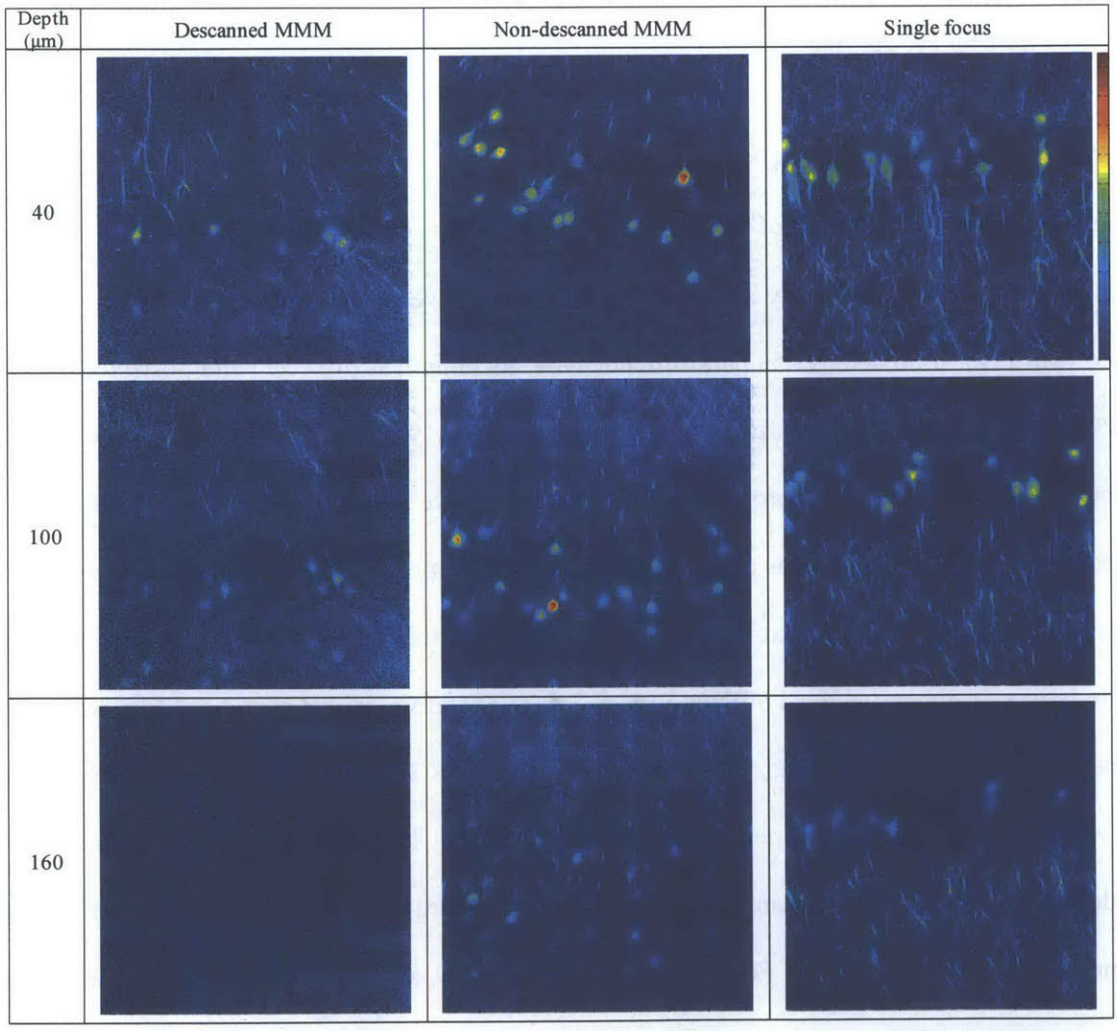

Fig 4.10. Mouse brain images at 40, 100, and 160 μm depths. All images are 340 μm × 340 μm with 0.4 μm pixel size. The left column images are descanned MMM images with 4 × 4 foci. The middle column images are non-descanned MMM images with 4 × 4 foci and the 4 time sample movement. The right column images are the standard single focus scanned images.

For quantitative comparison of signal attenuation between the descanned and non-descanned MMM, the intensity trend of the neuronal cell bodies is plotted as a function of the imaging depth in Fig 4.11. For accurate comparison, only the brightest center parts of the cell bodies were counted. With the same excitation laser power and the dwell time, the signal of the non-descanned MMM was higher than that of the descanned MMM as previously found in section 3.3. The signal improvement was about two- to four-fold over the imaging depths.

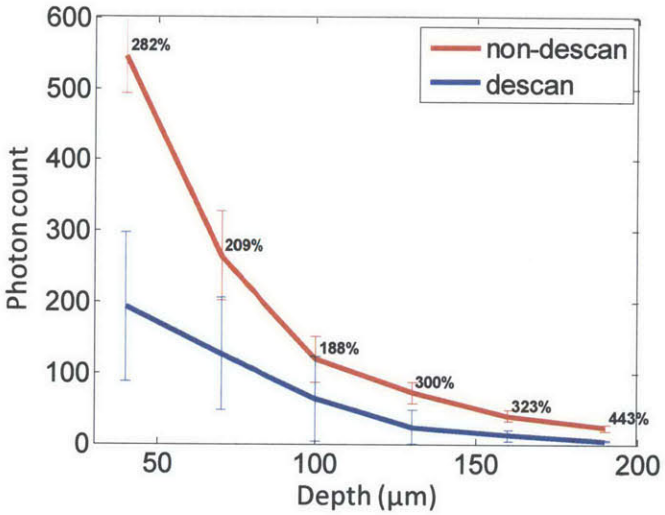

Fig 4.11. The fluorescence emission signal attenuation of the neuronal cell bodies in the descanned and non-descanned MMM. The percentage numbers show the signal improvement, and the error bars show ± one standard deviation at each data point. The data points are connected by lines for eye guidance.

4.4. Discussion

The descanned MMM can achieve better SNR compared to the traditional MMM by suppressing the SNR degradation due to the scattering of emission photons using the MAPMT in the descanned detection configuration. However, it still produces image artifacts, appearing as ghost sub-images, due to channel crosstalk and significant emission signal loss due to the long detection path length. The non-descanned MMM can minimize these ghost images with the maximized foci separation by fully utilizing the FOV of the objective lens with minimal aberrations for corner and edge foci. In addition, the non-descanned MMM can minimize the detection path length so that the signal collection efficiency can be improved up

to four-fold. However, the emission signals are no longer stationary on the detector due to scanning, and a new detection scheme is necessary. We introduced a detection scheme of shifting a specimen and imaging four times. With four time acquisition of the emission signals by locating the specimen at the corresponding quadrant of one image, the non-stationary signals could be collected with avoiding the dead space of the MAPMT. Further, maximum imaging speed improvement equal to the number of foci can be achieved with high performance scanners and stage to obtain comparable SNR with single focus scanning.

In addition to the sample shift and multiple imaging, another potential approach is the use of multiple detectors. Instead of moving and imaging a specimen several times, the use of multiple MAPMTs with split emission signals can achieve imaging with one time scanning and comparable SNR by covering different locations of a specimen and avoiding the signal loss due to the dead space. However, implementing multiple MAPMTs requires substantial more complex electronics, e.g. 256 acquisition channels for four 8×8 anode MAPMTs. Another possible option would be the use of a custom parabolic light collector array that has minimal dead space between elements at the entrance and can funnel the emission photons reaching each element to the center area of a corresponding MAPMT anode. The custom parabolic light collector (CPC) array may avoid either the sample movement or the complex data acquisition electronics system with the use of multiple MAPMT detectors, and may allow the single shot imaging with one MAPMT. However, the CPC should be fabricated with high precision for the inlet size of the CPC exactly matching to the anode matrix size of the MAPMT. The trade-off in the use of CPC is the more pronounced crosstalk between anodes requiring a more effective image post processing algorithm. Another detection method is to use a fast camera and take an image at every scanning point. The locations of focused emission photons from the multiple foci at each pixel can be easily predicted with imaging a non-scattering sample (e.g. a fluorescein solution) in advance, and then the scattered emission photons from a general specimen can be also collected by integrating the specific area of the camera image for each focus to minimize the crosstalk between neighbors, which realizes a virtual

MAPMT in the non-descanned detection configuration. We have substantially investigated this method, but it turned out that the accumulated readout noise during integrating a large number of pixels for each focus significantly degraded SNR and made this method inapplicable.

In any case, it is true that the SNR of the standard single focus scanning two-photon microscope can often achieve better SNR than the MMM. However, many applications with bright specimens have fairly good SNR but minimizing the acquisition time is critical. In this case, MMM can be a more desirable imaging solution, and the non-descanned MMM can perform better with higher SNR and less crosstalk with a large FOV compared with the previous version of descanned MMM. If the applications deal with relative transparent specimens [34-36] or shallower depths where scattering is not critical, other approaches such as two-photon wide-field microscopy [11, 12, 37] or light sheet microscopy [38, 39] may provide faster imaging speed with comparable SNR.

References

1. Denk, W., J.H. Strickler, and W.W. Webb, *2-PHOTON LASER SCANNING FLUORESCENCE MICROSCOPY.* Science, 1990. **248**(4951): p. 73-76.
2. So, P.T.C., et al., *Two-photon excitation fluorescence microscopy.* Annual Review of Biomedical Engineering, 2000. **2**: p. 399-429.
3. Kim, K.H., C. Buehler, and P.T.C. So, *High-speed, two-photon scanning microscope.* Applied optics, 1999. **38**(28): p. 6004-6009.
4. Fan, G., et al., *Video-rate scanning two-photon excitation fluorescence microscopy and ratio imaging with cameleons.* Biophysical journal, 1999. **76**(5): p. 2412-2420.
5. Iyer, V., B.E. Losavio, and P. Saggau, *Compensation of spatial and temporal dispersion for acousto-optic multiphoton laser-scanning microscopy.* Journal of Biomedical Optics, 2003. **8**: p. 460.
6. Reddy, G.D. and P. Saggau, *Fast three-dimensional laser scanning scheme using acousto-optic deflectors.* Journal of Biomedical Optics, 2005. **10**: p. 064038.
7. Zeng, S., et al., *Simultaneous compensation for spatial and temporal dispersion of acousto-optical deflectors for two-dimensional scanning with a single prism.* Optics Letters, 2006. **31**(8): p. 1091-1093.
8. Katona, G., et al., *Fast two-photon in vivo imaging with three-dimensional random-access scanning in large tissue volumes.* Nature methods, 2012. **9**(2): p. 201-208.
9. Zipfel, W.R., R.M. Williams, and W.W. Webb, *Nonlinear magic: multiphoton microscopy in the biosciences.* Nature biotechnology, 2003. **21**(11): p. 1369-1377.
10. Cianci, G.C., J. Wu, and K.M. Berland, *Saturation modified point spread functions in two-photon microscopy.* Microscopy research and technique, 2004. **64**(2): p. 135-141.
11. Oron, D., E. Tal, and Y. Silberberg, *Scanningless depth-resolved microscopy.* Optics Express, 2005. **13**(5): p. 1468-1476.
12. Zhu, G., et al. *Simultaneous spatial and temporal focusing of femtosecond pulses.* 2005: Optical Society of America.
13. Bewersdorf, J., R. Pick, and S.W. Hell, *Multifocal multiphoton microscopy.* Optics Letters, 1998. **23**(9): p. 655-657.

14. Buist, A.H., et al., *Real time two-photon absorption microscopy using multi point excitation.* Journal of Microscopy-Oxford, 1998. **192**: p. 217-226.
15. Sacconi, L., et al., *Multiphoton multifocal microscopy exploiting a diffractive optical element.* Optics Letters, 2003. **28**(20): p. 1918-1920.
16. Watson, B.O., V. Nikolenko, and R. Yuste, *Two-photon imaging with diffractive optical elements.* Frontiers in neural circuits, 2009. **3**.
17. Kim, K.H., et al., *Multifocal multiphoton microscopy based on multianode photomultiplier tubes.* Optics Express, 2007. **15**(18): p. 11658-11678.
18. Martini, J., V. Andresen, and D. Anselmetti, *Scattering suppression and confocal detection in multifocal multiphoton microscopy.* Journal of biomedical optics, 2007. **12**(3): p. 034010-034010-6.
19. Le Grand, Y., et al., *Non-descanned versus descanned epifluorescence collection in two-photon microscopy: Experiments and Monte Carlo simulations.* Optics Communications, 2008. **281**(21): p. 5480-5486.
20. Zinter, J.P. and M.J. Levene, *Maximizing fluorescence collection efficiency in multiphoton microscopy.* Optics Express, 2011. **19**(16): p. 15348.
21. Minsky, M., *Microscopy apparatus.* 1961, US Patent 3013467.
22. Sheppard, C. and A. Choudhury, *Image formation in the scanning microscope.* Journal of Modern Optics, 1977. **24**(10): p. 1051-1073.
23. Brakenhoff, G., P. Blom, and P. Barends, *Confocal scanning light microscopy with high aperture immersion lenses.* Journal of microscopy, 1979. **117**(2): p. 219-232.
24. Carlsson, K. and N. Åslund, *Confocal imaging for 3-D digital microscopy.* Applied optics, 1987. **26**(16): p. 3232-3238.
25. Pawley, J., *Handbook of biological confocal microscopy.* 2006: Springer.
26. Fischer, R.E., et al., *Optical system design.* 2000.
27. *Lens Selection Guide*, in *THE NEWPORT RESOURCE.*
28. *Multianode Photomultiplier Tube Assembly H7546A, H7546B*, HAMAMATSU.
29. Dunn, A.K., et al., *Influence of optical properties on two-photon fluorescence imaging in turbid samples.* Applied optics, 2000. **39**(7): p. 1194-1201.
30. Dong, C.-Y., K. Koenig, and P. So, *Characterizing point spread functions of two-photon fluorescence microscopy in turbid medium.* Journal of biomedical optics, 2003. **8**(3): p. 450-459.
31. Feng, G., et al., *Imaging neuronal subsets in transgenic mice expressing multiple spectral variants of GFP.* Neuron, 2000. **28**(1): p. 41-51.
32. Chen, J.L., et al., *Structural basis for the role of inhibition in facilitating adult brain plasticity.* Nature neuroscience, 2011. **14**(5): p. 587-594.
33. Chen, J.L., et al., *Clustered dynamics of inhibitory synapses and dendritic spines in the adult neocortex.* Neuron, 2012. **74**(2): p. 361-373.
34. Tuchin, V.V., *Optical clearing of tissues and blood.* Vol. 154. 2006: SPIE Press Bellingham.
35. Dodt, H.-U., et al., *Ultramicroscopy: three-dimensional visualization of neuronal networks in the whole mouse brain.* Nature methods, 2007. **4**(4): p. 331-336.
36. Chung, K. and K. Deisseroth, *CLARITY for mapping the nervous system.* Nature methods, 2013. **10**(6): p. 508-513.
37. Cheng, L.-C., et al., *Spatiotemporal focusing-based widefield multiphoton microscopy for fast optical sectioning.* Optics Express, 2012. **20**(8): p. 8939-8948.
38. Fuchs, E., et al., *Thin laser light sheet microscope for microbial oceanography.* Optics Express, 2002. **10**(2): p. 145.
39. Keller, P.J., et al., *Reconstruction of zebrafish early embryonic development by scanned light sheet microscopy.* Science, 2008. **322**(5904): p. 1065-1069.

Chapter 5

Spectral-Resolved Multifocal Multiphoton Microscopy with Multianode Photomultiplier Tube

5.1. Introduction

Multiphoton excitation fluorescence microscopy has inherent 3D resolution due to the nonlinear dependence of excitation efficiency on the incident light flux [1-3]. Multiphoton excitation can be localized to a femtoliter region at the focal point of a high numerical aperture objective lens reducing specimen photodamage and photobleaching. Multiphoton microscopy further can excite common fluorophores with infrared radiation enhancing excitation light penetration depth in turbid specimens where scattering is reduced. Equally importantly, unlike confocal microscopy, no confocal pinhole is required for depth resolution allowing scattered emission photons to be collected effectively greatly enhancing image signal to noise ratio (SNR) in turbid specimens. Consequently, multiphoton excitation fluorescence microscopy has become the preferred tool for deep imaging of highly scattering tissue specimens [4]. In many applications, high speed imaging is critical. For example, high speed imaging is useful for some studies of neuronal plasticity that may require high resolution mapping the whole dendritic arbor, covering almost 1 mm^3 in volume, while minimizing the period of anesthesia to reduce animal stress [5-10]. One of the methods to improve the imaging speed is multifocal multiphoton microscopy (MMM) [11, 12]. With a lenslet array or diffractive optical element (DOE) [13, 14], a number of foci are generated simultaneously in a specimen and scanned together. Each excitation focus scans a fraction of the whole imaging area; the final image is synthesized by montaging the data from each focus. Within the limit of the available laser power, the number of foci can be maximized and the imaging speed

can be improved in proportion to the number of foci. The early MMM used imaging detectors, such as CCD cameras, to record emission signals from multiple foci simultaneously. However, the turbidity of typical biological specimens scattered emission photons to neighbor pixels resulting in a blurred image with degraded SNR. This difficulty was recently partly circumvented by introducing descanned MMM using a detection scheme based on using a multianode photomultiplier tube (MAPMT). With this approach, the scattered emission photons are much more effectively collected by the large area anodes that corresponds to tens of micron size areas on the specimen plane providing much better immunity to SNR degradation due to emission photon scattering [15].

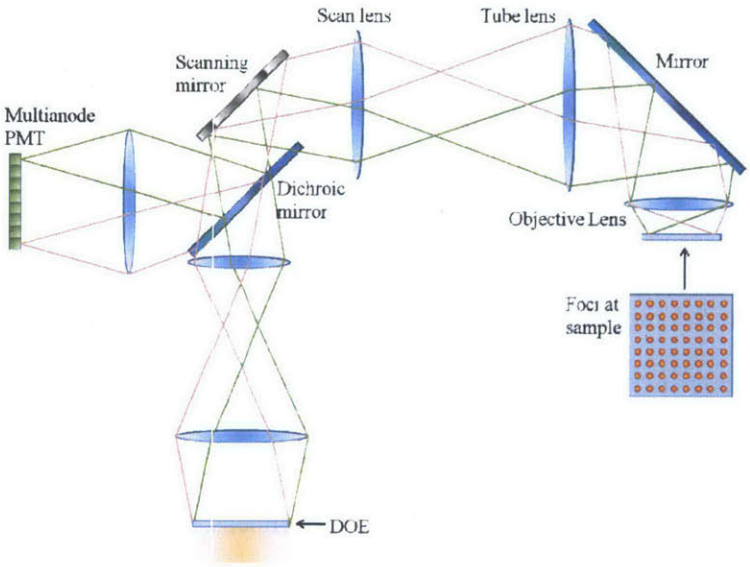

Fig 5.1. The Schematic of MMM.

Fig 5.1 shows the schematic of a MMM system. The excitation laser light is divided to several beamlets by the DOE, and they are delivered to the scanning mirrors with different angles by two lenses in the 4-f location. All the beamlets are scanned by the scanning mirrors together, and expanded to slightly overfill the back aperture of the objective lens. The beamlets enter the objective lens with different incident angles, are focused in the sample, and generate the multiple excitation foci distributed into a square 2D array. The emission signals from the foci are collected by the same objective lens, travel along the same beam path as the excitation light, and are descanned by the same scanning mirrors. As the arrival time of

the emission photons is much faster than the dwell time for one pixel, the emission photons from each focus are descanned and become stationary. The emission photons are separated by the dichroic mirror from the excitation laser light, and focused at the cathode locations that correspond to the center of each anode of the MAPMT. With the large area of the each anode, much of the scattered emission photons can be effectively collected in the designated channels. The deleterious effect of emission photon scattering can be effectively suppressed.

Many applications require not only high imaging speed but also the simultaneous detection of multiple fluorophores to delineate structural relationships between different cellular and tissue constituents. Other applications would require the imaging of multiple spectral ranges to assay tissue metabolic and biochemical states using ratiometric fluorescent sensors. For example, multicolor imaging is critical in the study of brain function. Recently, this approach has been used to study synapse formation and dissociation in the context of dendritic remodeling in a mammalian brain [16-18]. An essential feature of the mammalian brain is its capacity to adapt in response to the environment. This experience-dependent plasticity is thought to involve the remodeling of synaptic connections between neurons. By monitoring inhibitory and excitatory synapses of dendritic spines it has been investigated how synapse dynamics accompanies dendritic arbor rearrangements. To simultaneously monitor the multiple fluorophores marking dendrites, excitatory synapses and inhibitory synapses, spectral detection is essential. At the same time, the imaging speed remains critical in order to image the large dendrite arbor at high resolution so that individual synapses can be reliably resolved. Therefore, the addition of spectral detection capability into a MAPMT based MMM is important.

High speed imaging and spectral detection can, in principle, be accomplished by spectrally separating the emission light using dichroic mirrors and directing the different spectral components to multiple MAPMTs. However, MAPMTs are relatively bulky and a system with multiple detectors with their associated optics will have a very long detection optical path resulting in substantial loss of scattered emission photons [15]. Today, several groups have investigated various types of the spectral-resolved

MMM. A MMM system with temporal and spectral resolution has been developed with a specially designed streak camera [19-21]. The same group later has developed a spectral-resolved MMM with a CCD camera with an one-axis descanned configuration [22]. In addition, a spectrometer-integrated MMM using an optical multiplexer has been developed [23-25]. However, these previous investigation require specimen scanning or the use of a pulse multiplexing that limits image speed improvement. Here we introduce a spectral-resolved MMM by implementing the spectral detection in a descanned MMM system using a MAPMT. Previous designs of MAPMT based MMMs with descanned configuration utilized 2D array of the excitation foci mapping to the physical anode matrix of the MAPMT. Instead of producing a 2D array of excitation foci, spectral-resolved MAPMT based MMM generates a linear array of excitation foci. The spectral information can be acquired in the orthogonal axis of the MAPMT simultaneously. This approach doesn't require extending of the detection light path that often suffers from significant signal loss.

5.2. Method

5.2.1. System configuration

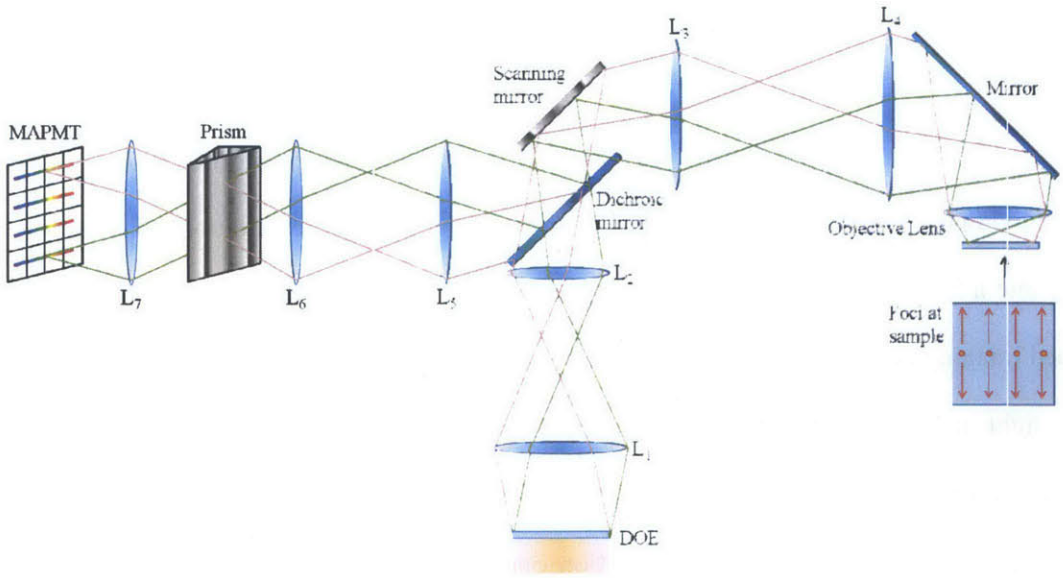

Fig 5.2. The configuration of the spectral-resolved MMM.

Fig 5.2 shows the spectral-resolved MMM. The excitation light path is same as the previously described [15]. The femtosecond light source used was a Chameleon Ultra II (Coherent, Santa Clara, CA). The excitation laser beam was split into 4 × 1 beamlets with a DOE (customized, Holo/Or, Rehovoth, Israel). The beamlets were sent to the scanning mirrors (6215H, Cambridge Technology, Lexington, MA) through the lens L_1 (f 300 mm, singlet, KPX232AR.16, Newport, Irvine, CA) and lens L_2 (f 75 mm, doublet, AC508-075-B-ML, Thorlabs, Newton, NJ) in a 4-f configuration and scanned together. The beamlets were expanded by the lens L_3 (f 35 mm, doublet, AC254-035-B-ML, Thorlabs, Newton, NJ) and lens L_4 (f 175 mm, singlet, KPX196AR.16, Newport, Irvine, CA) to slightly overfill the back aperture of the objective lens (W Plan-Apochromat, 20 ×, 1.0 NA, Zeiss, Thornwood, NY). The 4 × 1 excitation foci were generated in a sample with 85 μm separations, and each focus scanned 85 μm × 340 μm area, so the total imaging size was 340 μm × 340 μm. The emission photons were collected by the same objective lens, delivered along the same optical path as the excitation beam path, and descanned by the scanning mirrors. The stationary emission light after descanning was separated from the excitation laser light by the dichroic mirror (Chroma Technology, Bellows Falls, VT), relayed by lens L_5 (f 62.9 mm, singlet, KPX085AR.14, Newport, Irvine, CA) and lens L_6 (f 150 mm, doublet, AC508-150-A-ML, Thorlabs, Newton, NJ), and spectrally separated by a prism (PS853, Thorlabs, Newton, NJ) that anti-reflection coated (Chroma Technology, Bellows Falls, VT). For the spectral decomposition, a grating is an alternative choice. However, the grating generally suffers from significant light loss and its diffraction efficiency can varied substantially across the spectral range. In contrast, a prism has greater efficiency and more uniform sensitivity over a broader spectral range. However, prisms are less dispersive than gratings. Therefore, we have utilized two prisms to achieve our designed spectral dispersion power. The spatially separated and spectrally dispersed emission light was focused onto a MAPMT (H7546B-20, Hamamatsu, Bridgewater, NJ) through lens L_7 (f 100 mm, doublet, AC508-100-A-ML, Thorlabs, Newton, NJ). The double prisms and the lens L_7 were designed to collect the range of the emission spectra of typical fluorescent proteins (from teal to red fluorescent proteins). A BG39 (Chroma Technology, Bellows Falls,

VT) and a shortpass filter (ET680sp-2p, Chroma Technology, Bellows Falls, VT) were installed in front of the MAPMT to block the excitation IR and pass only the emission photons in the designed spectral range. Since the MAPMT has 8 × 8 channels, only 4 rows were used for the spatial separated foci while all 8 columns were used for 8 channels in spectral resolved detection. However, while we choose to use only 4 excitation foci, a different DOE can be fabricated to generate 8 foci to utilize the full 8 × 8 channels of the MAPMT. Further, within the available laser power, the use of multiple MAPMTs can improve the imaging speed more, e.g. placing two 8 × 8 MAPMTs side-by-side allowing 16 foci scanning in parallel with 8 simultaneous spectral channels. A single-photon avalanche diode (SPAD) array can be another choice with its large number of pixels and higher quantum efficiency for further imaging speed improvement and more spectral channels [26-28]. However, it should be noted that the SPAD array has typically a low fill-factor (around 10%) resulting in the loss of emission photons. This limitation may be overcome in the future with the use of a matching micro-lenslet array that takes the photon falling within each lenslet to the corresponding active area of each pixel.

5.2.2. Spectral decomposition

Spectral decomposition is routinely done by linear unmixing on a pixel by pixel basis.

$$\begin{bmatrix} J_1 \\ J_2 \\ \vdots \\ J_m \end{bmatrix} = \begin{bmatrix} s_{11} & s_{12} & \cdots & s_{1n} \\ s_{21} & s_{22} & \cdots & s_{2n} \\ \vdots & \vdots & \ddots & \vdots \\ s_{m1} & s_{m2} & \cdots & s_{mn} \end{bmatrix} \begin{bmatrix} I_1 \\ I_2 \\ \vdots \\ I_n \end{bmatrix} \quad (1)$$

where [I] is an n × 1 matrix representing the concentration of n fluorophore species that is to be determined, [S] is an m × n matrix representing the known spectra of the n species distributed in m detected spectral channels, and [J] is an m × 1 matrix representing the measured spectrally mixed signals of all the fluorophores collected in the m^{th} spectral channel. If [S] is known, retrieving [I] can be simply done by matrix inversion. [S] can be readily estimated in two ways. First, imaging each fluorophore with our system can provide the required spectral distribution information (Fig 5.3 (a)). This method gives perfect estimation, but it requires multiple calibration measurements performed in advance. The second

method is to estimate [S] with the known spectrum of each fluorophore. For the typical organic dyes or fluorescent proteins, their emission spectra are well known. With these known spectra, the required spectral distribution of each fluorophore can be estimated using the known wavelength dependent detection efficiency of our microscope taking into account transmittance of optics (e.g. dichroic and barrier filters) and the quantum efficiency of the MAPMT (Fig 5.3 (b)). In any case, the estimated spectral distribution is normalized to make the sum of the coefficients one so that the total photon count is preserved after unmixing.

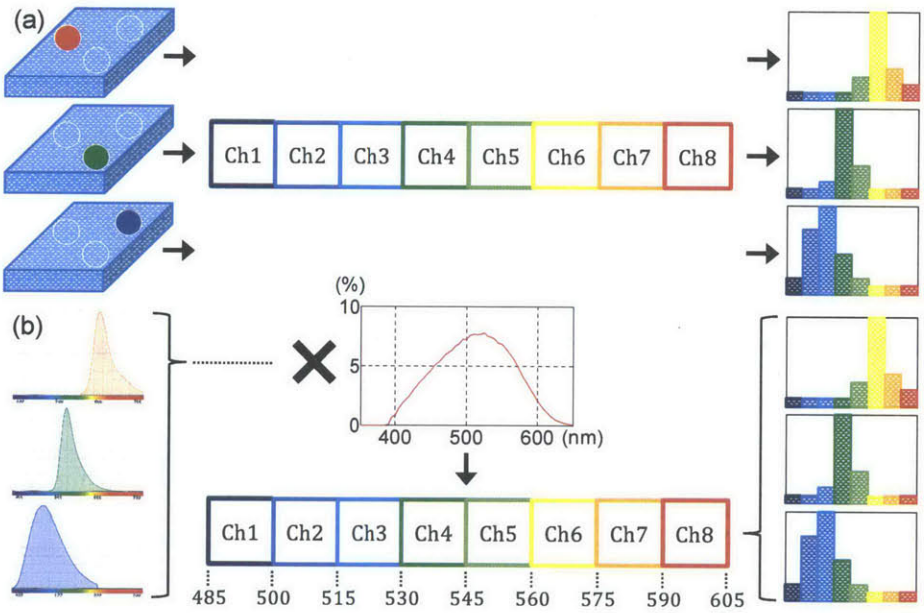

Fig 5.3. Spectral distribution estimation by (a) imaging the single-color samples with 8 channels or (b) based on the known emission spectrum of each specimen. The graph in (b) shows the total detection efficiency as a function of wavelength. The spectral calibration is discussed in section 3.1.

5.3. Result

5.3.1. Detection channel calibration

For spectral calibration of the eight spectral channels, several known samples have been used: Quinine Sulfate (emission peak (Em): 460 nm, R-14782, Molecular Probes, Eugene, OR), Fluorescein (Em: 513 nm, R-14782, Molecular Probes, Eugene, OR), yellow-green beads (Em: 515 nm, F8859, Molecular

Probes, Eugene, OR), orange beads (Em: 560 nm, F8833, Molecular Probes, Eugene, OR), red beads (Em: 605 nm, F8842, Molecular Probes, Eugene, OR), and several second harmonic generation signals from a collagen sample (475 nm to 537.5 nm with an increment of 12.5 nm from the Ti-Sa laser that generates the maximum output wavelength of 1075 nm). With these calibration samples, the detector was installed to collect from 485 nm to 605 nm with every 15 nm wavelength window.

5.3.2. Three color fluorescent beads

We first evaluated the performance of the spectral-resolved MMM with a three color fluorescent bead sample. Three different fluorescent polystyrene microspheres (F8859: yellow-green, F8833: orange, and F8842: red, Molecular Probes, Eugene, OR) were mixed and immobilized in 3D by 2 % agarose gel (UltraPure Low Melting Point Agarose, Invitrogen, Carlsbad, CA). Different sizes of beads (4, 10, and 15 μm diameter) were intentionally chosen for each color bead so that the correct species assignment based on spectral unmixing can be readily verified based on bead size. The excitation wavelength was 910 nm, the laser power was about 5mW per focus, and the dwell time was 40 μs per 0.5 μm pixel resolution. Fig 5.4 shows the three bead image. The acquired raw images for each wavelength channel are shown in (a). Individual raw image is not directly corresponding to different types of beads due to the typically board fluorescent spectra of fluorophores and the resulting spectral overlap. Since the spectrum of each bead is distributed differently onto the eight spectral channels, the identity of each beads can be determined based on the spectral unmixing algorithm as described in section 2.2. Fig 5.4 (b) shows the spectral distribution of the three color bead over the eight channels. The fractional intensities of each spectrum on each spectral channel are normalized such that the area under the each curve is unity preserving the original photon count in the spectral unmixing process. From the acquired coefficients, the eight raw images were processed with matrix calculation for the three decomposed images shown in Fig 5.4 (c). The final processed image showed the spectral-resolved MMM could successfully image the three color bead sample with spectral resolution at four times faster speed than single focus scanning. The full-width at

half-maximum (FWHM) of the three different beads expectedly showed good agreement with their specified sizes (4.1, 10.1, and 15.2 μm for each 4, 10, and 15 μm bead) demonstrating the spatial resolution of this system. For over hundreds of beads imaged, there was no mis-assignment in the spectral unmixing process.

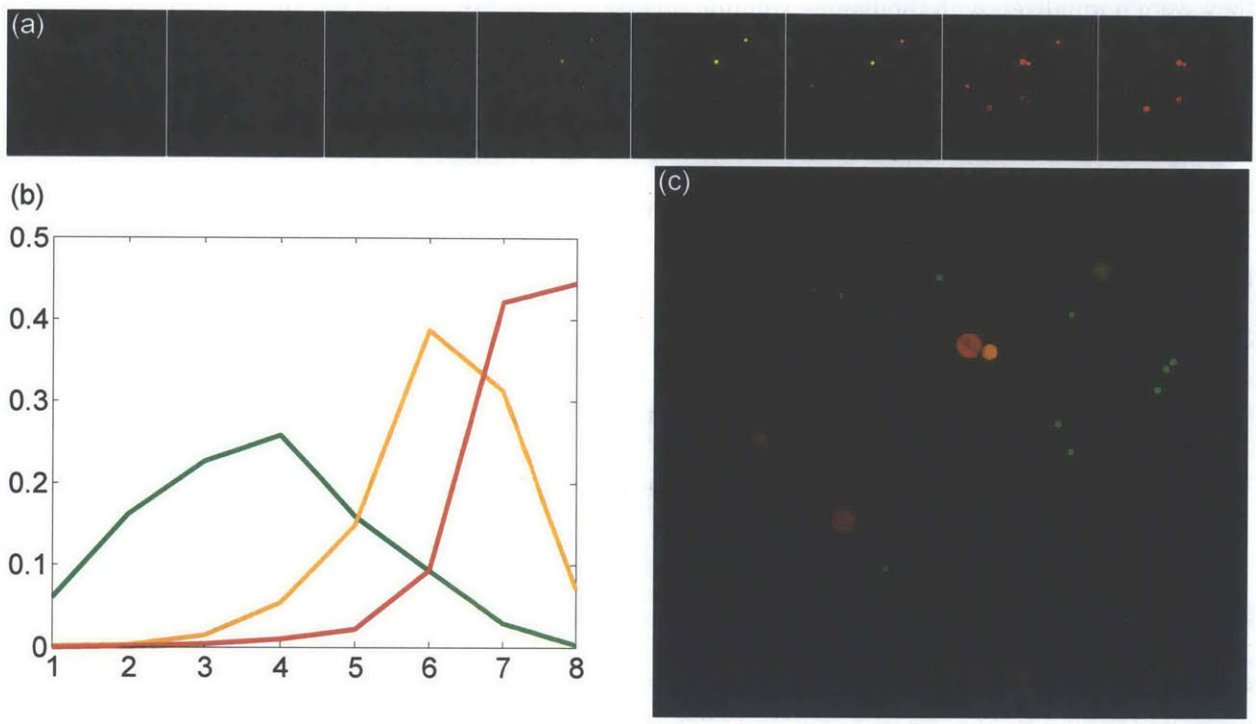

Fig 5.4. Three color fluorescent bead image. (a) Eight channel images in pseudo colors for display purpose. The raw image of each channel contains only combined intensity information. (b) The spectrum of each bead on the eight channels. (c) Processed image in pseudo colors. The image size is 340 μm × 340 μm.

5.3.3. Mouse kidney image

We further tested the system with a fixed mouse kidney sample labeled with three fluorescent dyes (FluoCells® Prepared Slide #3, F24630, Molecular Probes, Eugene, Oregon). Red-fluorescent Alexa Fluor® 568 phalloidin was used to label the filamentous actin. Green-fluorescent Alexa Fluor® 488 wheat germ agglutinin was used to label glycoproteins or glycolipids in the membrane. Finally, the nuclei were counterstained with the blue-fluorescent DAPI. The excitation wavelength was 780 nm, the laser

power was about 11 mW per focus, and the dwell time was 40 μs per 0.5 μm pixel resolution. The acquired raw images are typically not uniform (the center area is brighter than the edge area) because while the x and y scanning mirrors are closely spaced, they cannot be both at the eye-point of the scanning system. In addition, the four foci are under different aberration condition, so the center two sub-images are brighter than the top and bottom sub-images. To avoid the non-uniformity in the raw images, they were normalized with rhodamine solution images. A 1 mM rhodamine 6G solution was imaged with each spectral channel by moving the MAPMT to record the same peak intensity signal onto each channel, and the acquired raw images were normalized with the rhodamine solution images. Similar to the three color bead sample described in section 3.2, the three emission signals of the mouse kidney sample were recorded in the eight channels. For the fluorescent bead image, the unmixing is very straight forward since the beads are sparsely distributed beads spatially with almost no mixed contribution from more than one species in a single pixel. However, in this mouse kidney sample the three fluorophores are distributed within the complex tissue structures with significant spatial overlaps resulting in significant spectral overlap within each pixel. We first estimate of the spectrum of each fluorescent dye based on their known emission spectrum (Molecular Probes, Eugene, Oregon) and the wavelength dependent detection efficiency of this MMM system as described in section 2.2. The three colors were decomposed with the estimated spectral distribution, and showed in one image. Fig 5.5 shows that the system could successfully image the sample with details in the three different fluorophores. The acquired image matched well with images of similarly labeled samples acquired with other spectral resolved methods [29]. The distribution of three unmixed species corresponded well to the expected morphology of the underlying tissue components. The blue arrow in Fig 5.5 points to a representative nucleus labeled with DAPI showing the expected ellipsoidal geometry. The green arrows in Fig 5.5 point to tufts of capillaries forming the glomeruli in the kidney with the endothelial cell plasma membrane labeled with wheat germ agglutinin. The red arrow in Fig 5.5 points to filamentary structures of actin cytoskeleton of cells contained in the glomeruli and the brush border of proximal convoluted tubules. It should be noted that

the image size was 290 μm × 340 μm rather than a square shape due to the mismatch of the laser wavelength and the DOE specification. The DOE installed in the system was designed to generate 4 × 4 beamlets with 0.8 ° separation angle at 910 nm wavelength. However, in this case 780 nm wavelength was used for efficient excitation. Therefore, the excitation laser was slightly less diffracted than the designed angle resulting in the shortening of one spatial dimension by 50 μm.

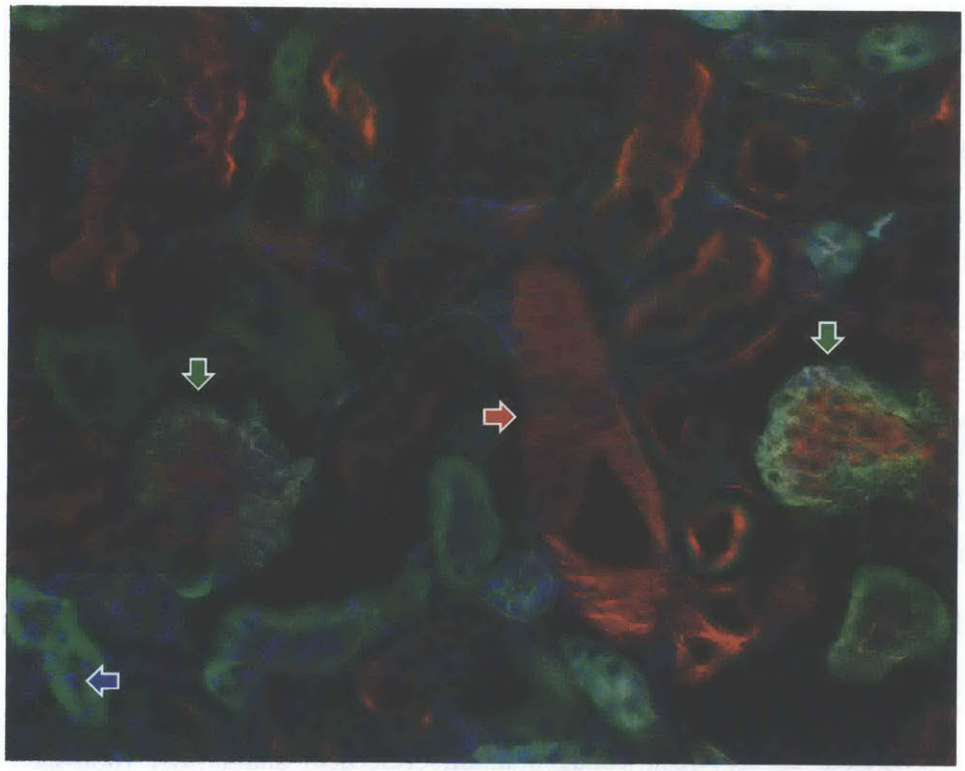

Fig 5.5. A mouse kidney image labeled with three colors. The red arrow indicates representative actin labeled with phalloidin, the green arrows show glomeruli labeled with Alexa 488, and the blue arrow for nuclei.

5.3.4. Nerve sample image

The capabilities of the spectral-resolved MMM are further demonstrated by imaging ex vivo samples of rat sciatic nerves that had been fully transected, entubulated inside a porous collagen scaffold, and harvested from the sacrificed animal one week later [30]. The nerve tissue was gently fixed by 4% paraformaldehyde, embedded in OCT medium, sectioned, stained using a primary antibody against α

smooth muscle actin (αSMA; A5228, Sigma Aldrich, St. Louis, MO) that is detected by an Alexa Fluor 488-conjugated anti-mouse secondary antibody, and counterstained by DAPI (binds nucleic acids), and TRITC-conjugated phalloidin (binds to F-actin) [31]. The laser excitation wavelength was 780 nm, power per focus was about 18 mW, and the dwell time was 40 μs per 0.5 μm pixel. The image field of view was 290 × 340 μm, same as the mouse kidney image shown in section 3.3. Non-uniform excitation over the image is corrected by normalizing the acquired images with the rhodamine solution image at each channel as described in the mouse kidney image. The signal contribution of the three fluorescent sources (DAPI, Alexa Fluor 488, TRITC) were estimated based on the estimated emission spectra over the eight channels as described in section 3.3. Fig 5.6 shows the nerve sample image. Each color is analogous to the fluorescent emission of one fluorescent source (red: TRITC, green: Alexa488, blue: DAPI). The instrument can successfully distinguish the spatial distribution of the fluorophores in the nerve sample in agreement with the published morphology of injured nerve samples [30]. The image consists of three parts: the nerve tissue (left), the inner lumen of the scaffold (right) and a cell-rich "capsule" that forms between the nerve and the scaffold (center). Phalloidin stains dimly sheath-like actin structures around the Schwann cells that surround axons, and tiny blood vessels in the nerve fascicle. A continuous line that stains strongly for phalloidin highlights the nerve perineurium, a thin layer of contractile cells around the fascicle. The perineurium is surrounded by epineurium, a collagenous connective tissue that stains dimly for DAPI (corresponds to the weak collagen autofluorescence) and αSMA (non-specific antibody binding). The bright circular blue feature at the center of the capsule is the autofluorescence emission of the stitch added by the surgeon to keep the nerve and the scaffold together. The stitch is surrounded by contractile cells that stain for phalloidin. In the capsule there are also several large blood vessels that stain brightly for both actin and αSMA. The scaffold stains dimly for collagen (dim DAPI signal) and also contains some weak αSMA signal (non-specific antibody binding). A number of contractile cells are bound on the scaffold. These contractile cells stain always strongly for actin and sometime for αSMA.

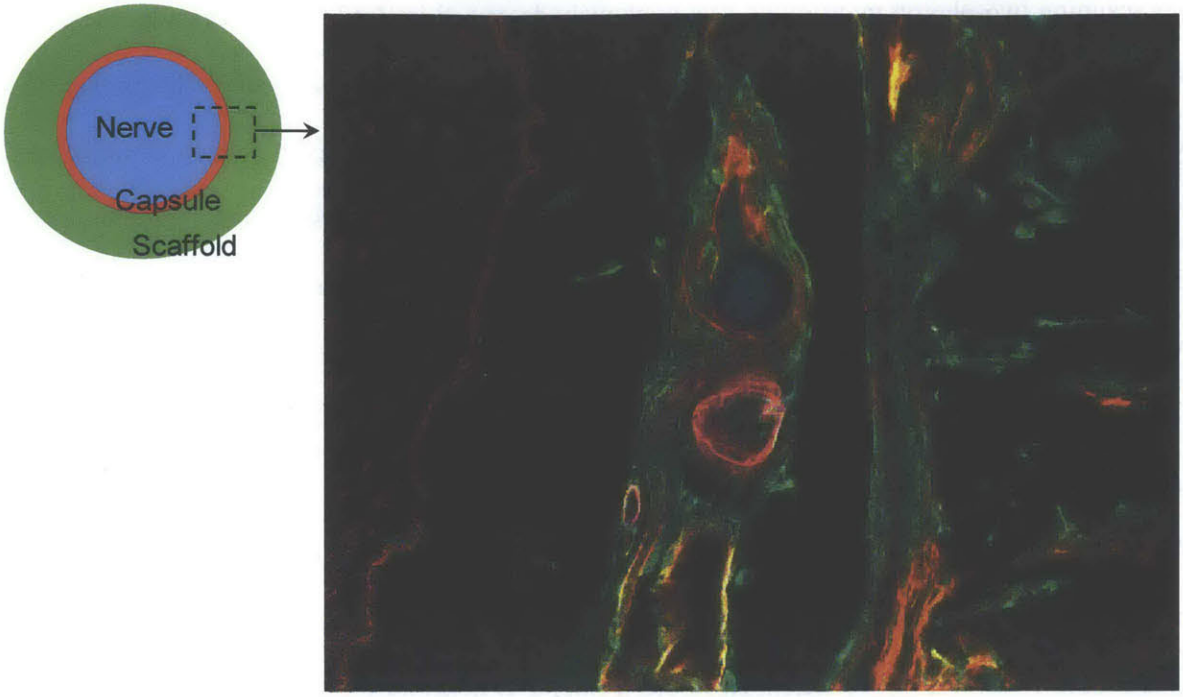

Fig 5.6. A nerve image surrounded by a scaffold labeled with three colors.

5.3.5. Mouse brain image

Lastly, we have performed in vivo imaging of neuron dendrite morphology and inhibitory synapse distribution in a rodent brain with the spectral-resolved MMM. To obtain mice that express fluorescent labels in a sparse subset of layer II/III pyramidal neurons in visual cortex, we *in utero* electroporated cre recombinase dependent expression plasmids for eYFP (for neuronal morphology) and Teal-Gephyrin (for inhibitory synapses) in timed pregnant C57BL6 mice as previously described in the reference [17]. Between 6-8 weeks of age, mice were anesthetized with isoflurane (3% for induction and 2% during surgery) and a 5mm glass coverslip was placed following craniotomy over the visual cortex. Imaging was performed on adult mice (>3months) anesthetized with isoflurane (3% for induction, 1-2% for imaging). The head was positioned in a custom made stereotaxic restraint affixed to a stage. Individual eYFP labeled dendrites and Teal-Gephyrin labeled synapses in layers 2/3 of visual cortex of an anesthetized adult mouse were imaged in the spectral-resolved MMM. As a comparison, the same animal was imaged using a single focus scanning two-photon microscope with two spectral channels. The single

focus scanning two-photon microscope was previously described in Ref [17]. Specifically, the excitation light path is practically identical to the spectral-resolved MMM except only a single focus is generated. The major difference of the single focus system is that the spectral-resolved detection is performed in a non-descanned configuration. The emission photons are collected by the same objective lens (W Plan-Apochromat, 20 ×, 1.0 NA, Zeiss, Thornwood, NY), and separated from the excitation beam path by a short-pass dichroic mirror (750dcspxr, Chroma Technology, Bellows Falls, VT). The emission photons are separated again by another dichroic mirror (520dcxr, Chroma Technology, Bellows Falls, VT) at 520 nm, which is the middle of the eYFP and Teal-Gephyrin emission peaks, and mapped onto two PMTs (R7400U-01 and R7400U-20, Hamamatsu, Bridgewater, NJ) locating at the conjugate plane of the back focal plane of the objective with the tube lens of the microscope (AXIOSKOP 2 FS, Zeiss, Thornwood, NY) and another lens (KPX079AR.14, Newport, Irvine, CA) in 4-f location. There are a BG39 (Newport, Irvine, CA) and a bandpass filter (hq485/70m-2p for Teal-Gephyrin and et560/80m-2p for eYFP, Chroma Technology, Bellows Falls, VT) in front of the two PMTs to block the excitation IR and get the photons in the designed spectral range. For these in vivo experiments, the excitation wavelength was 910 nm, the laser power was about 50 mW per focus, the dwell time was 40 μs with 0.5 μm pixel resolution, and the image size was 340 μm × 340 μm for both the spectral-resolved MMM and the single focus scanning microscope. For flat field correction, the acquired images were normalized with the rhodamine solution images acquired in each imaging system as described in section 3.3. For calibration measurements to obtain the true spectra for Teal and eYFP, HEK293 cells were singly transfected with plasmids pFueYFPW (for eYFP expression) or pFUTealW (for Teal expression) using calcium phosphate mediated gene transfer [32]. Transfected cells with each fluorescent labels were imaged in both systems. Imaging the cells labeled with the only single color provided the spectral distribution information of each label for the spectral decomposition. After the spectral unmixing the images were processed with background rejection and 2D B_3-Spline filter as a low pass filter as done in the previous publications [10, 17] since the dot-shape synapses are only about one micron size occupying 3×3 pixels and the maximum photon count

is only around 30, so the raw image is easily degraded by photon shot noise. While simple low pass filtering after unmixing provides fairly satisfactory results, more advanced unmixing algorithms including Poisson noise removal algorithm based on variance stabilization or maximum likelihood estimation may further improve our ability to identify small synapses [33-35].

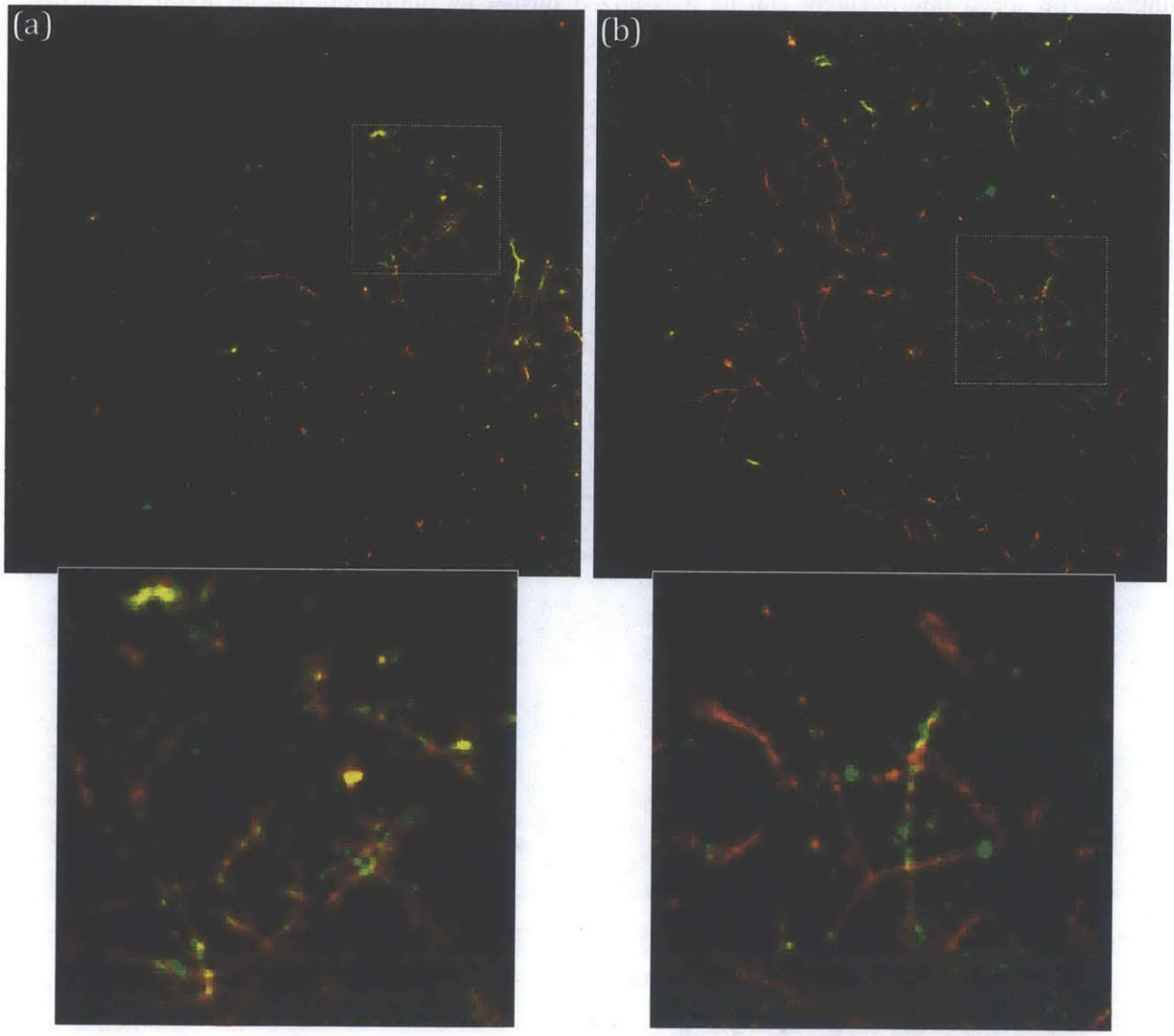

Fig 5.7. A mouse brain image labeled with two colors. (a) Spectral-resolved MMM image, (b) single focus scanning image and the enlarged images of the specified areas.

Fig 5.7 (a) shows the neuronal image taken by the spectral-resolved MMM and (b) is the image by the single focus scanning two-photon microscope at 60 μm depth. The bottom images are the enlarged images

of the specified area for details. The red line-shape structures are dendrites labeled with Teal-Gephyrin, and the green dots are synapses labeled with eYFP. The displayed red and green colors are pseudo-colors for better contrast. The spectral-resolved MMM acquired the image 4 times faster than the single focus scanning reducing the acquisition time of a general 1~2 hour brain imaging session [10, 17] to 15~30 minutes. The speed improvement can be maximized further by optimizing the DOE for more foci as described in the method section.

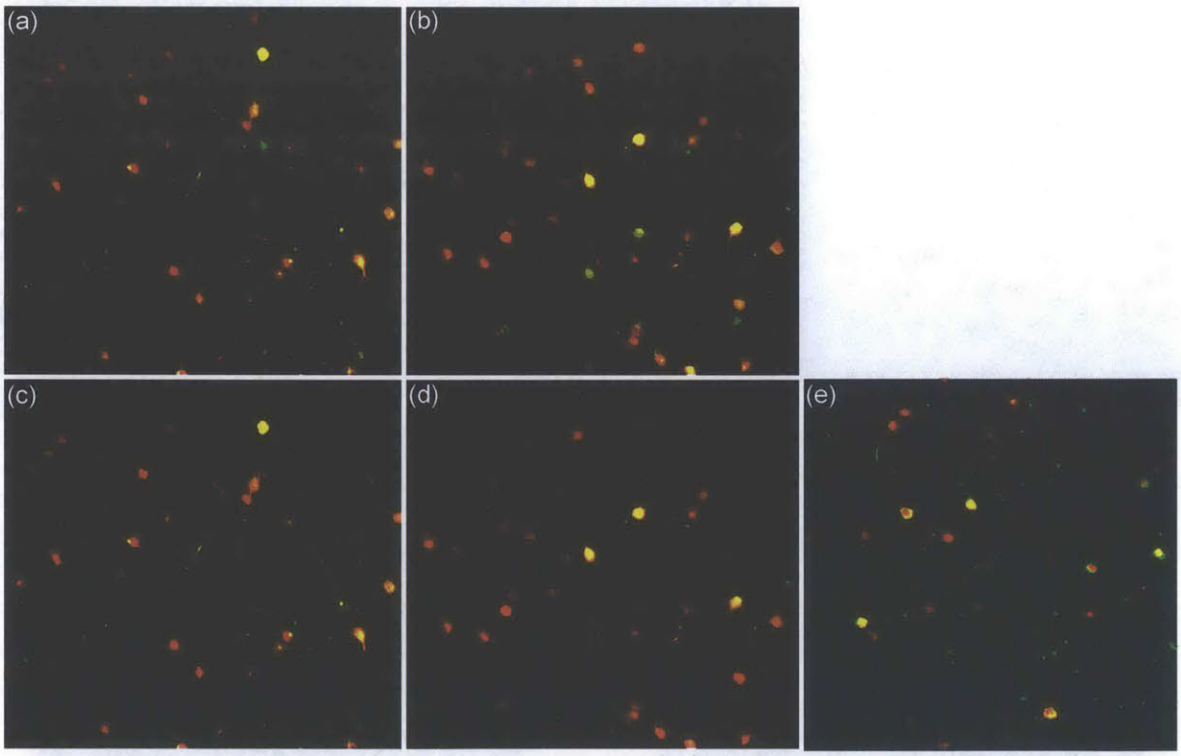

Fig 5.8. A mouse brain image labeled with two colors. (a) Spectral-resolved MMM image at 184 μm depth, and (b) at 156 μm depth. (c) The processed image of (a) with the ghost image removal algorithm, and (d) the processed image of (b). (c) Single focus scanning image at 156 μm depth.

It is known that the SNR of the MMM is lower than that of the single focus scanning two-photon microscope resulting in limited imaging depth [15], which is same for the spectral-resolved MMM. However, the typical imaging depth of 100-300 μm in the brain plasticity research can be achieved with MMM with MAPMT in the descanned configuration. Fig 5.8 shows the spectral-resolved MMM images

of the same animal used in Fig 5.7 at larger imaging depths. The raw images (Fig 5.8 (a) and (b)) showed image artifacts, appearing as ghost sub-images, due to scattering of the specimen from the large imaging depth, so they were processed with ghost image removal algorithm previously described in Ref [15]. The spectral-resolved MMM images at the larger imaging depths showed clear neuronal cell bodies and dendritic morphology (Fig 5.8 (c) and (d)) that is compared with single focus scanning system Fig 5.8 (e).

5.4. Discussion and Conclusion

MMM has successfully achieved the imaging speed improvement with the parallelized excitation. For applications that require spectral resolved imaging, we have developed a spectral-resolved MMM system that provide both high throughput and high content images. This spectral-resolved MMM is designed based on using one dimension of the MAPMT for resolving the signals from a multiple foci linear array while using the other dimension for resolving the spectral content of each foci. Within the available laser power the number of foci can be maximized resulting in maximum imaging speed improvement. This system has been demonstrated to successfully perform spectral resolved imaging deep in mouse brain in vivo with comparable SNR as single focus system but much higher speed.

This spectral-resolved MMM based on MAPMT is an interesting addition to other previous developed spectral-resolved MMMs. The use of the MAPMT with single-photon counting circuitry can achieve much higher frame rate compared with the system using imaging cameras [22], especially ones with long dead-time streak cameras [19-21]. However, streak camera has the advantage of providing lifetime-resolved imaging capability. In addition, multiple readouts (equal to the number of lines in an image) are required for these camera systems resulting in very undesirable accumulation of camera readout noise substantially degrading image SNR. Moreover, MMMs using cameras as detectors are vulnerable to scattering of emission photons in turbid specimens resulting in further degradation of SNR and limited imaging depth [15]. The pulse multiplexing MMMs have the advantage of mostly immune to emission photon scattering similar to single focus scanning systems [23, 24]. The pulse multiplexing system further

has the advantage that spectral detection can be readily accomplished with a grating spectrometer-camera system. A very promising system with two multiplexed beams has been demonstrated [25]. However, these pulse multiplexing MMMs require custom laser sources that is not broadly available. More importantly, the maximum number of time multiplexed beams generated by these laser sources are currently limited to less than ten resulting in slower imaging system compared with more conventional MMMs that can readily utilizes tens to hundreds of foci with a standard Ti-Sapphire oscillator.

One major disadvantage of MMM system based on MAPMT is the crosstalk between the foci resulting in image artifacts appearing as ghost images in the neighbor sub-images. Therefore, image post processing to unmix signals from the different foci may be required in highly turbid specimen or deep image [15]. More advanced cross talk removal algorithms based on a maximum likelihood approach is being developed [36].

The current eight channel detection allows us to image maximum eight different fluorophores, but practically to avoid severe spectral overlap, 3~4 color imaging would be a reasonable choice. To image more fluorophores at the same time, multiple MAPMTs or a SPAD array can be used. However, since different fluorophores have different excitation spectrum, simultaneous excitation with multiple excitation wavelengths may be required. Since DOE is wavelength dependent, the use of multiple excitation wavelengths can significantly complicate the design of this type of MMM systems.

One exciting future direction is the incorporation of simultaneous spectral and lifetime resolved imaging capability [19-21, 37]. For MMM systems based on MAPMT, high speed electronics for high speed fluorescence lifetime measurement can be readily implemented at the output anodes of 4x4 or 8x8 MAPMTs. A low cost, highly parallelized time-correlated single photon counting system based on high speed field programmable gate array electronics is under development.

For specimens with bright emission signals, spectral decomposition for fluorophores with sufficiently well separated spectra is often straight forward. However, for low level emission signals, the success of spectral decomposition is often limited by the inherent Poisson noise in the image data resulting in

significant uncertainty during spectral unmixing [38]. This error results in improper spectral decomposition and potential misinterpretation of the image data. Therefore, further spectral decomposition strategy such as image processing with the application of Poisson noise removal algorithms will be required [33-35].

References

1. Denk, W., J.H. Strickler, and W.W. Webb, *2-PHOTON LASER SCANNING FLUORESCENCE MICROSCOPY.* Science, 1990. **248**(4951): p. 73-76.
2. So, P.T.C., et al., *Two-photon excitation fluorescence microscopy.* Annual Review of Biomedical Engineering, 2000. **2**: p. 399-429.
3. Zipfel, W.R., R.M. Williams, and W.W. Webb, *Nonlinear magic: multiphoton microscopy in the biosciences.* Nature biotechnology, 2003. **21**(11): p. 1369-1377.
4. Helmchen, F. and W. Denk, *Deep tissue two-photon microscopy.* Nature methods, 2005. **2**(12): p. 932-940.
5. Denk, W., et al., *Anatomical and functional imaging of neurons using 2-photon laser scanning microscopy.* Journal of neuroscience methods, 1994. **54**(2): p. 151-162.
6. Yuste, R. and W. Denk, *Dendritic spines as basic functional units of neuronal integration.* Nature, 1995. **375**(6533): p. 682-684.
7. Svoboda, K., et al., *In vivo dendritic calcium dynamics in neocortical pyramidal neurons.* Nature, 1997. **385**(6612): p. 161-165.
8. Lee, W.C.A., et al., *Dynamic remodeling of dendritic arbors in GABAergic interneurons of adult visual cortex.* Plos Biology, 2006. **4**(2): p. 271-280.
9. Lee, W.C.A., et al., *A dynamic zone defines interneuron remodeling in the adult neocortex.* Proceedings of the National Academy of Sciences, 2008. **105**(50): p. 19968-19973.
10. Chen, J.L., et al., *Structural basis for the role of inhibition in facilitating adult brain plasticity.* Nature neuroscience, 2011. **14**(5): p. 587-594.
11. Bewersdorf, J., R. Pick, and S.W. Hell, *Multifocal multiphoton microscopy.* Optics Letters, 1998. **23**(9): p. 655-657.
12. Buist, A.H., et al., *Real time two-photon absorption microscopy using multi point excitation.* Journal of Microscopy-Oxford, 1998. **192**: p. 217-226.
13. Sacconi, L., et al., *Multiphoton multifocal microscopy exploiting a diffractive optical element.* Optics Letters, 2003. **28**(20): p. 1918-1920.
14. Watson, B.O., V. Nikolenko, and R. Yuste, *Two-photon imaging with diffractive optical elements.* Frontiers in neural circuits, 2009. **3**.
15. Kim, K.H., et al., *Multifocal multiphoton microscopy based on multianode photomultiplier tubes.* Optics Express, 2007. **15**(18): p. 11658-11678.
16. Gray, N.W., et al., *Rapid redistribution of synaptic PSD-95 in the neocortex in vivo.* PLoS biology, 2006. **4**(11): p. e370.
17. Chen, J.L., et al., *Clustered dynamics of inhibitory synapses and dendritic spines in the adult neocortex.* Neuron, 2012. **74**(2): p. 361-373.
18. van Versendaal, D., et al., *Elimination of inhibitory synapses is a major component of adult ocular dominance plasticity.* Neuron, 2012. **74**(2): p. 374-383.
19. Qu, J., et al., *Temporally and spectrally resolved sampling imaging with a specially designed streak camera.* Optics letters, 2006. **31**(3): p. 368-370.
20. Liu, L., et al., *Simultaneous time-and spectrum-resolved multifocal multiphoton microscopy.* Applied Physics B, 2006. **84**(3): p. 379-383.
21. Liu, L., et al. *Development of a Simultaneously Time-and Spectrum-Resolved Multifocal Multiphoton Microscopy System Using a Streak Camera.* in *Biophotonics, Nanophotonics and Metamaterials, 2006. Metamaterials 2006. International Symposium on.* 2006: IEEE.

22. Shao, Y., et al., *High-speed spectrally resolved multifocal multiphoton microscopy.* Applied Physics B, 2010. **99**(4): p. 633-637.
23. Amir, W., et al., *Simultaneous imaging of multiple focal planes using a two-photon scanning microscope.* Optics Letters, 2007. **32**(12): p. 1731-1733.
24. Chandler, E., et al., *High-resolution mosaic imaging with multifocal, multiphoton photon-counting microscopy.* Applied optics, 2009. **48**(11): p. 2067-2077.
25. Chandler, E.V., C.G. Durfee, and J.A. Squier, *Integrated spectrometer design with application to multiphoton microscopy.* Optics Express, 2011. **19**(1): p. 118-127.
26. Cova, S., et al., *20-ps timing resolution with single-photon avalanche diodes.* Review of scientific instruments, 1989. **60**(6): p. 1104-1110.
27. Dautet, H., et al., *Photon counting techniques with silicon avalanche photodiodes.* Applied optics, 1993. **32**(21): p. 3894-3900.
28. Cova, S., et al., *Avalanche photodiodes and quenching circuits for single-photon detection.* Applied optics, 1996. **35**(12): p. 1956-1976.
29. Molecular_Probes. *FluoCells® Prepared Slide #3 (Mouse Kidney Section with Alexa Fluor® 488 WGA, Alexa Fluor® 568 Phalloidin, DAPI)* Available from: http://www.lifetechnologies.com/order/catalog/product/F24630?ICID=search-f24630.
30. Soller, E.C., et al., *Common features of optimal collagen scaffolds that disrupt wound contraction and enhance regeneration both in peripheral nerves and in skin.* Biomaterials, 2012. **33**(19): p. 4783-4791.
31. Buydash, M., *Mechanical Modeling of Tissue Response During Early Stage Entubulated Peripheral Nerve Regeneration*, in *Department of Mechanical Engineering*. 2013, Massachusetts Institute of Technology.
32. Graham, F. and A. Van der Eb, *A new technique for the assay of infectivity of human adenovirus 5 DNA.* Virology, 1973. **52**(2): p. 456-467.
33. Nowak, R.D. and E.D. Kolaczyk, *A statistical multiscale framework for Poisson inverse problems.* Information Theory, IEEE Transactions on, 2000. **46**(5): p. 1811-1825.
34. Zhang, B., J.M. Fadili, and J.-L. Starck, *Wavelets, ridgelets, and curvelets for Poisson noise removal.* Image Processing, IEEE Transactions on, 2008. **17**(7): p. 1093-1108.
35. Spring, B. and R. Clegg, *Image analysis for denoising full-field frequency-domain fluorescence lifetime images.* Journal of microscopy, 2009. **235**(2): p. 221-237.
36. Cha, J.W., et al. *Spectral Decomposition of Multicolor Imaging in Multifocal Multiphoton Microscopy.* in *Biomedical Optics*. 2010: Optical Society of America.
37. Pelet, S., M.J. Previte, and P.T. So, *Comparing the quantification of Förster resonance energy transfer measurement accuracies based on intensity, spectral, and lifetime imaging.* Journal of biomedical optics, 2006. **11**(3): p. 034017-034017-11.
38. Pawley, J., *Handbook of biological confocal microscopy*. 2006: Springer.

Chapter 6

Conclusion and Outlook

This thesis has presented several significant improvements in multiphoton microscope design with a particular emphasis in improving the performance of multifocal multiphoton microscopes. First, adaptive optics (AO) compensation was introduced to improve signal-to-noise ratio (SNR) and resolution degraded due to the wavefront distortion by tissue specimens with inhomogeneous optical properties. The Shack-Hartmann wavefront sensor with a confocal depth selection mechanism could measure the wavefront distortion, and the deformable mirror could compensate the aberrations in the feedback loop. The AO compensation could achieve up to two fold signal improvement for peak intensities while suppressing the background signals improving image contrast. However, it has been also found that tissue scattering was the primary factor that limits the maximum imaging depth in tissue imaging by two-photon microscope. Given the limited imaging depth, the importance of AO compensation in many systems is relatively limited.

Secondly, a novel emission photon reassignment algorithm has been developed to overcome signal crosstalk between signals from different foci in MAPMT based MMMs. This photon reassignment algorithm is based on optical model based maximum likelihood optimization with minimal a prior measurements. This image post-processing method could significantly increase the SNR of the final processed image by reassigning the scattered photons to the original spatial locations and minimizing image artifacts.

Further, a new non-descanned MAPMT based MMM was developed to minimize the crosstalk between foci. This MMM could minimize crosstalk artifacts, appearing as ghost images, through maximizing foci separation by fully utilizing the large field-of-view (FOV), high numerical aperture (NA) objective lenses.

One complication in designing MMM systems with these large FOV objectives is that the edge and corner foci are susceptive to optical aberration if the intermediate optics of the microscope system is not optimized. However, the optimization of intermediate optics is found to be incompatible with the use of small, high speed galvanometric scanners and high NA objectives with large back aperture in the descanned configuration. Implementing MMM system with a novel non-descanned geometry could minimize the optical aberration of the edge and corner foci allowing full use of the large FOV objectives resulting in maximized foci separation. In addition, the non-descanned MMM further minimized the detection path length so that the signal collection efficiency could be improved up to four-fold. To detect the non-stationary emission signals and avoid the dead space of the MAPMT, a detection scheme that involves four times shifting of the image field was successfully demonstrated.

Finally, a spectral resolved MMM based on MAPMT was introduced to simultaneously improve imaging speed and enable spectral resolved detection. This system is configured by using one dimension of the MAPMT to detect signal from a linear array of excitation foci while using the other dimension for the spectral-resolved detection. We have demonstrated a system that generates four excitation foci along a line providing four time speed improvement. The signals from the four foci were distributed into eight spectral channels allowing simultaneous 3-4 color imaging in practice. In future implementation, clearly more foci can be generated with a different diffractive optical element (DOE) providing higher speed. In addition, imaging faster with more foci and/or imaging with high spectral resolution can be readily accomplished by implementing multiple MAPMTs together or by using single-photon avalanche diode (SPAD) array with more pixel elements. Simple spectral unmixing algorithm is used in this work but more advanced algorithm incorporating ideas such as Poisson noise removal algorithm is under development that promises to allow unmixing of images with more overlapped spectra or images with very low SNR.

In any case, it is true that the standard single focus scanning two-photon microscope will often have better SNR than MMM systems. It is also true that single focus scanning two-photon microscope will often have

better imaging depth than MMM systems. However, we have shown that MMM systems offer significant improvement in imaging speed that single focus system cannot rival (roughly equal to the number of foci generated) with only a minimal loss in SNR. Clearly, all imaging methodologies have their strengths and weakness. The appropriate imaging method should be selected to target a particular biomedical application. For example, there are many applications where the specimens contain sufficient fluorophores to provide sufficient SNR, and the use of MMM can greatly reduce image acquisition time and provide the opportunity to study system dynamics on the millisecond to second time scale. As another example, if imaging with both high speed and high spectral resolution is required, spectral-resolved MMM may be an excellent system for this type of tissue imaging applications.